Doctoral Dissertation
博士論文

Exploring the Frontiers of Low-Mass Galaxy Formation over the Cosmic History Using Large Observational Data

(大規模観測データで探る宇宙史を通した低質量銀河の形成)

A Dissertation Submitted for the Degree of Doctor of Philosophy
December 2021
令和3年12月博士 (理学) 申請

Department of Astronomy, Graduate School of Science,
The University of Tokyo
東京大学理学系研究科天文学専攻

Shotaro Kikuchihara
菊地原 正太郎

Ph.D. Thesis Committee:

- Dr. Kotaro Kohno[1,2] (Chair)
- Dr. Mamoru Doi[1,2,4]
- Dr. John D. Silverman[1,4]
- Dr. Masayuki Umemura[5]
- Dr. Hidenobu Yajima[5]

Thesis Adviser:

- Dr. Masami Ouchi[4,6,7]

[1] Department of Astronomy, Graduate School of Science, The University of Tokyo
[2] Research Center for the Early Universe, Graduate School of Science, The University of Tokyo
[3] Institute of Astronomy, Graduate School of Science, The University of Tokyo
[4] Kavli Institute for the Physics and Mathematics of the Universe, The University of Tokyo
[5] Center for Computational Sciences, University of Tsukuba
[6] Institute for Cosmic Ray Research, The University of Tokyo
[7] National Astronomical Observatory of Japan; Graduate University for Advanced Studies (SOKENDAI)

This thesis is based on the following papers:

Paper I.
S. Kikuchihara, M. Ouchi, Y. Ono, K. Mawatari J. Chevallard, Y. Harikane, T. Kojima, M. Oguri, G. Bruzual, and S. Charlot, “Early Low-mass Galaxies and Star-cluster Candidates at $z \sim 6-9$ Identified by the Gravitational-lensing Technique and Deep Optical/Near-infrared Imaging”, The Astrophysical Journal, Volume 893, pp.60-71, 2020

Paper II. S. Kikuchihara, Y. Harikane, M. Ouchi, Y. Ono, T. Shibuya, R. Itoh, R. Kakuma, A. K. Inoue, H. Kusakabe, K. Shimasaku, R. Momose, Y. Sugahara, S. Kikuta, S. Saito, N. Kashikawa, H. Zhang, and C.-H. Lee, “SILVERRUSH. XII. Intensity Mapping for Lyα Emission Extending over $100-1000$ comoving kpc around $z \sim 2-7$ LAEs with Subaru HSC-SSP and CHORUS Data”, arXiv:2108.09288, submitted to the Astrophysical Journal

ACKNOWLEDGEMENTS

I would like to express my deepest gratitude to my thesis supervisor, Masami Ouchi, for supporting and encouraging me throughout these five years. I also show my gratitude to the thesis committee members, Kotaro Kohno, Mamoru Doi, John D. Silverman, Masayuki Umemura, and Hidenobu Yajima for very useful discussion. I really thank the laboratory staff, Yoshiaki Ono, Takatoshi Shibuya, Kimihiko Nakajima, Shohei Aoyama, Ken Mawatari, Jun Toshikawa, Hideki Umehata, and Yuichi Harikane for kindly helping and teaching me. I thank my colleagues, Akira Konno, Seiji Fujimoto, Haibin Zhang, Takashi Kojima, Shiro Mukae, Yuma Sugahara, Ryo Higuchi, Hilmi Miftaful, Yechi Zhang, Shenli Tang, Ryota Kakuma, Karin Shimodate, Yuki Isobe, Nao Sakai, Dongsheng Sun, Yi Xu, Akinori Matsumoto, Moka Nishigaki, and Hiroya Umeda. I deeply thank Takako Idomura for helping me a lot with administrative procedures. I especially thank Ryohei Itoh for enjoying astronomy together.

I deeply thank Masamune Oguri, Masafumi Ishigaki, and Ryota Kawamata for teaching me a lot about lensing. I thank Dan Coe for letting me join the RELICS project. I thank Michiko Fujii, Takanobu Kirihara, and Daisuke Taniguchi for helping me in discussions about the Milky Way. I thank Rieko Momose, Haruka Kusakabe, Satoshi Kikuta, and Chris Byrohl for sharing discussion about extended Lyα emission. I thank the coauthors, Jacopo Chevallard, Gustavo Bruzual, Stéphane Charlot, Nobunari Kashikawa, Kazuhiro Shimasaku, Akio K. Inoue, Shun Saito, and Chien-Hsiu Lee. I thank my old colleagues in Kohno-lab, including Yoichi Tamura, Bunyo Hatsukade, Takuma Izumi, and Tsuyoshi Ishida.

I thank my friends working together on galactic astronomy, Kazuharu Himoto, Kei Ito, Kianhong Lee, Kana Moriwaki, Shigeru V. Namiki, Takafumi Tsukui, Satoshi Yamada, and Yui Yamashita. I thank my friends in Astronomy Department, including Noriaki Arima, Kah Wuy Chin, Noriyoshi Ishizuka, Yuki Takei, and Masamichi Zaizen. I thank my friends in Physics Department, including Soichiro Hashiba, Shin Kobayashi, Hiromasa Nakatsuka, Kumon Taku, Daichi Tsuna, and Kohei Yamamoto.

Lastly, I really thank *all* the researchers and students, not raised above, whom I met in these 7.5 years, for which I have been working on astronomy.

This work is based on observations obtained with the NASA/ESA Hubble Space Telescope, retrieved from the Mikulski Archive for Space Telescopes (MAST) at the Space Telescope Science Institute (STScI). STScI is operated by the Association of Universities for Research in Astronomy, Inc. under NASA contract NAS 5-26555. This work utilizes gravitational lensing models produced by PIs Bradač, Natarajan & Kneib (CATS), Merten & Zitrin, Sharon, Williams, Keeton, Bernstein and Diego, and the GLAFIC group. This lens modeling was partially funded by the HST Frontier Fields program conducted by STScI. The lens models were obtained from the MAST. This work is based on data and catalog products from HFF-DeepSpace, funded by the National Science Foundation and STScI.

Funding for the SDSS-IV has been provided by the Alfred P. Sloan Foundation, the U.S. Department of Energy Office of Science, and the Participating Institutions. SDSS-IV acknowledges support and resources from the Center for High Performance Computing at the University of Utah. The SDSS website is www.sdss.org.

SDSS-IV is managed by the Astrophysical Research Consortium for the Participating Institutions of the SDSS Collaboration including the Brazilian Participation Group, the Carnegie Institution for Science, Carnegie Mellon University, Center for Astrophysics — Harvard & Smithsonian, the Chilean Participation Group, the French Participation Group, Instituto de Astrofísica de Canarias, The Johns Hopkins University, Kavli Institute for the Physics and Mathematics of the Universe (IPMU) / University of Tokyo, the Korean Participation Group, Lawrence Berkeley National Laboratory, Leibniz Institut für Astrophysik Potsdam (AIP), Max-Planck-Institut für Astronomie (MPIA Heidelberg), Max-Planck-Institut für Astrophysik (MPA Garching), Max-Planck-Institut für Extraterrestrische Physik (MPE), National Astronomical Observatories of China, New Mexico State University, New York University, University of Notre Dame, Observatário Nacional / MCTI, The Ohio State University, Pennsylvania State University, Shanghai Astronomical Observatory, United Kingdom Participation Group, Universidad Nacional Autónoma de México, University of Arizona, University of Colorado Boulder, University of Oxford, University of Portsmouth, University of Utah, University of Virginia, University of Washington, University of Wisconsin, Vanderbilt University, and Yale University.

The HSC collaboration includes the astronomical communities of Japan and Taiwan, and Princeton University. The HSC instrumentation and software were developed by the National Astronomical Observatory of Japan (NAOJ), the Kavli Institute for the Physics and Mathematics of the Universe (Kavli IPMU), the University of Tokyo, the High Energy Accelerator Research Organization (KEK), the Academia Sinica Institute for Astronomy and Astrophysics in Taiwan (ASIAA), and Princeton University. Funding was contributed by the FIRST program from the Japanese Cabinet Office, the Ministry of Education, Culture, Sports, Science and Technology (MEXT), the Japan Society for the Promotion of Science (JSPS), Japan Science and Technology Agency (JST), the Toray Science Foundation, NAOJ, Kavli IPMU, KEK, ASIAA, and Princeton University.

The Pan-STARRS1 Surveys (PS1) and the PS1 public science archive have been made possible through contributions by the Institute for Astronomy, the University of Hawaii, the Pan-STARRS Project Office, the Max Planck Society and its participating institutes, the Max Planck Institute for Astronomy, Heidelberg, and the Max Planck Institute for Extraterrestrial Physics, Garching, The Johns Hopkins University, Durham University, the University of Edinburgh, the Queen's University Belfast, the Harvard-Smithsonian Center for Astrophysics, the Las Cumbres Observatory Global Telescope Network Incorporated, the National Central University of Taiwan, the Space Telescope Science Institute, the National Aeronautics and Space Administration under grant No. NNX08AR22G issued through the Planetary Science Division of the NASA Science Mission Directorate, the National Science Foundation grant No. AST-1238877, the University of Maryland, Eotvos Lorand University (ELTE), the Los Alamos National Laboratory, and the Gordon and Betty Moore Foundation.

This paper makes use of software developed for the Large Synoptic Survey Telescope. We thank the LSST Project for making their code available as free software at `http://dm.lsst.org`.

This paper is based on data collected at the Subaru Telescope and retrieved from the HSC data archive system, which is operated by the Subaru Telescope and Astronomy Data Center (ADC) at National Astronomical Observatory of Japan. Data analysis was in part carried out with the cooperation of Center for Computational Astrophysics (CfCA), National Astronomical Observatory of Japan. The Subaru

Telescope is honored and grateful for the opportunity of observing the Universe from Maunakea, which has the cultural, historical and natural significance in Hawaii.

This work is supported by World Premier International Research Center Initiative (WPI Initiative), MEXT, Japan, and KAKENHI (Grant Numbers 15H02064, 15H05892, 17H01110, 17H01114, 18K03693, 19J01222, 20J11993, 20H00180, 21H04467, and 21K13953) through Japan Society for the Promotion of Science. The NB387, NB527, and NB921 filters were supported by KAKENHI (23244022, 24244018, and 23244025, respectively) Grant-in-Aid for Scientific Research (A) through the JSPS. The NB816 filter was supported by Ehime University.

This work is supported by the joint research program of the Institute for Cosmic Ray Research (ICRR), The University of Tokyo.

ABSTRACT

In hierarchical structure formation, low-mass galaxies play a key role as the building blocks of the galaxy assembly. It is therefore important to reveal the physical processes that regulate low-mass galaxy formation. To this end, we investigate stellar mass functions (SMFs), rest-frame far ultra-violet (UV) luminosity functions (LFs), and Lyman-α (Lyα) emission radial profiles and their redshift evolution at $z \sim 0-9$, exploiting large observational data sets over the UV to mid-infrared (MIR) wavelength range. Estimating these three quantities help to understand the galaxy formation processes in a comprehensive way, because the stellar mass $M_{\star}$, UV magnitude $M_{\rm UV}$, and Lyα emission reflect the completed, ongoing, and future star formation activities, respectively.

First, we estimate SMFs at $z \sim 6-9$ and $z \sim 0$ using optical to MIR data of the *Hubble*+*Spitzer* Space Telescopes and the Sloan Digital Sky Survey (SDSS), respectively. To derive SMFs at $z \sim 6-9$, we use the very deep optical to MIR images of the *Hubble* Frontier Fields (HFF; $\sim 28-29$ and $\sim 25-26$ mag at 5σ in the optical and MIR bands, respectively) and 453 dropout galaxies that are strongly magnified by the foreground galaxy clusters. We investigate the stellar populations of the dropouts to estimate their $M_{\star}$ by fitting a stellar population synthesis and photoionization model to the observed photometries. For $z \sim 0$, we use the latest SDSS spectroscopic survey data over the very wide fields (~ 9400 deg^2). We apply the $1/V_{\rm max}$ method to 651202 galaxies at $z = 0.003-0.2$ to derive the SMF. We find that the SMFs reach down to $M_{\star} \sim 10^6 - 10^7\ M_{\odot}$ both at $z \sim 6-9$ and 0, with the flatter low-mass-end slopes $\alpha_{\star}$ toward low redshifts (from ~ -1.8 to -1.5). A turnover is identified in the very low-mass end of our $z \sim 0$ SMF ($M_{\star}^{\rm T} = 6.71^{+0.60}_{-0.42} \times 10^6\ M_{\odot}$), while no clear turnovers are found at $z \sim 6-9$.

Second, we discuss UV LFs at $z \sim 0-9$. We estimate a UV LF at $z \sim 0$ with the *Galaxy Evolution Explorer* (GALEX) survey data. We choose 67277 galaxies at $z = 0.003-0.2$ over the very large area of $> 10^4$ deg^2 from the latest GALEX catalog cross-matched with the SDSS spectroscopic catalog. We derive the UV LF down to $M_{\rm UV} \sim -10$ mag with the $1/V_{\rm max}$ method, finding that the faint-end slope is very flat ($\alpha_{\rm UV} = -1.30 \pm 0.01$). Comparing our UV LF with those at high redshifts taken from the literature, we identify an increasing trend of $\alpha_{\rm UV}$ toward low redshifts. We also find a tentative turnover at $M_{\rm UV}^{\rm T} \sim -11$ mag in our ~ 0 UV LF, while turnovers at

$z > 6$ are controversial due to the observational limits and lens model uncertainties.

Third, we probe extended diffuse Lyα emission around Lyα emitters (LAEs) at $z \sim 2-7$. We use the deep (~ 26 mag at 5σ) and large-area (~ 4.5 deg^2) data of the Subaru Telescope/Hyper Suprime-Cam (HSC) Strategic Program (SSP) and the Cosmic HydrOgen Reionization Unveiled with Subaru (CHORUS) project. We apply the intensity mapping technique to the narrow-band (NB) images and 1781 LAEs at $z = 2.2$, 3.3, 5.7, and 6.6, deriving the average Lyα surface brightness ($\mathrm{SB}_{\mathrm{Ly}\alpha}$) radial profiles around the LAEs. By carefully estimating systematics, we detect diffuse Lyα emission ($\sim 10^{-20}-10^{-19}$ erg s^{-1} cm^{-2} arcsec^{-2}) at $\sim 100-1000$ comoving kpc around $z = 3.3$ LAEs at the 4.1σ level and tentatively ($\sim 2\sigma$) at the other redshifts, beyond the virial radius R_{vir} of a dark-matter halo with a mass of 10^{11} $M_{\odot}$. We tentatively identify a decreasing trend $\mathrm{SB}_{\mathrm{Ly}\alpha}$ toward low redshifts when we correct $\mathrm{SB}_{\mathrm{Ly}\alpha}$ for the cosmological dimming effect. This result may be due to the decreasing cosmic hydrogen gas density according to the cosmic expansion. Comparisons with theoretical models suggest that extended Lyα emission outside R_{vir} is produced by Lyα photons that are resonantly scattered in the circum- and inter-galactic medium (CGM and IGM, respectively), and/or that are emitted from surrounding dwarf galaxies outside R_{vir}.

Based on these results, we discuss the galaxy formation processes. We find that both low-mass ends of the SMFs and faint ends of the UV LFs are steep at high redshifts, which implies that low-mass galaxies are abundant in the early universe. The low-mass- and faint-end slopes become flatter toward low redshifts as galaxies become massive through merging processes. At the lowest mass limits, star formation is strongly suppressed, which appears as turnovers in SMFs and UV LFs. We compare our estimation of $M_{\star}^{\mathrm{T}}$ and $M_{\mathrm{UV}}^{\mathrm{T}}$ with theoretical predictions, finding that the turnovers can be explained by the atomic gas cooling limit, supernova feedback, and/or photoionization due to the UV background (UVB) radiation. We also find that our $z \sim 0$ SMF is similar to that of the local satellite galaxies. This may suggest that the local satellite galaxies form in the physical process same as the central galaxies.

TABLE OF CONTENTS

CHAPTER 1
INTRODUCTION

1.1 Role of Low-Mass Galaxies in Galaxy Formation History

In the frame of the standard cold dark matter (CDM) model, primordial perturbation in the very universe grows large to create the density fluctuation through the gravitational instability (e.g., Mo et al. 2010; Loeb & Furlanetto 2013). Once the amplitude of the fluctuation exceeds a threshold, it collapses into a gravitationally bounded object, which is called a dark-matter halo (DMH). A DMH is filled with ionized hot gas just after the collapse. The gas releases its energy as radiation via the atomic and/or molecular gas cooling processes (e.g., Barkana & Loeb 2001; Nishi 2002). They fall into the central part of the DMH, subsequently forming a galaxy. In this picture, low-mass galaxies form first, and then merge to build massive ones (e.g., Press & Schechter 1974; Lacey & Cole 1993; Hopkins et al. 2008, see Figure 1.1). This formation scenario is called "hierarchical galaxy formation." Low-mass galaxies are important in studying galaxy formation processes, since they are the very "building blocks" in the hierarchical formation scenario.

Low-mass galaxies are important also in that they may be predecessors of present Milky Way-like galaxies. Galaxies with stellar masses ($M_\star$) of $\sim 10^6 - 10^7\ M_\odot$ at redshift $z \sim 6$ grow up to have $M_\star$ of $\sim 10^{10} - 10^{11}\ M_\odot$ at $z = 0$, according to the models of Behroozi et al. (2013) and Behroozi et al. (2019; in the case of a DMH mass M_h of $\sim 10^{12}\ M_\odot$; e.g., Sakamoto et al. 2003; Xue et al. 2008). That $M_\star$ value is similar to that of the Milky Way (e.g., Licquia & Newman 2015),

Low-mass galaxies are worth investigating also as sources of the cosmic reionization. Indeed, observational studies identified a large number of intrinsically faint galaxies in the reionization epoch with the intrinsic rest-frame ultra-violet (UV)[1] magnitudes M_UV of < -21 mag (detailed in Section 1.3.1). Because the escape fraction (f_esc) and production rate (ξ_ion) of ionizing photons are larger in fainter galaxies (e.g., Matthee et al. 2017; Nakajima et al. 2020), faint galaxies are likely to largely contribute to the reionization.

---

[1] Throughout the thesis, "UV" refers to far UV (~ 1500 Å), unless otherwise specified.

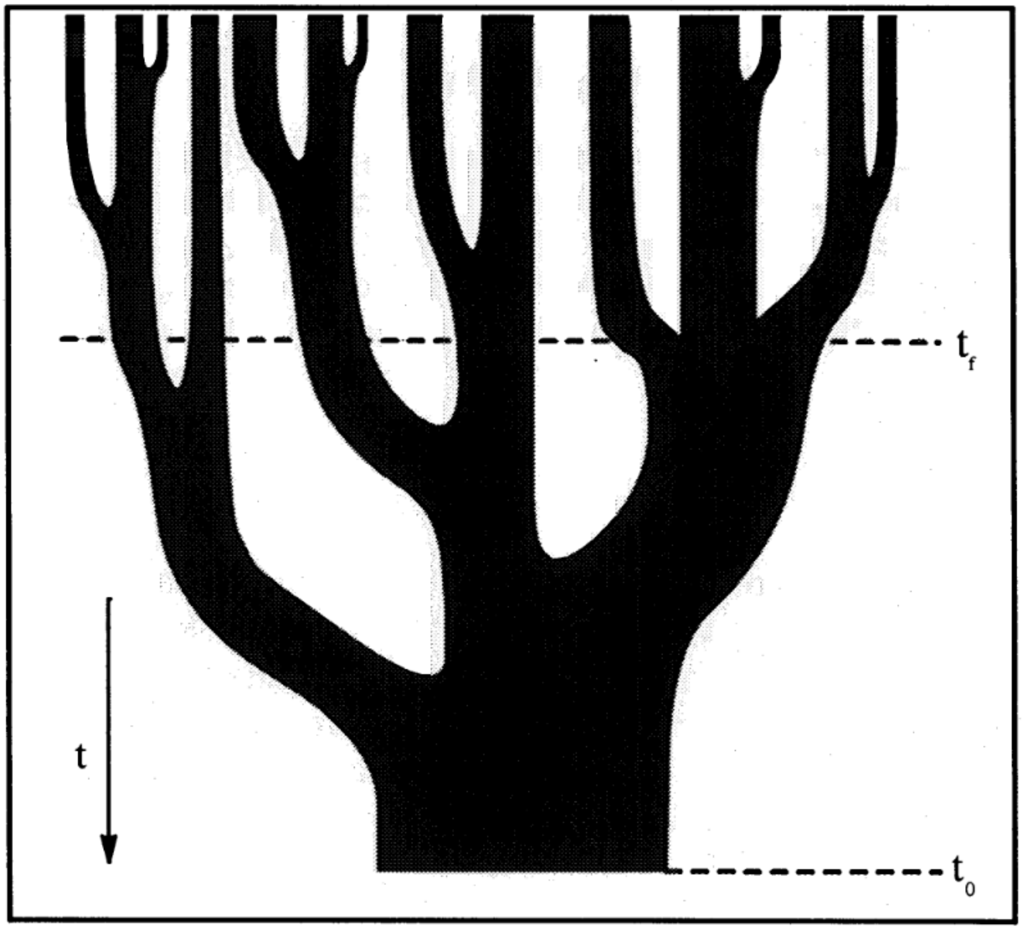

Figure 1.1 Schematic illustration of the hierarchical structure formation. Each branch represents a DMH, whose halo mass corresponds to the branch width. Time t goes from top to bottom, where $t_{\rm f}$ is the epoch when the halo mass exceeds half of the final halo mass, and t_0 is the present. Small halos (narrow branches) merge into larger ones as time passes. Adopted from Figure 6 of Lacey & Cole (1993).

1.2 Feedback Process Regulating Galaxy Formation

1.2.1 Theoretical Backgrounds

One of the fundamental physical quantities useful to understand galaxy formation is a number density distribution of the galaxies versus their masses, i.e., a mass function. Figure 1.2 compares a stellar mass function (SMF) and a DMH mass function (HMF) at $z \sim 6$. The black data points and solid line show the SMF and the best-fit Schechter (1976) function taken from the observational study of Song et al. (2016), while the gray line is the Sheth et al. (2001) HMF arbitrarily scaled to match the SMF at $M_\star \sim 10^{10}\ M_\odot$. As illustrated by the blue arrow, the SMF lies much below the HMF particularly in the low-mass regime, which indicates that the star formation activity is suppressed. Theoretical studies suggest that this is caused by stellar feedback, such as radiation from stars and supernovae (SNe; e.g., Dekel & Silk 1986; Read & Trentham 2005; McKee & Ostriker 2007; Somerville & Davé 2015; Naab & Ostriker 2017). The discrepancy between SMFs and HMFs is larger in the local universe than in the early universe. Indeed, the SMF and HMF at $z \sim 0$ roughly follow $\propto M_\star^{-0.5}$ (e.g., Baldry et al. 2012) and $\propto M_\star^{-1}$ (e.g., Sheth et al. 2001), respectively. In particular, the deficit of satellite galaxies around the Milky Way compared to the expectation by the CDM model is known as the "missing satellite problem" (e.g., Klypin et al. 1999; Moore et al. 1999; Tollerud et al. 2008; Tanaka et al. 2018, see also reviews by Bullock 2010; Kravtsov 2010). In summary, investigating the low-mass regimes of SMFs sheds light on the physical processes regulating star formation in low-mass galaxies.

Given that the star formation is strongly suppressed in low-mass galaxies, then a natural question that comes to our minds is about the *minimum* $M_\star$ value of galaxies. Indeed, theoretical studies predict that star formation almost completely halts below some critical $M_\star$, which is attributed to several physical mechanisms, such as the atomic gas cooling limit (e.g., Barkana & Loeb 2001; Jaacks et al. 2013), photoionization by the UV background (UVB) radiation (e.g., Efstathiou 1992; Quinn et al. 1996; Gnedin 2000; Kitayama et al. 2001; Susa & Umemura 2004; Okamoto et al. 2008; Finlator et al. 2012; Katz et al. 2020), and stellar feedback (e.g., Faucher-Giguère et al. 2011; Wyithe & Loeb 2013; Dayal et al. 2014; Yung et al. 2019b; Ocvirk et al. 2020; Qin et al. 2021).

- *Atomic gas cooling limit.* As touched above, baryons in a DMH start to collapse

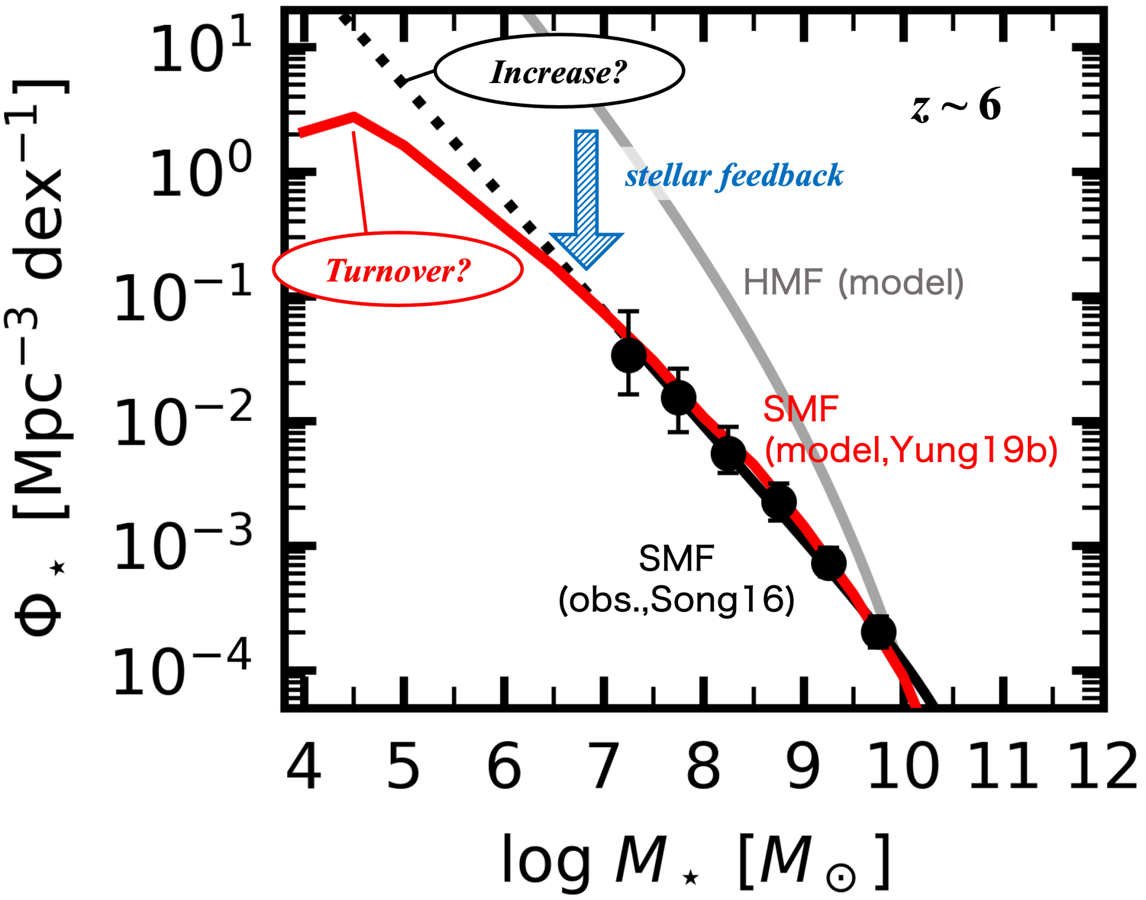

Figure 1.2 Mass functions at $z \sim 6$. The black circles are the observed SMF taken from Song et al. (2016), while the black solid and dotted lines represent the best-fit Schechter (1976) function and its extrapolation. The gray line represents the HMF of the Sheth et al. (2001) model arbitrarily scaled to match the SMF. The SMF falls below the HMF in the low-mass regime. The red solid lines show the model SMF of Yung et al. (2019b). Although the model predicts an inversion of the slope, i.e., a turnover, at $M_\star \sim 10^4 - 10^5\ M_\odot$, the insufficient survey depths have prevented its observational identification. The HMF is drawn with the `Colossus` toolkit (Diemer 2018).

when the gravity exceeds the internal pressure of the baryons. Star formation takes place when the baryons lose their energy via cooling. Cooling via hydrogen and helium atoms is effective at the virial temperature T_{vir} of $> 10^4$ K, which corresponds to M_{h} of $\sim 10^9\ M_\odot$ (Barkana & Loeb 2001). Below this threshold, cooling becomes insufficient, which prevents star formation.

- *Photoionization by the UVB*. When the UVB penetrates a DMH, it heats the baryons and prevents their accretion. This suppresses star formation in low-mass DMHs, say, of $M_{\mathrm{h}} < 10^{10}\ M_\odot$ (Okamoto et al. 2008). Massive DMHs can protect themselves against penetration of the UVB by the self-shielding effect (e.g., Susa & Umemura 2004), enabling star formation to take place.
- *Stellar feedback*. Strong stellar feedback can suppress star formation completely by expelling the baryons via outflows. The cosmological hydrodynamical (HD) simulation of Faucher-Giguère et al. (2011) predicts that the gas accretion rate is strongly suppressed due to outflows at $M_{\mathrm{h}} < 10^{11}\ M_\odot$.

The halting of star formation in low-mass galaxies should appear as a rapid drop of an SMF at its extremely low-mass end, which we hereafter refer to as a "turnover." For example, the semi-analytic model of Yung et al. (2019b) predicts turnovers in SMFs at $M_\star \sim 10^4 - 10^5\ M_\odot$, taking into account the cooling limit, photoionization, and stellar winds (the red line in Figure 1.2). Observing the lowest stellar-mass limit of an SMF is thus crucial to identify a turnover, and consequently to investigate the physical process regulating the formation of the *minimum-mass* galaxies. Given the strength of the effects above are expected to change along the cosmic time, due to, for example, the change in the intensity of the UVB and the depth of the potential wall of a halo, it is worth investigating turnovers both in the early and local universe, to understand the redshift evolution.

1.2.2 Previous Observations

Contrary to theoretical predictions, observational studies have failed to identify turnovers so far. At $z > 4$, observed near- to mid-infrared (NIR to MIR) photometric data help to estimate $M_\star$ via the amplitude of the 4000 Å/Balmer break. For example, Song et al. (2016) used $\sim$ 4500 galaxies over the wide fields of the Cosmic Assembly Near-infrared Deep Extragalactic Legacy Survey (CANDELS; Grogin et al. 2011; Koekemoer et al. 2011) and the Great Observatories Origins Deep Survey (GOODS; Giavalisco et al. 2004) to derive SMFs at $z \sim 4-8$. Although they found that the SMFs continue monotonically increasing down to $M_\star \sim 10^7\ M_\odot$, no feature of the turnover was identified.

At $z < 0.3$, Panter et al. (2004), Baldry et al. (2008), and Rodríguez-Puebla et al. (2020) used the optical spectroscopic data over the extremely wide fields of the Sloan Digital Survey (SDSS; e.g., Eisenstein et al. 2011; Blanton et al. 2017) to derive SMFs. They found that the SMFs are very flat at the low-mass ends (roughly $\propto M_\star^{-0.5}$). Similar results were obtained also in the Galaxy And Mass Assembly (GAMA) survey (e.g., Baldry et al. 2012; Wright et al. 2017). However, no turnovers have been identified down to $M_\star \sim 10^7\ M_\odot$ in any work.

In summary, the current observational limits ($M_\star \lesssim 10^7\ M_\odot$) are insufficient to identify turnovers both at high and low redshifts. Because the critical halo masses mentioned above ($M_\mathrm{h} \sim 10^9 - 10^{10}\ M_\odot$) correspond to $M_\star \sim 10^6 - 10^7\ M_\odot$ at $z \sim 0$ assuming the $M_\star$ to M_h ratios (SHMRs) of Behroozi et al. (2019), we need to advance the current observational limits down to much lower $M_\star$, say, of $\lesssim 10^7\ M_\odot$.

1.3 Observing Galaxy Formation from Multiple Aspects

The stellar mass of a galaxy is an indicator of the masses that are aggregated through the *completed* star formation. For a comprehensive understanding of galaxy formation, we also need to investigate young stars and gas, which are the proxies for *ongoing* and *future* star formation, respectively. We will inspect these factors by estimating rest-frame UV luminosity functions (LFs) and Lyman-α (Lyα) emission profiles, in addition to SMFs.

1.3.1 Ongoing Star Formation

A rest-frame UV LF is a number density distribution versus the rest-frame UV absolute magnitudes $M_{\rm UV}$ of the galaxies. *Ongoing* star formation can be estimated with a UV LF, because the UV light is emitted mainly from young O- and B-type stars contained in galaxies.

At $z > 6$, deep optical and NIR data of the Advanced Camera for Surveys (ACS) and the Wide Field Camera 3 (WFC3)-IR, respectively, on board the *Hubble* Space Telescope (HST) enable us to identify Lyman break galaxies and to estimate their UV LFs. For example, Ishigaki et al. (2018) derived UV LFs at $z \sim 6-10$ using the data of the *Hubble* Frontier Fields (HFF; Coe et al. 2015; Lotz et al. 2017). HFF is one of the most intensive surveys of the HST Treasury Programs (the 5σ limiting magnitudes are ~ 29 mag), and focuses on the galaxy cluster fields causing the strong gravitational lensing effect. Because the strong lensing effect magnifies the galaxies behind the clusters, HFF is advantageous for identifying galaxies that are *intrinsically* faint but magnified *apparently* brighter than observational limits. Ishigaki et al. (2018) found that the $z \sim 6 - 10$ UV LFs monotonically increase down to $M_{\rm UV} \sim -14$ rapidly.

Local UV LFs have been obtained mainly with the extremely wide field survey with the *Galaxy Evolution Explorer* (GALEX; Martin et al. 2005; Morrissey et al. 2005, 2007). For example, Budavári et al. (2005) and Wyder et al. (2005) cross-matched the GALEX sources with the spectroscopic survey data of the SDSS and the Two-Degree Field Galaxy Redshift Survey (2dFGRS; Colless et al. 2001), respectively, obtaining UV LFs at $z < 0.2$ down to $M_{\rm UV} \sim -12$ mag. Arnouts et al. (2005) derived UV LFs down to $M_{\rm UV} \sim -18$ to -16 mag at $0.2 < z < 3.4$. Their UV LFs exhibit very flat faint-end slopes. More recent studies, such as Cucciati et al. (2012), Driver et al. (2012), and Moutard et al. (2020), observed similar trends of the $z \sim 0$ UV LFs in the faint ends, using ground-based survey data.

These efforts have revealed the redshift evolution of the faint ends of the UV LFs, which becomes flatter toward low redshifts. Meanwhile, identification of turnovers has been still controversial both at high and low redshifts. For example, although Ishigaki et al. (2018) and Bouwens et al. (2017b) confirmed no turnovers down to $M_{\rm UV} \sim -14$ mag under multiple lens models (see Table 2 and Figure 8 of Bouwens et al. 2017b, see also Yue et al. 2018), Atek et al. (2018) claimed a turnover at $M_{\rm UV} = -14.9$ mag. The discrepancies are mainly due to the insufficient sensitivities of the observations, and uncertain lensing models. Also at $z \sim 0$, no previous studies have succeeded in identifying turnovers. More effective constraints by observations are necessary to settle these problems.

1.3.2 Fuel for Future Star Formation

The gas surrounding a galaxy, called the circumgalactic medium (CGM), falls onto the galaxy and triggers *future* star formation activity (e.g., Tumlinson et al. 2017; Péroux & Howk 2020). The hydrogen gas inside the CGM can be traced by Lyα emission, which is observed as a Lyα halo (LAH).

Many studies have detected LAHs around nearby galaxies (e.g., Östlin et al. 2009; Hayes et al. 2013, 2014). At high redshifts, meanwhile, LAHs have been identified mainly around massive galaxies, such as Lyman break galaxies (e.g., Hayashino et al. 2004; Swinbank et al. 2007; Steidel et al. 2011) and quasars (e.g., Goto et al. 2009; Cantalupo et al. 2014; Martin et al. 2014; Borisova et al. 2016; Arrigoni Battaia et al. 2019; Kikuta et al. 2019; Zhang et al. 2020). However, it remains difficult to detect diffuse emission around less massive galaxies, such as Lyα emitters (LAEs), at high redshifts, due to their faintness and sensitivity limits.

To overcome this difficulty, Rauch et al. (2008), for example, performed a very deep (92 hr) long-slit observation with the ESO Very Large Telescope (VLT)/FOcal Reducer and low dispersion Spectrograph 2 (FORS2) that reached a 1σ surface brightness (SB) detection limit of 8×10^{-20} erg cm^{-2} s^{-1} arcsec^{-2}. They investigated 27 LAEs at $z = 2.67 - 3.75$, identifying Lyα emission extended over 26 physical kpc (pkpc) around one of their LAEs. Individual detection of many high-redshift LAHs has been enabled by the advent of the Multi-Unit Spectroscopic Explorer (MUSE) installed on the VLT (Bacon et al. 2010). Recently, Leclercq et al. (2017) identified individual LAHs around 145 LAEs at $z = 3 - 6$ in the Hubble Ultra Deep Field (HUDF) with the VLT/MUSE (see also Wisotzki et al. 2016). Their data reached a SB limit of $\lesssim 10^{-19}$ erg s^{-1} cm^{-2} arcsec^{-2} at radii of > 10 pkpc.

A stacking method has been widely used to obtain averaged radial profiles of Lyα emission with high signal-to-noise (S/N) ratios (e.g., Matsuda et al. 2012; Momose et al. 2014, 2016; Xue et al. 2017; Wisotzki et al. 2018; Wu et al. 2020). For example, Momose et al. (2014) stacked Subaru Telescope/Suprime-Cam (SC) narrow-band (NB) images around > 100 LAEs at $z = 2.2 - 6.6$, obtaining Lyα radial profiles up to

~ 50 pkpc scales. Matsuda et al. (2012) and Momose et al. (2016) investigated the LAH size dependence on LAE properties, such as Lyα luminosity, UV magnitude, and overdensity, at $z = 3.1$ and 2.2, respectively. For example, Matsuda et al. (2012) suggested that the Lyα radial profiles become flatter as the surface number density of the LAEs increase.

Despite these efforts, it is still not clear whether Lyα emission continues to even larger scales, i.e., outside the virial radius ($R_{\rm vir}$) of DMHs.

This question is motivated by the recent identification of Lyα emission over $\sim$ 1 physical Mpc (pMp) scales tracing the filamentary structure of the cosmic web (Umehata et al. 2019; Bacon et al. 2021). Because they target Lyα emission in overdense regions at $z \sim 3-4$, we still need to investigate whether even field LAEs harbor such extended Lyα emission. In addition, no previous studies have investigated such extended Lyα emission over a wide redshift range with a unified method, which motivates us to reveal the redshift evolution of the Lyα emission radial profiles.

Another open question is the physical origin of Lyα emission (see review by Ouchi et al. 2020 and Figure 15 of Momose et al. 2016). Theoretical studies have suggested several physical processes, which can be attributed mainly to 1) resonant scattering and 2) *in-situ* production.

- *Resonant scattering.* Lyα photons are produced in the interstellar medium (ISM) of a galaxy, and then resonantly scattered by neutral hydrogen gas while escaping the galaxy into the CGM and intergalactic medium (IGM; e.g., Laursen & Sommer-Larsen 2007; Laursen et al. 2011; Steidel et al. 2011; Zheng et al. 2011; Dijkstra & Kramer 2012; Jeeson-Daniel et al. 2012; Verhamme et al. 2012; Kakiichi & Dijkstra 2018; Smith et al. 2018, 2019; Garel et al. 2021).

- *In-situ production.* Lyα photons are produced not inside the galaxy, but in the CGM. This can be further classified into three processes: i) recombination, ii) collisional excitation, and iii) satellite galaxies. i) Recombination: ionizing radiation from the galaxy or extragalactic UVB photoionizes the hydrogen gas in the CGM, which in turn emits Lyα emission via recombination ("fluorescence"; e.g., Furlanetto et al. 2005; Cantalupo et al. 2005; Kollmeier et al. 2010; Lake et al. 2015; Mas-Ribas & Dijkstra 2016; Gallego et al. 2018; Mas-Ribas et al. 2017b). ii) Collisional excitation: hydrogen gas in the CGM is compressively

> heated by shocks and then emit Lyα photons by converting its gravitational energy into Lyα emission while accreting onto the galaxy ("gravitational cooling" or "cold stream"; e.g., Haiman et al. 2000; Fardal et al. 2001; Goerdt et al. 2010; Faucher-Giguère et al. 2010; Rosdahl & Blaizot 2012; Lake et al. 2015). iii) Satellite galaxies: Lyα emission is produced by star formation in unresolved dwarf galaxies ("satellite galaxies") surrounding the central galaxy (e.g., Mas-Ribas et al. 2017a,b).

Major mechanisms producing extended Lyα emission have been controversial. For example, Momose et al. (2016) suggest that the contributions of resonant scattering in the CGM and satellite galaxies cannot be ruled out, and Leclercq et al. (2017) admit the possibilities of all the processes above. Fluorescence is considered to play a major role in quasars (e.g., Kollmeier et al. 2010; Kikuta et al. 2019).

1.4 Goals of the Thesis

Our goal in this thesis is to comprehend the formation of low-mass galaxies from multiple aspects: stellar mass, UV light, and Lyα emission. We stress again that these three factors reflect completed, ongoing, and future star formation. We work on the SMFs, UV LFs, and Lyα emission profiles over a wide redshift range exploiting various observational data sets. Our strategies and the thesis constitution (Chapters 2 to 4) are detailed below, and schematically summarized in Figure 1.3. Discussions and a summary are given in Chapters 5 and 6, respectively.

1.4.1 SMFs

We study SMFs at $z \sim 0-9$ in Chapter 2. As touched in Section 1.2, the low-mass end of an SMF sheds light on physical processes regulating the formation of low-mass galaxies. Identifying a turnover is especially important to understand the complete suppression of star formation. Therefore, our aim is to observationally put constraints on the low-mass ends of SMFs, including turnovers, and to investigate their redshift evolution.

Again, a stellar mass of a galaxy can be estimated with its Balmer break. Because the break is observed in the infrared and optical wavelengths for galaxies at $z > 6$ and $z \sim 0$, respectively, we focus on SMFs at $z > 6$ and $z \sim 0$.

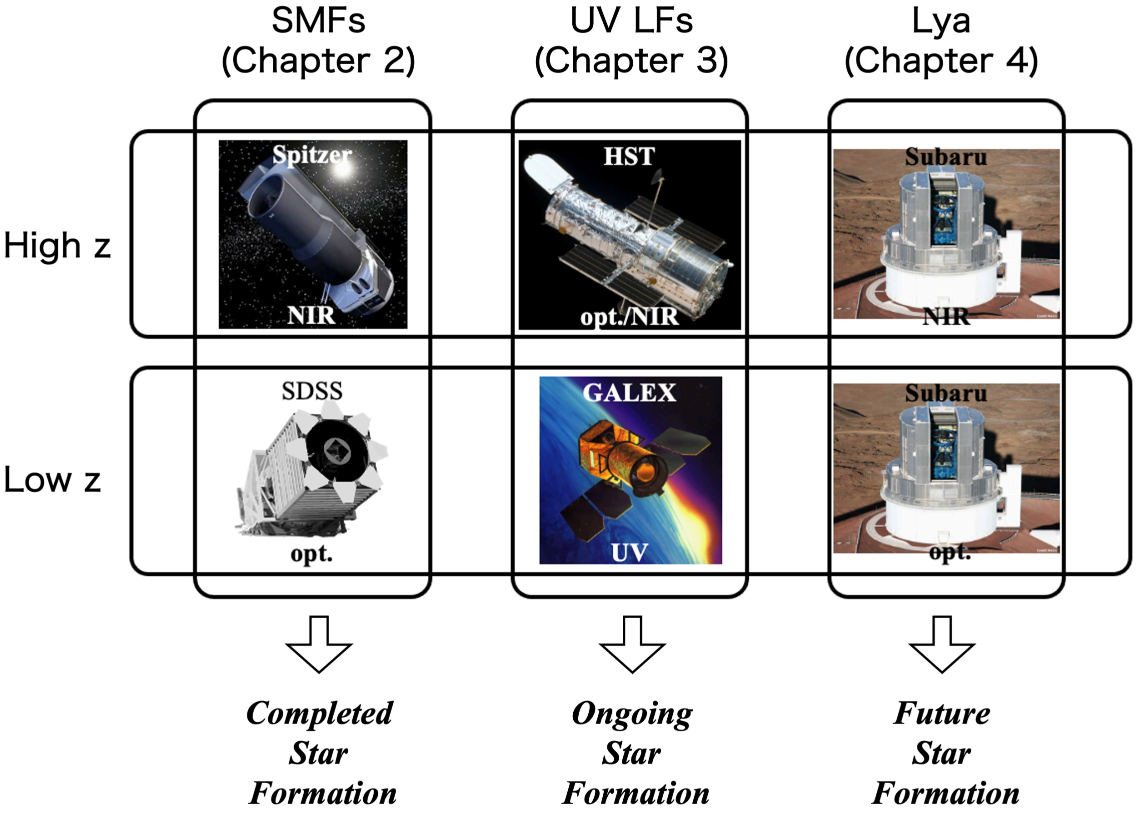

Figure 1.3 Overview of this thesis. We investigate SMFs, UV LFs, and Lyα emission at $z \sim 0-9$ mainly using the observational data with the telescopes shown in the grids. Illustrations/pictures: © NASA, SDSS, and NAOJ.

At $z > 6$, we utilize the data of HFF. HFF provides very deep optical/NIR and MIR data taken with the HST and the *Spitzer* Space Telescope, respectively, over six galaxy cluster fields and their parallel fields. We also utilize NIR observational data of the VLT and Keck Telescope. The lensing effect caused by the galaxy clusters helps to estimate $M_\star$ with high S/N ratios. Our study is the first to use the latest complete data sets of HFF to estimate SMFs, while previous studies were limited to part of the fields.

At $z \sim 0$, we exploit the spectroscopic survey data of SDSS that spans an extremely wide area of ~ 9400 deg^2. Owing to the extremely wide area, we anticipate a large number of galaxies, including intrinsically faint ones. In the local universe, wide-field surveys are more advantageous to identify intrinsically faint galaxies very close to observers, while deep pencil-beam surveys are suitable for searching high-redshift galaxies.

1.4.2 UV LFs

UV LFs at $z \sim 0 - 9$ are discussed in Chapter 3. We aim to study the faint ends of UV LFs, and subsequently to reveal galaxy formation by comparing the UV LFs with the SMFs.

At $z > 6$, again, rest-frame UV emission can be measured with the HST/ACS and WFC3-IR. Thus we take the latest results of the HFF from Ishigaki et al. (2018), since they have already reached the very faint ends ($M_{\rm UV} \sim -14$ mag).

At $z \sim 0$, we use the latest data release (GR6/7) of GALEX to derive a UV LF. We use the GALEX source catalog cross-matched with the SDSS spectroscopic catalog, which features an extremely wide area of 1.1×10^4 deg^2 (Bianchi & Shiao 2020). This area is much wider than those used in previous GALEX work (e.g., 43.9 and 56.7 deg^2 in Budavári et al. 2005 and Wyder et al. 2005, respectively).

1.4.3 Lyα Emission Profiles

We address the Lyα emission profiles at $z \sim 2 - 7$ in Chapter 4. Our aim is to reveal averaged profiles of very diffuse ($\lesssim 10^{-19}$ erg s^{-1} cm^{-2} arcsec^{-1}) Lyα emission out to large scales ($> R_{\rm vir}$), and to reveal the physical mechanism governing extended Lyα emission.

To this end, we utilize the intensity mapping technique (Kovetz et al. 2017 for a review; see also Carilli 2011; Gong et al. 2011; Silva et al. 2013; Pullen et al. 2014; Comaschi & Ferrara 2016a,b; Li et al. 2016; Fonseca et al. 2017), which is based on cross-correlation functions between objects and their emission or absorption spectra. This technique enables us to detect signals from targeted galaxies with a high S/N ratio by efficiently estimating and removing contaminating signals from foreground interlopers. For example, Croft et al. (2016, 2018) derived cross-correlation functions between the Lyα emission and quasar positions at $z = 2 - 3.5$ using the SDSS data, detecting positive signals up to a ~ 20 comoving Mpc (cMpc) radial scale.

More interestingly, Kakuma et al. (2021) tentatively identified very diffuse ($\sim 10^{-20}$ erg s^{-1} cm^{-2} arcsec^{-2}) Lyα emission extended around over the $R_{\rm vir}$ scales. They applied the intensity mapping technique to the NB816 and NB921 images of the Subaru/Hyper Suprime-Cam (HSC) Strategic Program (HSC-SSP; Aihara et al. 2019) and LAEs at $z = 5.7$ and 6.6. Their finding motivates us to investigate whether such extended structures exist even at lower redshifts. We can now access Lyα emission at $z < 4$ owing to the advent of the Cosmic HydrOgen Reionization Unveiled with Subaru (CHORUS; Inoue et al. 2020) project, whose NB387 and NB527 filters capture Lyα emission from galaxies at $z = 2.2$ and 3.3, respectively. In this thesis, we systematically investigate Lyα emission extended beyond $R_{\rm vir}$ around the LAEs at $z = 2.2 - 6.6$, by taking advantage of the intensity mapping technique and ultra-deep images of the HSC-SSP and CHORUS projects.

1.5 General Assumptions throughout the Thesis

Throughout the thesis, we adopt the concordance cosmology with $\Omega_{\rm m,0} = 0.7$, $\Omega_{\Lambda,0} = 0.3$, and $H_0 = 70$ km s^{-1} Mpc^{-1}. In this cosmology $1''$ corresponds to transverse sizes of (8.3, 7.5, 5.9, 5.4) pkpc and (26, 32, 39, 41) comoving kpc (ckpc) at $z = (2.2,\ 3.3,\ 5.7,\ 6.6)$.

Magnitudes are given in the AB system (Oke & Gunn 1983). The conversion between an apparent magnitude m and an absolute/intrinsic magnitude M for an object at redshift z is given as

$$m = M + 5\log[d_{\rm L}(z)/10\ {\rm pc}] + K(z) - 2.5\log[\mu(z)], \tag{1.1}$$

where $5\log[d_\mathrm{L}(z)/10\ \mathrm{pc}]$ and $d_\mathrm{L}(z)$ are the distance modulus and luminosity distance, respectively (Hogg 1999). The k-correction is termed as $K(z)$. We assume flat UV continua, i.e., $K(z) = -2.5\log(1+z)$. When the object is magnified, $-2.5\log[\mu(z)]$ is taken into account, where $\mu(z)$ is the best-fit magnification factor at the position of the object. An *absolute* magnitude refers to the magnitude of an object when it is observed from 10 pc away, while an *intrinsic* magnitude means the absolute magnitude that is corrected for the lensing effect. In short, an *intrinsic* magnitude is a *de-lensed absolute* magnitude.

We adopt the Chabrier (2003) initial mass function (IMF) in a mass range of $0.1 - 100\ M_\odot$ to estimate $M_\star$. All the $M_\star$ values taken from previous studies are converted to those estimated with the Chabrier (2003) IMF. For example, a $M_\star$ value estimated with the Salpeter (1955) IMF is divided by 1.64 to match to the Chabrier (2003) IMF.

CHAPTER 2
STELLAR MASS FUNCTIONS

In this Chapter, we investigate the SMFs of galaxies at $z \sim 6-9$ (Section 2.1) and $z \sim 0$ (Section 2.2) using the data mainly of HST+*Spitzer* and SDSS, respectively. The redshift evolution of the SMFs will be discussed in Section 2.3.

2.1 SMFs at $z > 6$

2.1.1 Data

HST Data and Samples

We make use of the image mosaics obtained in the HFF program, which targets six cluster fields—Abell 2744, MACS J0416.1−2403, MACS J0717.5+3745, MACS J1149.6+2223, Abell S1063, and Abell 370—and their accompanying six parallel fields. We hereafter denote them as A2744C/P, M0416C/P, M0717C/P, M1149C/P, A1063C/P, and A370C/P, respectively, where C/P indicates cluster/parallel field. All of the 12 fields were observed with the three bands of the ACS and four bands of the WFC3/IR; F435W (B_{435}), F606W (V_{606}), F814W (i_{814}), F105W (Y_{105}), F125W (J_{125}), F140W (JH_{140}), and F160W (H_{160}). The throughputs of these filters are shown in Figure 2.1. We utilize the drizzled and weight images that were produced by Shipley et al. (2018) in the manner summarized below. [1] First, the HFF v1.0 images were downloaded from the MAST archive. [2] The point-spread functions (PSFs) of these images were homogenized to those of the H_{160} images. The PSF full width at half maximum (FWHM) of the homogenized images is $\sim 0.''18$. Second, the bright cluster galaxies (bCGs) were modeled and subtracted from the images to avoid the diffuse intracluster light (ICL) in photometry of the background faint sources. The Galactic extinction was also corrected. All of the images have a pixel scale of $0.''06$.

We divide each image into 3×3 grid cells, and measure the limiting magnitude in each cell (~ 1 arcmin^2). This is because limiting magnitudes are not homogeneous due to the ICL (e.g., Montes & Trujillo 2014; Ishigaki et al. 2015; Kawamata et al.

---

[1] `http://cosmos.phy.tufts.edu/~danilo/HFF/Download.html`

[2] `http://www.stsci.edu/hst/campaigns/frontier-fields/`

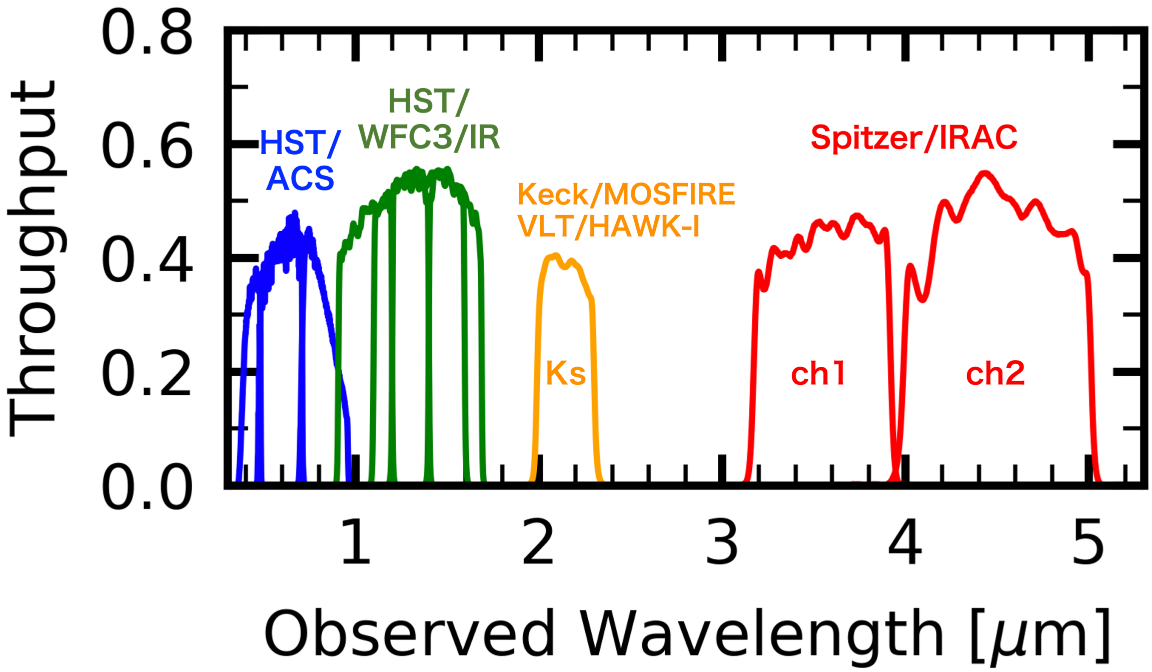

Figure 2.1 Filter throughputs in the B_{435}, V_{606}, and i_{814} bands (HST/ACS; blue), the Y_{105}, J_{125}, JH_{140}, and H_{160} bands (HST/WFC3/IR; green), the $K_{\rm s}$ band (Keck/MOSFIRE and VLT/HAWK-I; orange), and ch1 and ch2 (*Spitzer*/IRAC; red).

2016). The 5σ limiting magnitudes in the H_{160} band images are $\sim 28.4 - 29.2$ mag in a $0\farcs35$-diameter circular aperture.

We use the galaxy sample selected by Kawamata et al. (2018) and Ishigaki et al. (2018), which consists of 350, 64, and 39 dropout galaxies ("dropouts" or Lyman break galaxies, LBGs) at $z \sim 6 - 7$, 8, and 9, respectively, 453 in total. We estimate their photometries as follows. First, we measure the aperture magnitude $m_{\rm aper}$ with a diameter of $D_{\rm aper} \equiv 0\farcs35$ at the position of the dropouts, using the IRAF task `phot` (Tody 1986, 1993). Second, we apply an aperture correction. To evaluate the aperture correction term $c_{\rm aper}$, we create a median-stacked J_{125}-band image of the i-dropouts with PSF homogenization, and measure the aperture flux of the stacked dropout with changing the aperture diameter. Because ~ 95 % of the total flux is contained in a $1\farcs2$-diameter aperture, we take the magnitude within a $1\farcs2$-diameter aperture as the total magnitude $m_{\rm tot}$. The magnitude within a $0\farcs35$-diameter aperture is fainter than $m_{\rm tot}$ by 0.96 mag, so we define $c_{\rm aper} \equiv 0.96$ mag in the J_{125} band. Because the PSFs in the HST-band images are homogenized, we can apply the same aperture correction to all the bands. Finally, we estimate the total magnitude $m_{\rm tot}$ as $m_{\rm tot} = m_{\rm aper}(D_{\rm aper}) - c_{\rm aper}$.

We take J_{125}, JH_{140}, and H_{160} band magnitudes as the rest-frame UV apparent magnitudes $m_{\rm UV}$ of the dropouts at $z \sim 6-7$, 8, and 9, respectively. The mean values of relative errors of $m_{\rm UV}$ estimated by either two of Kawamata et al. (2018), Ishigaki et al. (2018), and this work are only ~ 1 %, implying a good consistency among the three measurements.

VLT and Keck Data

We use the $K_{\rm s}$ band ($\lambda = 2.2$ μm) images obtained by the K-band Imaging of the Frontier Fields (KIFF) program (Brammer et al. 2016). Ground-based observations in the $K_{\rm s}$ band help to narrow down the position of the Balmer break with *Spitzer* data. The deep images of the VLT/High Acuity Wide field K-band Imager (HAWK-I) are available in A2744, M0416, A1063, and A370. Additionally, M0717 and M1149 are observed with Keck-I/Multi-Object Spectrometer For Infra-Red Exploration (MOSFIRE). The HAWK-I and MOSFIRE images have the PSF FWHM of $\sim 0\farcs4 - 0\farcs5$. We utilize the drizzled and weight images of Shipley et al. (2018). The pixel scale of the images is $0\farcs06$, which is matched to that of the HST images. Photometry and limiting-magnitude measurements are conducted in the same manner as for the HST images, but with $D_{\rm aper} = 0\farcs6$. Brammer et al. (2016) report the values of $c_{\rm aper}$ in each HFF field. Because the mean value of $c_{\rm aper}$ weighted by the number of our dropouts in each field is 0.74, we define $c_{\rm aper} \equiv 0.74$ in the $K_{\rm s}$ band. The 5σ limiting magnitudes are $\sim 25.3 - 26.2$ mag in a $0\farcs6$-diameter circular aperture.

Spitzer Data

We utilize the drizzled and weight images of ch1 ($\lambda = 3.6\ \mu$m) and ch2 ($\lambda = 4.5\ \mu$m) of the Infrared Array Camera (IRAC). The images are reduced by Shipley et al. (2018), who combine the photometric data by 2016 December, subtract bCGs, and correct for the Galactic extinction. In both ch1 and ch2, the PSF FWHM is $\sim 1\farcs7 - 2\farcs0$, and pixel scales are $0\farcs3$. Photometry and limiting-magnitude measurements are conducted in the same manner as for the HST images, but with $(D_{\rm aper}, c_{\rm aper}) = (3\farcs0, 0.52)$ and $(3\farcs0, 0.55)$ for ch1 and ch2, respectively (Ono et al. 2010). The 5σ limiting magnitudes are $\sim 24.7 - 25.4$ mag in a $3\farcs0$-diameter circular aperture.

Lens Models

To estimate the intrinsic photometries of the dropouts, we adopt the best-fit magnification factors $\mu_{\rm best}$ from the `glafic` (Oguri 2010) parametric models derived by Kawamata et al. (2018, see also Kawamata et al. 2016). [3] Although the uncertainties of $\mu_{\rm best}$ are not considered to derive the $M_\star$-$m_{\rm UV}$ relations here (Section 2.1.2), the uncertainties propagate from the UV LFs of Ishigaki et al. (2018) to the SMFs.

We should also pay attention to the systematical discrepancy among lens models. Priewe et al. (2017) estimate the uncertainties of the eight mass models of M0416, using a fractional normalized median absolute deviation, which is defined as

$$\mathrm{fNMAD} \equiv 1.4826 \times \mathrm{median}|\mu_{\rm m}(\boldsymbol{\theta}) - \tilde{\mu}|/\tilde{\mu}. \tag{2.1}$$

Here $\mu_{\rm m}(\boldsymbol{\theta})$ is the magnification factor calculated with a given model m at a given position $\boldsymbol{\theta}$, and $\tilde{\mu}$ is the median of the magnification factors. They find that fNMAD $\sim$ 0.3 (0.7) at $\tilde{\mu} \sim 2$ (40) in M0416, which implies that magnification factors of different

---

[3] https://archive.stsci.edu/prepds/frontier/lensmodels/

models differ only by a factor of ~ 2 (Meneghetti et al. 2017, see also). Therefore, the model discrepancy is unlikely to affect our main results. Indeed, Ishigaki et al. (2018) confirm that their UV LFs are robust against the lens model discrepancy (see their Figure 7).

2.1.2 Methods

We find that the detection of the individual dropouts in the NIR to MIR bands is very ambiguous (the median S/N ratio in ch1 is ~ 1.1). This prevents us directly measuring $M_\star$ of the individual dropouts. To avoid this observational difficulty, we first stack the image in each band to improve the S/N ratios, and derive the averaged value of $M_\star$ for each $M_{\rm UV}$. Then we apply the $M_\star$-$M_{\rm UV}$ relations to UV LFs to derive the SMFs.

Stacking

First, we calculate the intrinsic magnitude $M_{\rm UV}$ of a dropout using Equation (1.1). We divide our dropouts into subsamples by the values of $M_{\rm UV}$ at $z \sim 6-7$, 8, and 9. A summary of the subsamples is shown in Table 2.1.

In each band, we cut out images centered at the positions of dropouts, and divide the pixel counts by the magnification factors of the dropouts. We then median-stack the images of the dropouts for each subsample with `iraf` task `imcombine`. We do not consider the stretching effect by lensing, because the apparent sizes of our dropouts are very small.

Because of the poor spatial resolution of the IRAC, our dropouts may be blended with other nearby sources. However, based on our visual check on the IRAC images of the dropouts, we find that 384 dropouts (~ 85 % out of the total sample) have no nearby bright sources within a $3''.0$-diameter aperture. Additionally, we adopt median stacking to suppress the effects of outliers. These facts imply that contamination does not significantly affect the resulting photometry of the stacked dropouts. Even when we use these 384 dropouts and perform stacking analysis and photometry, the SEDs do not change beyond the uncertainties. We thus use the full sample of 453 dropouts hereafter for statistical accuracy.

Figures 2.2 and 2.3 show the stacked images of the $z \sim 6-7$, 8, and 9 subsamples.

Magnitudes for the subsamples are measured in the same manner as those for the individual dropouts in Section 2.1.1. To estimate uncertainties of the total fluxes (or the total magnitudes), we follow the three steps; 1) randomly selecting positions in the grid cell where the subsamples are located, 2) generating median-stacked sky noise images, and 3) performing aperture photometry on the sky noise images with the aperture correction to obtain the total flux f_i. The steps 1)-3) are repeated for 100 times. We make a histogram of f_i, and fit the histogram with a Gaussian profile. We regard the standard deviation divided by the median magnification factor of the subsample as the uncertainty of the total flux.

SED Fitting

To investigate the typical $M_\star$ for a given $M_{\rm UV}$, we conduct the SED fitting method based on the Markov Chain Monte Carlo (MCMC) algorithm. We use the `BEAGLE` tool (Chevallard & Charlot 2016), which is based on a recent version of the stellar population models of Bruzual & Charlot (2003) and the photoionization models of Gutkin et al. (2016) that are computed with `CLOUDY` (Ferland et al. 2013). The IGM absorption follow the models of Inoue et al. (2014). We adopt the Calzetti et al. (1994) law for dust attenuation.

There are five free parameters in the fitting: i) galaxy age $t_{\rm age}$, ii) galaxy-wide ionization parameter $U_{\rm ion}$, iii) total mass of the formed stars $M_\star$, iv) stellar metallicity Z, and v) V_{606}-band dust attenuation optical depth $\tau_{\rm V}$. We assume uniform prior probability distribution functions (PDFs) in the range of

$$1\ {\rm Myr} \leq t_{\rm age} \leq t_{\rm univ}(z = z_{\rm phot}^{\rm median}) - t_{\rm univ}(z = 20), \tag{2.2}$$

$$-3 \leq \log U_{\rm ion} \leq -1, \tag{2.3}$$

$$6 \leq \log(M_\star/M_\odot) \leq 11, \tag{2.4}$$

$$-2 \leq \log(Z/Z_\odot) \leq 0.2, \quad \text{and} \tag{2.5}$$

$$0 \leq \log \tau_{\rm V} \leq 2 \tag{2.6}$$

for the parameters i), ii), iii), iv), and v), respectively. Here, $z_{\rm phot}^{\rm median}$ is the median of the photometric redshifts $z_{\rm phot}$ of the subsample whose values are taken from Kawamata et al. (2018). We do not use $z_{\rm phot}$ less than 4 to derive $z_{\rm phot}^{\rm median}$ following their

Table 2.1 Summary of the subsamples.

Subsample	Threshold	N
$z \sim 6-7,\ M_{\rm UV} = -21.3$	$M_{\rm UV} \leq -21.0$	4
-20.6	$-21.0 \leq M_{\rm UV} \leq -20.5$	9
-20.2	$-20.5 \leq M_{\rm UV} \leq -20.0$	24
-19.7	$-20.0 \leq M_{\rm UV} \leq -19.5$	49
-19.2	$-19.5 \leq M_{\rm UV} \leq -19.0$	64
-18.8	$-19.0 \leq M_{\rm UV} \leq -18.5$	91
-18.3	$-18.5 \leq M_{\rm UV} \leq -18.0$	43
-17.7	$-18.0 \leq M_{\rm UV} \leq -17.5$	25
-17.3	$-17.5 \leq M_{\rm UV} \leq -17.0$	21
-16.6	$-17.0 \leq M_{\rm UV} \leq -16.0$	17
-15.1	$-16.0 \leq M_{\rm UV}$	9
$z \sim 8,\ M_{\rm UV} = -20.4$	$M_{\rm UV} \leq -20.0$	13
-19.7	$-20.0 \leq M_{\rm UV} \leq -19.5$	14
-19.3	$-19.5 \leq M_{\rm UV} \leq -19.25$	10
-19.1	$-19.25 \leq M_{\rm UV} \leq -19.0$	11
-18.7	$-19.0 \leq M_{\rm UV}$	17
$z \sim 9,\ M_{\rm UV} = -20.3$	$M_{\rm UV} \leq -19.9$	9
-19.6	$-19.9 \leq M_{\rm UV} \leq -19.5$	9
-19.3	$-19.5 \leq M_{\rm UV} \leq -19.1$	11
-18.7	$-19.1 \leq M_{\rm UV}$	11

Columns: (1) Subsample name that indicates the redshift and the median value of $M_{\rm UV}$. (2) Threshold of the subsample. (3) Number of the dropouts in the subsample.

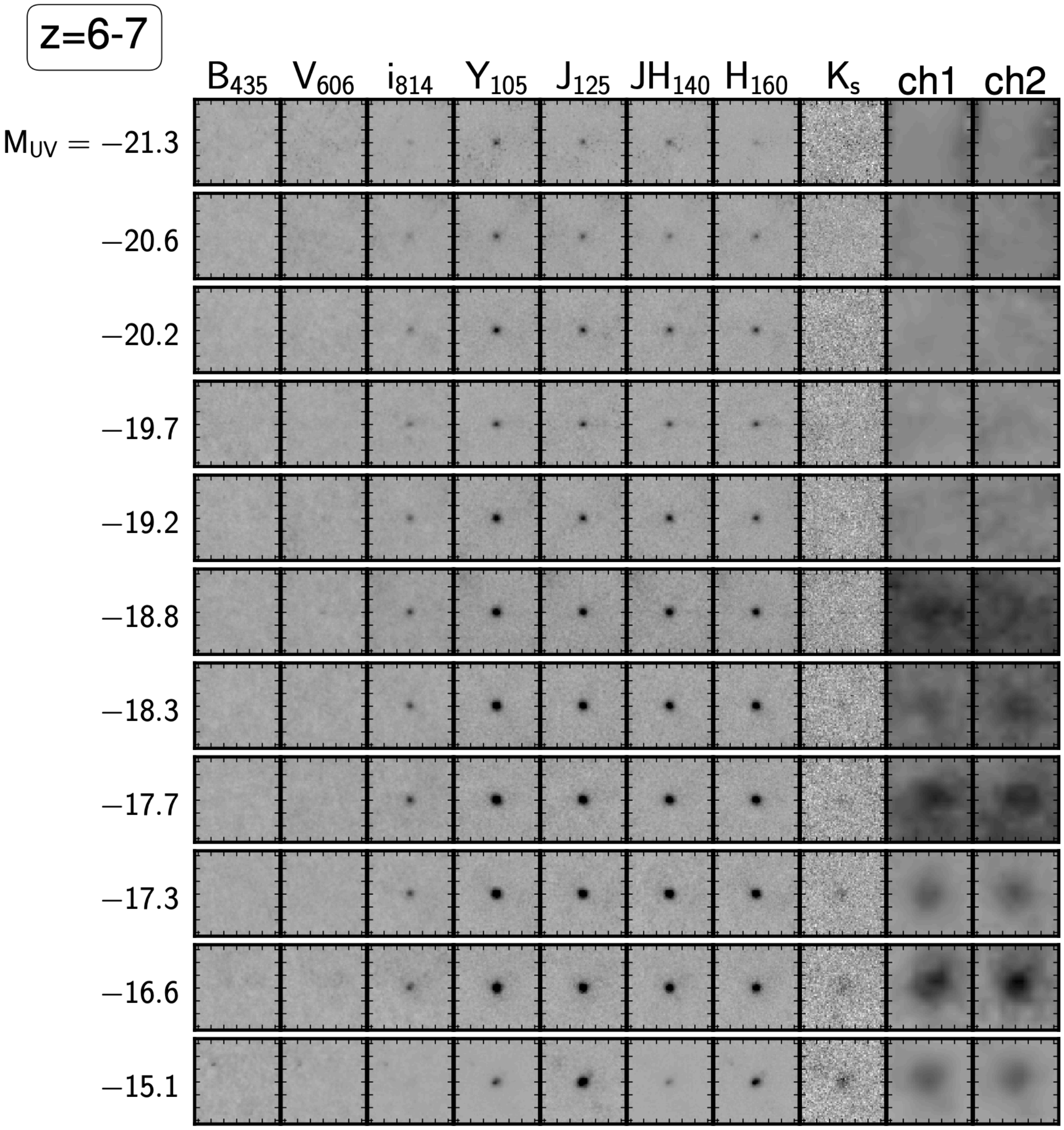

Figure 2.2 Stacked images of the $z \sim 6-7$ subsamples for each band. The image size is $4'' \times 4''$.

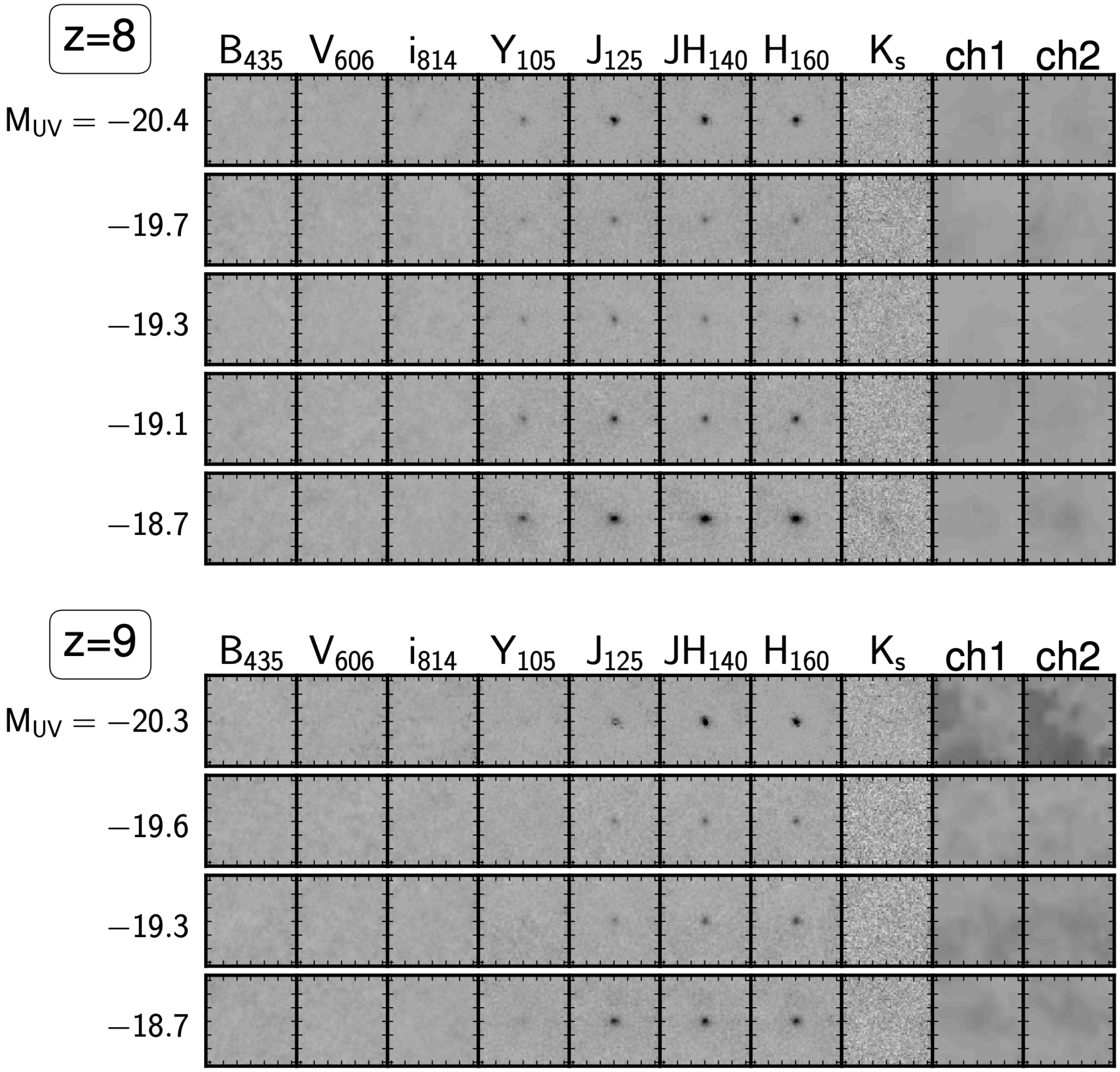

Figure 2.3 Same as Figure 2.2, but for $z \sim 8$ (top) and 9 (bottom) subsamples, respectively.

way. The age of the universe at z is represented by $t_{\rm univ}(z)$. The galaxy redshift is fixed to $z_{\rm phot}^{\rm median}$. The gas metallicity is assumed to equal the stellar metallicity. The dust-to-metal ratio is fixed to 0.3 (e.g., De Vis et al. 2017).

We assume a constant star formation history (SFH). Although we also test exponentially rising and declining SFHs $\psi(t) \propto \exp(t/\tau)$ where the time scale τ varies as the sixth free parameter, we find that the best-fit τ values are $\gtrsim 1$ Gyr in most of the subsamples. This is much greater than their best-fit galaxy ages $t_{\rm age}$ by $\gtrsim 1$ dex, implying that their SFHs are approximately constant. We confirm that the choice of SFHs does not significantly change the fitting results.

The posterior PDF $P(\boldsymbol{\Theta}|\boldsymbol{D},\mathsf{H})$ of a given parameter set $\boldsymbol{\Theta} = \{t_{\rm age}, U_{\rm ion}, M_\star, Z, \tau_{\rm V}\}$ of a model H is calculated based on the Bayes' theorem

$$P(\boldsymbol{\Theta}|\boldsymbol{D},\mathsf{H}) = \frac{P(\boldsymbol{\Theta}|\mathsf{H})P(\boldsymbol{D}|\boldsymbol{\Theta},\mathsf{H})}{\int \mathrm{d}\boldsymbol{\Theta} P(\boldsymbol{\Theta}|\mathsf{H})P(\boldsymbol{D}|\boldsymbol{\Theta},\mathsf{H})} \tag{2.7}$$

(e.g., Jeffreys 1961), where $\boldsymbol{D}$ is the data set, i.e., the fluxes in the B_{435}, V_{606}, i_{814}, Y_{105}, J_{125}, JH_{140}, H_{160}, $K_{\rm s}$, ch1, and ch2 bands. The likelihood function of $\boldsymbol{\Theta}$, $\mathcal{L}(\boldsymbol{\Theta}) \equiv P(\boldsymbol{D}|\boldsymbol{\Theta},\mathsf{H})$, is defined via

$$\ln \mathcal{L}(\boldsymbol{\Theta}) = -\frac{1}{2}\sum_k \left[\frac{f_k - \hat{f}_k(\boldsymbol{\Theta})}{\sigma_k}\right]^2. \tag{2.8}$$

Here f_k, $\hat{f}_k(\boldsymbol{\Theta})$, and σ_k are the observed flux, the flux predicted by the parameter set $\boldsymbol{\Theta}$, and the flux uncertainty, respectively. The subscript k runs over all of the bands. We do not use the i_{814}, Y_{105}, and J_{125} band for $z \sim 6-7$, 8, and 9 subsamples, respectively, because the photometries in these bands may be contaminated by unknown Lyα emission and IGM absorption effects. The value of σ_k is defined as

$$\sigma_k \equiv \sqrt{(\sigma_k^{\rm obs})^2 + (\sigma_0 f_k)^2}, \tag{2.9}$$

where $\sigma_k^{\rm obs}$ is the observational uncertainty, and σ_0 is the relative systematical uncertainty, e.g., errors in background subtraction, flux calibration, and model predictions (Brammer et al. 2008; Dahlen et al. 2013; Acquaviva et al. 2015; Chevallard & Charlot 2016). We define $\sigma_0 = 0.04$ (0.05) for the HST and $K_{\rm s}$ (IRAC) bands, applying the values recommended in the user manual of `BEAGLE` (Chevallard & Charlot 2016).

The posterior PDFs are efficiently sampled by the Nested Sampling algorithm implemented in the `MULTINEST` tool (Feroz & Hobson 2008; Feroz et al. 2009). We present the best-fit SEDs with the data photometries for $z \sim 6-7$, 8, and 9 subsamples in Figure 2.4.

We quickly test any potential biases in our sample and method here. This is motivated by the fact that the shapes of the SMFs largely differ between the star-forming and quiescent galaxies (e.g., Ilbert et al. 2013; Muzzin et al. 2013; Kelvin et al. 2014; Tomczak et al. 2014). Because our dropouts are selected with the Lyman break technique, they are likely to be star-forming. We confirm that this is not affected by the stacking analysis, because the star-formation rate (SFR) to $M_\star$ relations derived with the stacked photometries are on the track of the star-forming galaxy "main sequence" (Figure 2.5). For example, we confirm that the SFR-$M_\star$ relation of our $z \sim 6-7$ dropouts agrees well with those of the star-forming galaxies taken from the literature (Salmon et al. 2015; Santini et al. 2017). Additionally, our dropouts follow the main sequence obtained with multiple observations (Speagle et al. 2014).

Stellar Mass to UV Luminosity Relations

Figure 2.6 shows the $M_\star$-$M_{\rm UV}$ relations. Here, $M_\star$ and $M_{\rm UV}$ represent the median value of the marginal posterior PDF and the median value of the UV magnitudes of the dropouts in the subsample, respectively. The vertical error bars represent 68 % confidence intervals, while the horizontal bars show the minimum and maximum values of $M_{\rm UV}$ of the dropouts in the subsamples. Figure 2.6 indicates that our results are broadly consistent with the previous results.

We fit a linear function

$$\log(M_\star/M_\odot) = a_0 + a_1(M_{\rm UV} + 19.5), \tag{2.10}$$

where the intercept a_0 and the slope a_1 are set as free parameters, to our data in the magnitude range of $-21 \leq M_{\rm UV} \leq -16$. The black solid lines in Figure 2.6 show the best-fit relations. At $z \sim 6-7$, we find that the best-fit parameters are $(a_0, a_1) = (8.83^{+0.14}_{-0.15}, -0.48^{+0.12}_{-0.10})$, which is comparable to those obtained in the previous studies (e.g., Duncan et al. 2014; Song et al. 2016; Bhatawdekar et al. 2019).

At $z \sim 8$ and 9, we fix a_1 to the best-fit value at $z \sim 6-7$ $(= -0.48)$, because the

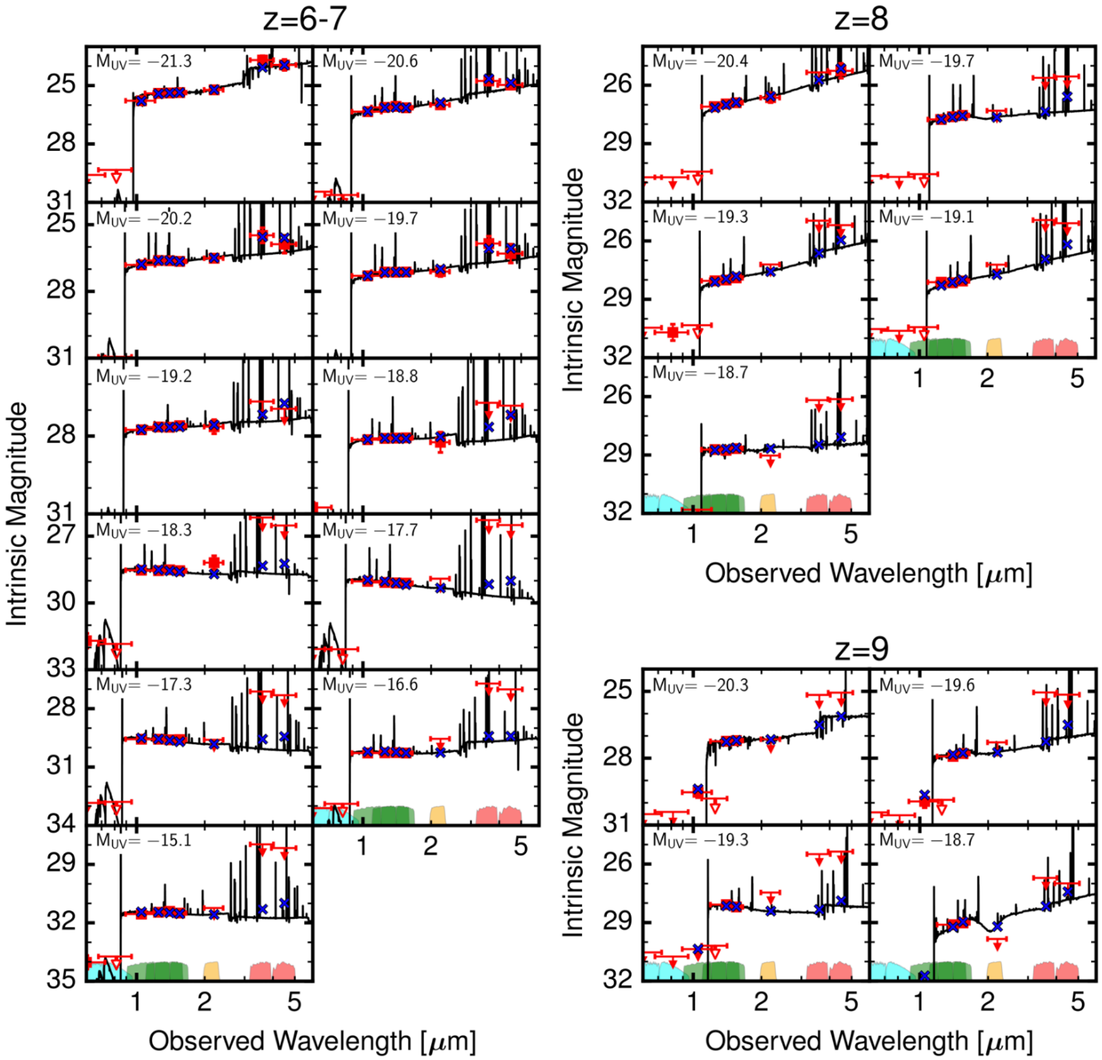

Figure 2.4 Intrinsic SEDs of the $z \sim 6-7$ (left), 8 (right top), and 9 (right bottom) subsamples. The subsample names are denoted at the upper-left corner in each panel. The red filled squares and down arrows show the photometric data points and 2σ upper limits obtained in Section 2.1.2. The open arrows are not included in the likelihood calculation (see text). The horizontal and vertical error bars represent the wavelength range of the filters and the 1σ uncertainties, respectively. The black lines represent the best-fit SEDs, while the blue crosses show the bandpass-averaged magnitudes predicted from the best-fit SEDs. The color shades denote the normalized filter throughputs.

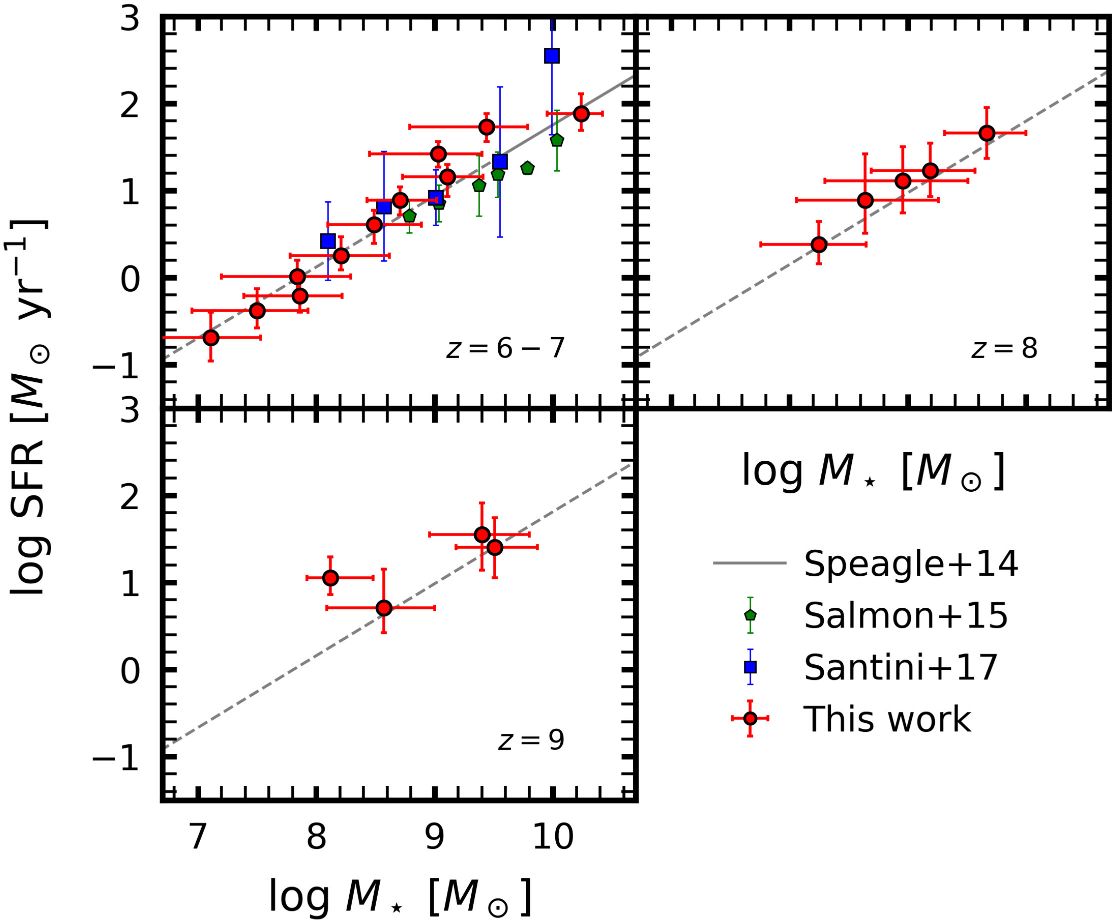

Figure 2.5 SFR versus $M_\star$ relations at $z \sim 6-7$ (left top), 8 (right top), and 9 (left bottom). The red circles show our dropouts, while the green pentagons and blue boxes are taken from Salmon et al. (2015) and Santini et al. (2017), respectively. The solid gray line shows the best-fit relations derived by Speagle et al. (2014), who compile multiple observational studies at $z \leq 6$ (the dotted is the extrapolation).

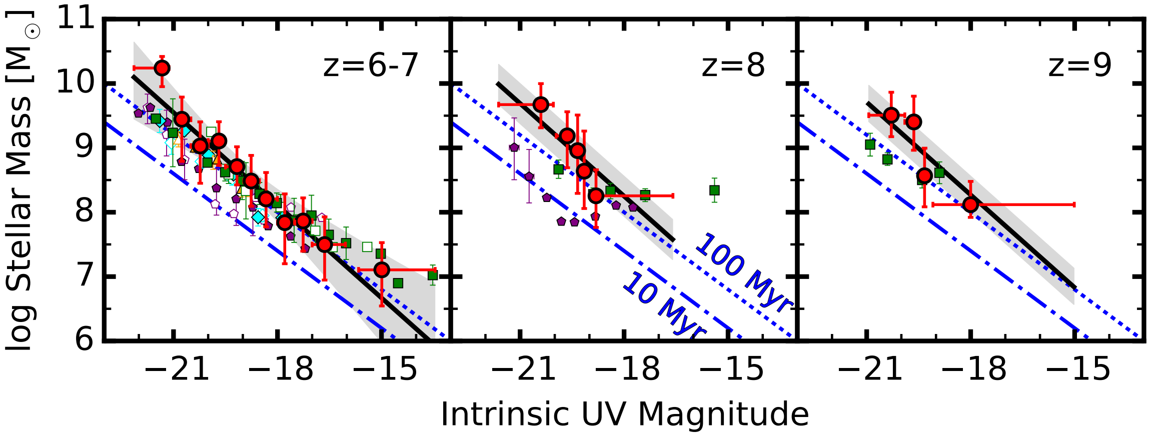

Figure 2.6 Distribution of $M_\star$ versus $M_{\rm UV}$ of the $z\sim 6-7$ (left), 8 (middle), and 9 (right) subsamples. The red filled circles represent our results. The black lines and the gray shades denote the best-fit relations and the 1σ uncertainties, respectively. The other data points are taken from the previous studies, Stark et al. (2013, orange triangles), Duncan et al. (2014, cyan diamonds), Song et al. (2016, purple pentagons), and Bhatawdekar et al. (2019, green boxes). In the left panel, the filled and open symbols show the data at $z\sim 6$ and 7, respectively. The blue dashed and dotted lines show the models of 10 and 100 Myr star formation duration time (Bouwens et al. 2017a).

fitting is unstable due to the lack of data points. We find that the best-fit values are $a_0 = 8.97 \pm 0.21$ and 8.99 ± 0.19 at $z \sim 8$ and 9, respectively. The best-fit values of a_0 present no significant redshift evolution beyond the uncertainties, which indicates that stellar populations of the dropouts do not significantly change at $z \sim 6-9$ in the magnitude range considered here. When a_1 is not fixed in the fitting, a_0 slightly becomes steeper especially at $z \sim 8$. This might lead to the flatter low-mass-end slope of the SMF.

In Figure 2.6, the blue dashed and dotted lines denote the $M_\star$-$M_{\rm UV}$ relations that are assumed in Bouwens et al. (2017a). These lines correspond to stellar populations with star-formation duration times of 10 and 100 Myr, which correspond to $(a_0, a_1) = (8.0, -0.4)$ and $(8.6, -0.4)$, respectively. We find that our best-fit $M_\star$-$M_{\rm UV}$ relations (the black solid lines) are comparable to the 100-Myr star formation model. The 10-Myr model falls below our best-fit relation by $\sim 5\sigma$ difference. We use these models in Section 5.3.

2.1.3 Results

We use the $M_\star$-$M_{\rm UV}$ relations to derive the SMFs, following Song et al. (2016) and Bhatawdekar et al. (2019). We apply the best-fit $M_\star$-$M_{\rm UV}$ relations (Section 2.1.2) to the LFs $\Phi_{\rm UV}(M_{\rm UV})$ of Ishigaki et al. (2018, Section 3.1) in the following way. For a given data point $(M_{\rm UV},\ \Phi_{\rm UV}(M_{\rm UV}))$ of the Ishigaki et al. (2018) LFs, we first derive $M_\star$ from the value of $M_{\rm UV}$ using the best-fit $M_\star$-$M_{\rm UV}$ relation and its uncertainty (represented as the solid black line and the gray shade in Figure 2.6). We next convert $\Phi_{\rm UV}(M_{\rm UV})$ value to $\Phi_\star(M_{\rm UV})$ in the same manner but with accounting for the uncertainties both from the best-fit $M_\star$-$M_{\rm UV}$ relation and the LF. Repeating this process for every $M_{\rm UV}$ of the data point yields the SMF $\{(M_\star(M_{\rm UV}),\ \Phi_\star(M_{\rm UV}))\}$. We show our SMFs in Figure 2.7 with the red filled circles. The red open circles and the arrows also represent our SMFs, but with the extrapolated $M_\star$-$M_{\rm UV}$ relations (the arrows represent the upper limits). The magnitude ranges of the $M_\star$-$M_{\rm UV}$ relations do not fully cover those of the UV LFs, presumably because we use only part of the dropouts used for the UV LFs.

We confirm that our SMFs roughly agree with those of previous studies in the range of $M_\star \sim 10^7 - 10^9\ M_\odot$, especially at $z \sim 6-7$. We note the slight discrepancies in the SMFs at $z \sim 8$ and 9; for example, the $z \sim 8$ SMFs of Stefanon et al. (2021)

and our work exceed that of Song et al. (2016), and our $z \sim 9$ SMF is larger than that of Stefanon et al. (2021). These are possibly because of the difficulty in determining photometric redshifts, and/or the contamination by strong nebular lines in IRAC bands. In the low-mass end, our SMFs reach $M_\star \sim 10^6\ M_\odot$, which is lower than those of the previous studies by $\gtrsim 1$ dex. Turnovers are not identified above the current mass limits.

The error bars of our SMFs are smaller especially for $z \sim 8$ and 9 compared to those of previous results. This is probably because the number of our dropouts is larger than the previous work. For example, the number of dropouts at $z \sim 9$ is 39 and 9 in this work and Bhatawdekar et al. (2019, green boxes in Figure 2.7), respectively. It may also be attributed to the systematic uncertainties of the magnification factors, because our error bars represented here only include the statistical uncertainties in the magnitude measurements.

We parametrize our SMFs with a Schechter (1976) function,

$$\begin{aligned}\Phi_\star(\log M_\star)\mathrm{d}\log M_\star \\ = \ln(10)\phi_\star^* 10^{(\alpha_\star+1)(\log M_\star - \log M_\star^*)} \exp(-10^{\log M_\star - \log M_\star^*})\mathrm{d}\log M_\star,\end{aligned} \tag{2.11}$$

where the characteristic stellar mass $M_\star^*$, the low-mass-end slope $\alpha_\star$, and the normalization $\phi_\star^*$ are free parameters. We estimate the best-fit values of the parameters of the Schechter functions by running the MCMC sampling. We limit sampling space to the product space of $8 \leq \log(M_\star^*/M_\odot) \leq 12$, $\alpha_\star > -5$, and $-9 \leq \log(\phi_\star^*/[\mathrm{dex}^{-1}\,\mathrm{Mpc}^{-3}]) \leq -3$. Because the high-mass ends of the SMFs are poorly constrained due to the lack of bright dropouts, we take a log-normal prior on $\log(M_\star^*/M_\odot)$ with the mode of 10.75 and the standard deviation of 0.3, following the results of Song et al. (2016) at $z = 4-5$. The posterior PDFs are sampled with the affine invariant sampling algorithm implemented in the `emcee` package (Foreman-Mackey 2016). To improve the statistical accuracy, we fit Schechter functions simultaneously to our SMFs and the SMFs derived by Song et al. (2016) who use the CANDELS/GOODS and the HUDF data, at $z \sim 6-7$ and 8. The sample of Song et al. (2016) is selected with the photometric redshifts in Finkelstein et al. (2015) and our dropouts are selected with the Lyman breaks. Nonetheless, these techniques produce similar sample properties (Finkelstein et al. 2015; Stefanon et al. 2017), which allows us to combine the data of Song et al. (2016) and ours.

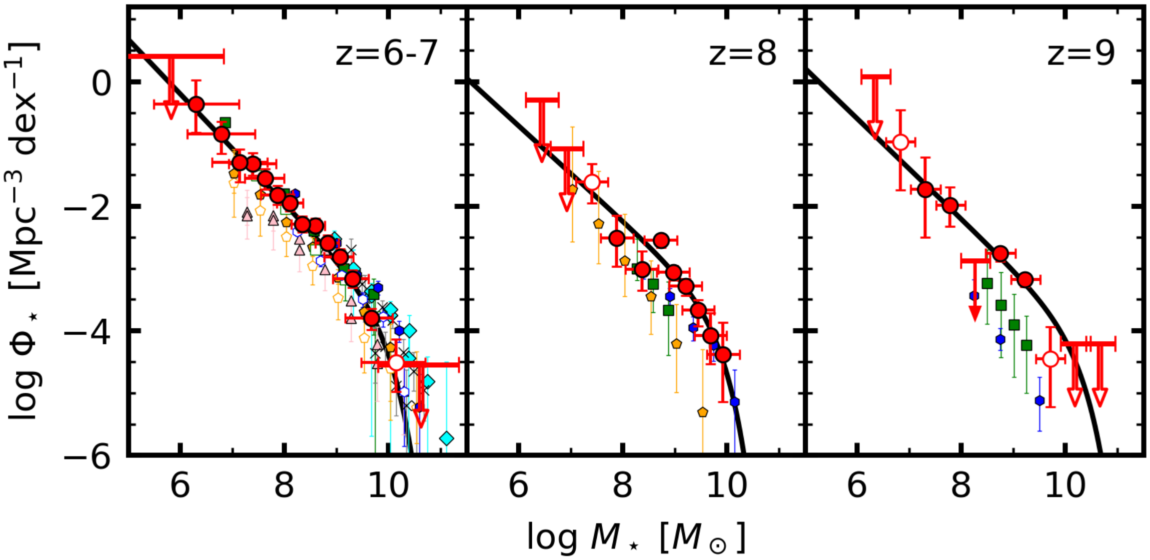

Figure 2.7 SMFs at $z \sim 6-7$ (left), 8 (middle), and 9 (right). The red filled circles show our SMFs, reaching down to $\sim 10^6\ M_\odot$ and $10^8\ M_\odot$ at $z \sim 6-7$ and $8-9$, respectively. The red open circles and the red open down arrows also represent our SMFs, but we extrapolate the best-fit $M_\star$-$M_{\rm UV}$ relations to derive the SMFs. The down arrows denote the upper limits of the SMFs. The other data points are taken from the previous studies, González et al. (2011, magenta triangles), Duncan et al. (2014, cyan diamonds), Grazian et al. (2015, black crosses), Song et al. (2016, orange pentagons), Bhatawdekar et al. (2019, green boxes), and Stefanon et al. (2021, blue hexagons). In the left panel, the filled and open symbols show the SMFs at $z \sim 6$ and 7, respectively. The black curves represent the best-fit Schechter functions to our SMFs at $z \sim 6-7$, 8, and 9, combined with those of Song et al. (2016) at $z \sim 6-7$ and 8.

Table 2.2 summaries the best-fit parameters at $z \sim 6-9$. Our measurements of $\log M_\star^*$ are broadly consistent with the previous work of Duncan et al. (2014), Grazian et al. (2015), Song et al. (2016), Bhatawdekar et al. (2019), and Stefanon et al. (2021) at $z \sim 6-9$. Our $\alpha_\star$ value is shallower than those in the previous studies, which is possibly attributed to the new constraints on the low-mass range of the SMFs.

2.2 SMF at $z \sim 0$

2.2.1 Data

We focus on the local galaxies that are spectroscopically observed with the SDSS, Baryon Oscillation Spectroscopic Survey (BOSS; Dawson et al. 2013), and extended BOSS (eBOSS; Ross et al. 2020). The values of $M_\star$ are taken from the Firefly catalog (Comparat et al. 2017), which is one of the Value-Added Catalogs included in the SDSS Data Release (DR) 16. The catalog provides stellar population properties of the sources, such as ages, metallicities, and $M_\star$, obtained by performing the `FIREFLY` SED fitting code (Wilkinson et al. 2017).

We choose secure galaxies from the catalog by applying the following criteria:

- The morphological flag (`type`) indicates `GALAXY`.
- The spectral type flags (`class` and `CLASS_NOQSO`) indicate `GALAXY`.
- The spectra should be clean (`clean` $= 1$).
- The measurement of spectroscopic redshift z is reliable (`z` $>$ `zErr` > 0 and `zWarning` $= 0$).

These flags are defined in the SDSS reduction pipeline. This selection results in 2362018 galaxies, which we hereafter refer to as the spectroscopic galaxies. The distribution of $M_\star$ and z are shown with the small gray dots in Figure 2.8. We particularly focus on the galaxies with $10^6 \leq M_\star/M_\odot \leq 10^{12}$ and at $0.003 \leq z \leq 0.2$. We choose 0.003 such that the cosmic expansion rate cz, where c is the speed of light in vacuum, is large enough compared to galaxies' peculiar motions. We arbitrarily set 0.2 for fair comparisons with literature (Wright et al. 2017; Rodríguez-Puebla et al. 2020), but this choice is unlikely to affect our main results, because most of our

Table 2.2 Best-fit parameters of the Schechter function of the SMFs.

Reference	$\log M_\star^*$ $[M_\odot]$	$\alpha_\star$	$\phi_\star^*$ $[10^{-5}\ \mathrm{dex}^{-1}\ \mathrm{Mpc}^{-3}]$
$z \sim 6$			
This work	$9.80^{+0.28}_{-0.17}$	-1.88 ± 0.07	$12.8^{+9.7}_{-7.3}$
Duncan et al. (2014)	$10.87^{+1.13}_{-1.06}$	$-2.00^{+0.57}_{-0.40}$	$1.4^{+41.1}_{-1.4}$
Grazian et al. (2015)	10.49 ± 0.32	-1.55 ± 0.19	$6.19^{+13.50}_{-4.57}$
Song et al. (2016)	$10.72^{+0.29}_{-0.30}$	$-1.91^{+0.09}_{-0.09}$	$1.35^{+1.66}_{-0.75}$
Bhatawdekar et al. (2019)*	$10.29^{+0.48}_{-0.56}$	$-1.93^{+0.05}_{-0.07}$	$5.63^{+7.12}_{-3.23}$
Stefanon et al. (2021)	$10.03^{+0.08}_{-0.11}$	$-1.88^{+0.06}_{-0.03}$	$8.13^{+3.89}_{-1.96}$
$z \sim 7$			
Duncan et al. (2014)	10.51 (fixed)	$-1.89^{+1.39}_{-0.61}$	$3.6^{+30.1}_{-3.5}$
Grazian et al. (2015),	10.69 ± 1.58	-1.88 ± 0.36	$0.57^{+59.68}_{-0.57}$
Song et al. (2016)	$10.78^{+0.29}_{-0.28}$	$-1.95^{+0.18}_{-0.18}$	$0.53^{+1.10}_{-0.38}$
Bhatawdekar et al. (2019)*	$10.25^{+0.45}_{-0.49}$	$-1.95^{+0.06}_{-0.07}$	$2.82^{+5.16}_{-1.88}$
Stefanon et al. (2021)	$9.83^{+0.15}_{-0.13}$	-1.73 ± 0.08	$7.24^{+3.98}_{-2.98}$
$z \sim 8$			
This work	$9.67^{+1.10}_{-0.33}$	$-1.76^{+0.21}_{-0.19}$	$13.2^{+25.6}_{-12.5}$
Song et al. (2016)	$10.72^{+0.29}_{-0.29}$	$-2.25^{+0.72}_{-0.35}$	$0.035^{+0.246}_{-0.030}$
Bhatawdekar et al. (2019)*	$10.48^{+0.90}_{-0.75}$	$-2.25^{+0.23}_{-0.29}$	$0.089^{+0.36}_{-0.074}$
Stefanon et al. (2021)	$9.77^{+0.44}_{-0.24}$	$-1.82^{+0.20}_{-0.21}$	$2.04^{+3.09}_{-1.65}$
$z \sim 9$			
This work	$10.11^{+1.24}_{-0.70}$	$-1.81^{+0.21}_{-0.18}$	$4.0^{+32.0}_{-5.0}$
Bhatawdekar et al. (2019)*	$10.45^{+0.80}_{-0.85}$	$-2.33^{+0.30}_{-0.39}$	$0.06^{+0.66}_{-0.06}$
Stefanon et al. (2021)	9.29 (fixed)	−2 (fixed)	0.76 ± 0.20

* We take the “point source” results from Bhatawdekar et al. (2019).

low-mass galaxies are at $z < 0.1$ (Figure 2.8). The galaxies with $M_\star < 10^6\ M_\odot$ are not used here, because the number is insufficient to accurately derive the SMF.

We note that some previous studies at $z \sim 0$ exclude galaxies whose $M_\star$ is smaller than the $\sim 10-20$ percentile mass at each z (e.g., Moustakas et al. 2013; Muzzin et al. 2013; Tomczak et al. 2014). Because we confirm that this selection does not largely affect our SMF, we do not apply this selection here.

2.2.2 Methods

Completeness

The completeness of the sample ($C_{\rm tot}$) consists of the detection completeness ($C_{\rm det}$) and redshift ($C_{\rm specz}$) completeness via $C_{\rm tot} = C_{\rm det} \times C_{\rm specz}$. These are measured as functions of SDSS `cModel` apparent magnitudes in the r band (m_r). We present the completeness in Figure 2.9.

The detection completeness $C_{\rm det}$ is taken from the SDSS homepage.[4] We show $C_{\rm det}$ with the dotted line in the bottom panel. Since $C_{\rm det}$ is ~ 100 % in the magnitude range considered here, $C_{\rm tot}$ is almost equivalent to $C_{\rm specz}$.

To estimate $C_{\rm specz}$, we use the SDSS optical photometric catalog. We select secure photometric galaxies such that they meet `z` $>$ `zErr` > 0, $0.003 \leq$ `z` ≤ 0.2, and `clean` $= 1$ for a fair comparison to the spectroscopic galaxies. We define $C_{\rm specz}$ as the number fraction of the spectroscopic to photometric galaxies, following Wyder et al. (2005). The number distributions of these galaxies and $C_{\rm specz}$ are shown in the top and bottom panels, respectively.

We choose the spectroscopic galaxies brighter than $m_r = 17.8$ mag to ensure high completeness ($C_{\rm tot} > 50$ %). We note that this magnitude is much brighter than the detection limit (22.7 mag at 5σ).[4] The galaxies brighter than $m_r = 11.5$ mag are also excluded, because $C_{\rm tot}$ cannot be defined due to the insufficient number of the photometric galaxies at $m_r < 11.5$ mag. The final sample consists of 651202 galaxies, which are shown with the black dots in Figure 2.8.

---

[4] https://www.sdss.org/dr16/imaging/other_info/

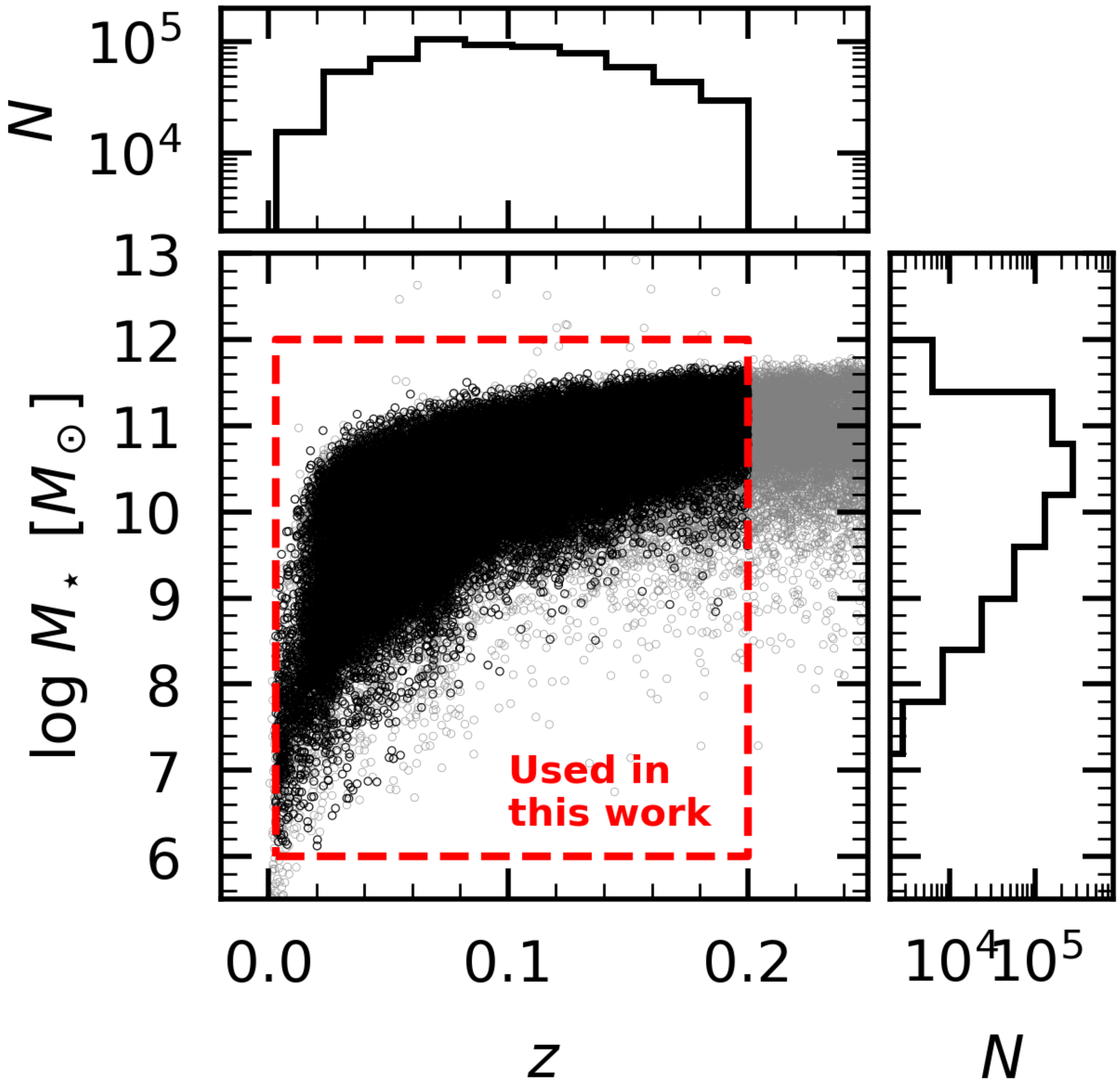

Figure 2.8 **Center:** $M_\star$-z distributions. The black dots show our final sample, which is selected from the original secure galaxies (small gray dots). Our final sample is defined as the secure galaxies meeting $0.003 \leq z \leq 0.2$, $10^6 \leq M_\star/M_\odot \leq 10^{12}$, and $11.5 \leq m_r \leq 17.8$ (see text). **Top and Right:** z and $M_\star$ histograms of the sample, respectively.

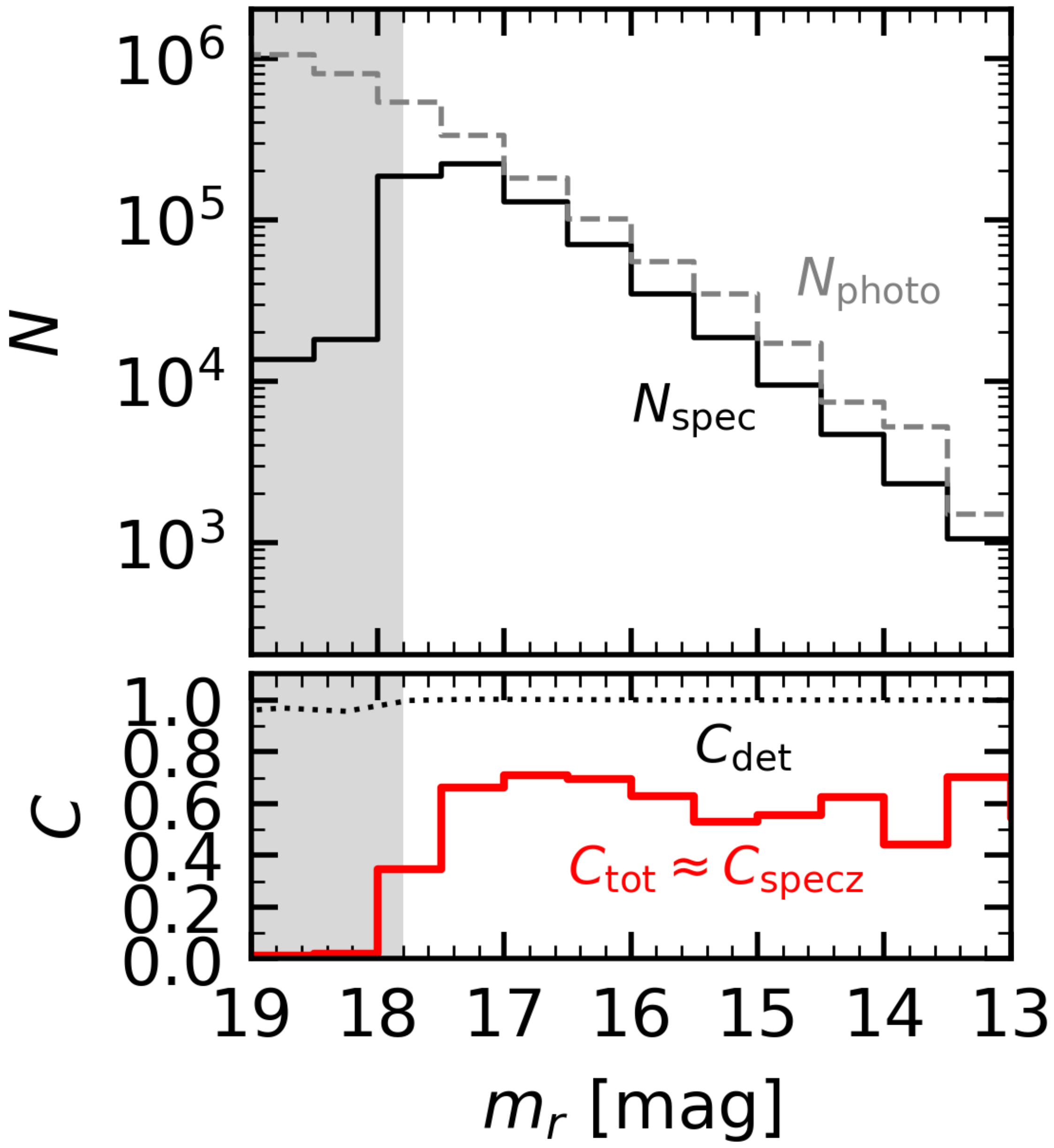

Figure 2.9 **Top:** Histograms of the spectroscopic and photometric galaxies ($N_{\rm spec}$ and $N_{\rm photo}$, respectively). We use $N_{\rm spec}/N_{\rm photo}$ to define $C_{\rm specz}$. **Bottom:** Completeness. The black dotted, black dashed, and red solid lines show $C_{\rm det}$, $C_{\rm specz}$, and $C_{\rm tot}$, respectively. We note that the black dashed line is almost overlapped by the red solid line, i.e., $C_{\rm tot} \sim C_{\rm specz}$, because $C_{\rm det}$ is almost 100 % over the m_r range here. The gray shade represents the area where $C_{\rm tot} \leq 50$ %.

$1/V_{\rm max}$ Method

We use the traditional $1/V_{\rm max}$ method (Schmidt 1968; Felten 1976; Steidel et al. 1999) to derive the SMF. We derive the maximum cosmic volumes of the i-th object, $V_{{\rm max},i}$, via

$$V_{{\rm max},i}(M_{r,i}) = \Omega \int_{z_{\rm l}}^{z_{\rm u}} C_{\rm tot}(m_r(M_{r,i}, z)) \frac{{\rm d}V}{{\rm d}z} {\rm d}z, \tag{2.12}$$

where the object has the absolute magnitude $M_{r,i}$. The angular area of the survey, Ω, is 9376 deg^2.[5] The integral range is $z_{\rm l} \leq z \leq z_{\rm u}$, where $z_{\rm l} \equiv \max(0.03, z_{\rm min})$ and $z_{\rm u} \equiv \min(0.2, z_{\rm max})$. We derive $z_{\rm min}$ and $z_{\rm max}$ by solving

$$M_{r,i} + 5\log[d_{\rm L}(z_{\rm min})/10~{\rm pc}] + K(z_{\rm min}) = m_{r,{\rm l}} \tag{2.13}$$

and

$$M_{r,i} + 5\log[d_{\rm L}(z_{\rm max})/10~{\rm pc}] + K(z_{\rm max}) = m_{r,{\rm u}}, \tag{2.14}$$

where $m_{r,{\rm l}} = 11.5$ and $m_{r,{\rm u}} = 17.8$ mag. Lastly,

$$\frac{{\rm d}V}{{\rm d}z}(z) = \frac{c}{H_0} \frac{\rm d}{{\rm d}z} \int_0^z \frac{{\rm d}z'}{\sqrt{\Omega_{{\rm m},0}(1+z'^3) + \Omega_{\Lambda,0}}} \tag{2.15}$$

is the differential comoving volume (Hogg 1999). The SMF $\Phi_\star$ is derived as

$$\Phi_\star(\log M_\star) = \frac{1}{\Delta(\log M_\star)} \sum_{i=1}^{N} \frac{1}{V_{{\rm max},i}}. \tag{2.16}$$

Here i runs over the galaxies in the stellar mass bin between $\log M_\star - \Delta(\log M_\star)/2$ and $\log M_\star + \Delta(\log M_\star)/2$. We assume the Poisson uncertainty:

$$\sigma(\Phi_\star) = \frac{1}{\Delta(\log M_\star)} \sqrt{\sum_{i=1}^{N} \frac{1}{V^2_{{\rm max},i}}}. \tag{2.17}$$

2.2.3 Results

Figure 2.10 shows our SMF at $z \sim 0$ and those taken from the previous studies of Baldry et al. (2012), Kelvin et al. (2014), Wright et al. (2017), and Rodríguez-Puebla

---

[5] https://www.sdss.org/dr16/scope/

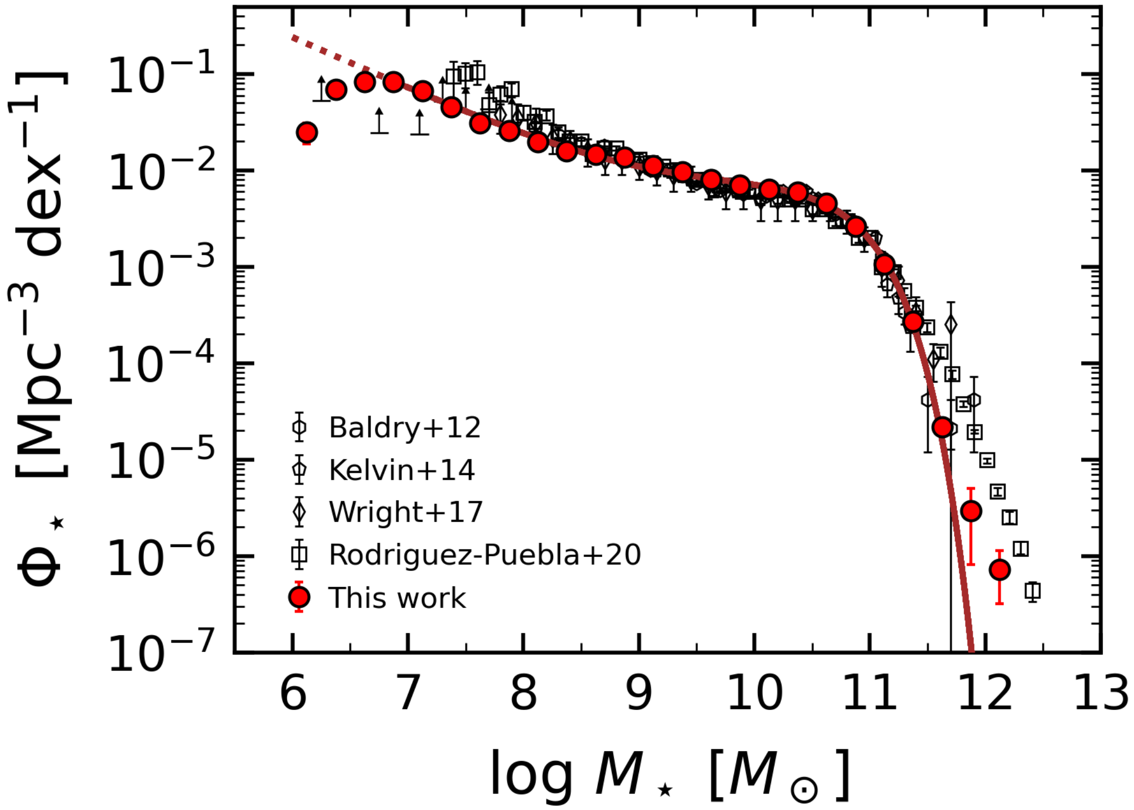

Figure 2.10 SMFs at $z \sim 0$. The red circles show our SMF, while the black symbols are taken from the previous work of Baldry et al. (2012, hexagons and up arrows), Kelvin et al. (2014, pentagons), Wright et al. (2017, diamonds), and Rodríguez-Puebla et al. (2020, squares). The brown solid and dotted lines represent our best-fit double Schechter function and its extrapolation, respectively.

et al. (2020). In the moderate stellar mass range ($10^8 < M_\star/M_\odot < 10^{11}$), our SMF agrees well with those taken from the literature. In the high-mass range, our SMF at $M_\star \lesssim 10^{11.5}\ M_\odot$ agree with those of Baldry et al. (2012), Kelvin et al. (2014), and Wright et al. (2017). There are slight discrepancies of the SMFs among the studies at the massive ends ($M_\star \gtrsim 10^{11.5}\ M_\odot$) due to the lack of galaxies at this mass range. The SMF of Rodríguez-Puebla et al. (2020) lies much above ours, probably because their $M_\star$ values are based on uncertain mass-to-light ratios. Additionally, the discrepancies may also be caused by whether the samples include active galactic nuclei (AGNs) or not; we explicitly exclude AGNs (Section 2.2.1), while no relevant descriptions are found in the literature.

At the low-mass end, our SMF reaches $M_\star \sim 10^6\ M_\odot$ for the first time. Although the SMF of Baldry et al. (2012) also reaches $\sim 10^6\ M_\odot$ including the lower limits, their SMF at $M_\star < 10^7\ M_\odot$ is based on only 28 galaxies (see their Table 1). We use much more 995 galaxies in the same $M_\star$ range. Thanks to the update of the mass limit, we find a clear turnover at $M_\star \sim 10^6 - 10^7\ M_\odot$ for the first time.

The turnover is reliable, because the data points in the three lowest-mass bins are below the extrapolation from the massive side (the dotted brown line) by 29.3, 6.3, and 2.4σ levels. Although we use galaxies brighter than $m_r = 17.8$ (Section 2.2.2), we confirm that our sample recovers ~ 70 % of the sources with no magnitude cut. This suggests that the turnover is also robust against the sample selection. We quantify the turnover mass and discuss the physical origin in detail in Section 5.2.1.

We parametrize our SMF with a double Schechter function, which has often been used for SMFs at $z < 3$ (e.g., Baldry et al. 2008; Pozzetti et al. 2010; Baldry et al. 2012; Bielby et al. 2012; Ilbert et al. 2013; Moustakas et al. 2013; Muzzin et al. 2013; Tomczak et al. 2014; Davidzon et al. 2017). A double Schechter function is given as the sum of two single Schechter functions (Equation 2.11) sharing the same characteristic stellar mass $M_\star^*$, i.e.,

$$\begin{aligned}\Phi_\star(\log M_\star)\mathrm{d}\log M_\star \\ = \Phi_{\star,\mathrm{Sch}}(\log M_\star; M_\star^*, \alpha_{\star,\mathrm{low}}, \phi^*_{\star,\mathrm{low}}) + \Phi_{\star,\mathrm{Sch}}(\log M_\star; M_\star^*, \alpha_{\star,\mathrm{high}}, \phi^*_{\star,\mathrm{high}}).\end{aligned} \tag{2.18}$$

Here, the two term of $\Phi_{\star,\mathrm{Sch}}$ are single Schechter functions with $\alpha_{\star,\mathrm{low}} + 1 < 0$ and $\alpha_{\star,\mathrm{high}} + 1 > 0$. We refer to the first and second terms as the low- and high-mass components, respectively. The high-mass component is implemented to reproduce the knee-like shape at $M_\star \sim 10^{10} - 10^{11}\ M_\odot$ in the SMF. In fitting, we only use the data points with $M_\star$ larger than the turnover mass.

The best-fit parameters are compared with those obtained in the literature in Figure 2.11 and Table 2.3. We find that our SMF has the best-fit $\alpha_{\star,\mathrm{low}}$ as faint as $-1.54^{+0.09}_{-0.08}$, which is comparable to the previous studies (e.g., Baldry et al. 2012; Kelvin et al. 2014; Wright et al. 2017).

The best-fit value of our $M^*_\star$ is 10.82 ± 0.01, which agrees with those of Wright et al. (2017) and Rodríguez-Puebla et al. (2020). Our $M^*_\star$ value is slightly larger than those of Baldry et al. (2012) and Kelvin et al. (2014), which may be affected by our new data points at $M_\star \gtrsim 10^{11.5}\ M_\odot$.

2.3 Redshift Evolution of SMFs

To investigate the redshift evolution of the SMFs, we compare our SMFs at $z \geq 6$ (Section 2.1) and $z \sim 0$ (Section 2.2), together with those taken from the literature, in Figure 2.12. The SMFs at $z = 1.2$ and 2.2 are taken from Davidzon et al. (2017), those at $z \sim 4$ and 5 from Song et al. (2016), and that at $z \sim 10$ from Stefanon et al. (2021). We focus on these results because they reach the lowest $M_\star$ at each redshift among the existing literature. Our SMFs at $z \sim 6 - 9$ are only available in low mass regimes, we complementarily show the SMFs of González et al. (2011) at $z \sim 6$ and those of Stefanon et al. (2021) at $z \sim 8$ and 9. These SMFs are shown in the top panel. We also show the best-fit Schechter functions with the colored lines, the redshift evolution of whose parameters are displayed with the filled circles in the bottom panels. We also plot the results taken from Grazian et al. (2015) and Bhatawdekar et al. (2019) with the open circles as references. The $\alpha_\star$ values at $z < 3$ are of the low-mass component of the double Schechter functions, and the $\phi^*_\star$ at $z < 3$ refers to the sum of $\phi^*_{\star,\mathrm{low}}$ and $\phi^*_{\star,\mathrm{high}}$ at each z.

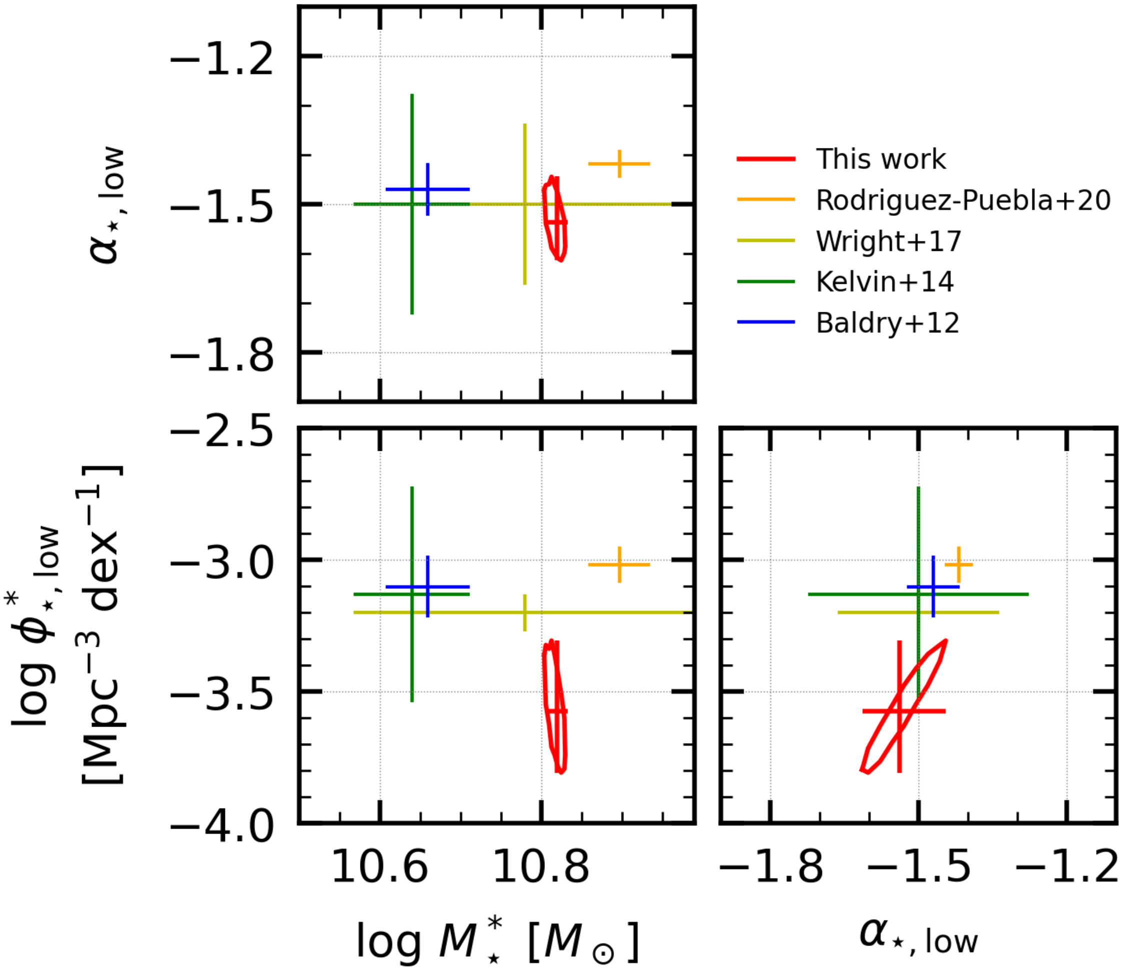

Figure 2.11 Confidence intervals of the parameters of the low-mass components of the double Schechter functions at $z \sim 0$. The red contour and crosses show the 3σ confidence intervals of our SMF, while the other crosses represent the 1σ confidence intervals of the SMFs taken from the previous studies (Baldry et al. 2012; Kelvin et al. 2014; Wright et al. 2017; Rodríguez-Puebla et al. 2020). We note that Rodríguez-Puebla et al. (2020) combines a modified Schechter function at the low-mass end and a power law at the massive end; the intervals shown here are for the modified Schechter function.

Table 2.3 Best-fit parameters of the double Schechter functions of the $z \sim 0$ SMFs.

Reference (1)	$\log M_\star^*$ $[M_\odot]$ (2)	$\alpha_{\star,\mathrm{low}}$ (3)	$\phi_{\star,\mathrm{low}}^*$ $[10^{-3}\ \mathrm{Mpc}^{-3}\ \mathrm{dex}^{-1}]$ (4)	$\alpha_{\star,\mathrm{high}}$ (5)	$\phi_{\star,\mathrm{high}}^* \times 10^{-3}$ $[10^{-3}\ \mathrm{Mpc}^{-3}\ \mathrm{dex}^{-1}]$ (6)
This work	10.82 ± 0.01	$-1.54^{+0.09}_{-0.08}$	$0.27^{+0.23}_{-0.11}$	$-0.91^{+0.06}_{-0.04}$	$3.39^{+0.11}_{-0.19}$
Rodríguez-Puebla et al. (2020)	10.90 ± 0.04	-1.42 ± 0.03	0.96 ± 0.15	—	—
Wright et al. (2017)	10.78 ± 0.21	-1.50 ± 0.16	0.63 ± 0.10	-0.62 ± 0.45	2.93 ± 0.40
Kelvin et al. (2014)	10.64 ± 0.07	-1.50 ± 0.22	0.74 ± 1.13	-0.43 ± 0.35	4.18 ± 1.52
Baldry et al. (2012)	10.66 ± 0.05	-1.47 ± 0.05	0.79 ± 0.23	-0.35 ± 0.18	3.96 ± 0.34
Peng et al. (2010)	10.67 ± 0.01	-1.56 ± 0.12	0.66 ± 0.09	-0.52 ± 0.04	4.03 ± 0.12

Columns: (1) Reference. (2) Characteristic stellar mass. (3,4) Low-mass-end slope and normalization of the low-mass component. (5,6) Same as Columns (3,4), but for the high-mass component. All the uncertainties are presented at 1σ. The parameters of the SMFs of Rodríguez-Puebla et al. (2020) refer to those of their modified Schechter function at the low-mass end (see their Section 3.2).

We find that $\alpha_\star$ becomes linearly flatter toward low redshifts, which is consistent with the trend found at $z < 3$ in the literature (e.g., Fontana et al. 2006; Mortlock et al. 2011). We fit a linear function to the data points, finding that the best-fit relation is

$$\alpha_\star = -0.075(z-3) - 1.6. \tag{2.19}$$

This best-fit relation is shown with the red thick line in the left bottom panel. We note that this fitting is a rough estimation just to illustrate the trend of the redshift evolution. Accurate determination is difficult particularly at $z > 6$ due to the discrepancies among the literature. For example, the $\alpha_\star$ values of Stefanon et al. (2021) and our work are comparable, while those of Bhatawdekar et al. (2019) fall below our estimation.

The large $|\alpha_\star|$ values (i.e., steep faint ends) at high redshifts indicate that the low-mass galaxies are the dominant population in the early universe. The flatter $\alpha_\star$ toward low redshifts reflect the hierarchical structure formation, where the low-mass galaxies undergo merging events and grow to be massive with cosmic time (e.g., Conselice et al. 2008; Mortlock et al. 2011). New formation of low-mass galaxies are suppressed at low redshifts due to stellar feedback; indeed, $\alpha_\star$ is flatter than the low-mass-end slopes of the HMFs (cyan line) especially at low redshifts. The low-mass-end slope discrepancy between the SMFs and HMFs is larger in lower redshifts, implying that the stellar feedback is more effective in the later epoch.

There are increasing trends of $M_\star^*$ at $3 < z < 10$ and $\phi_\star^*$ at $0 < z < 10$. We model $M_\star^*$ with a quadratic function truncated at $z = 3$ and $\phi_\star^*$ with a linear function, finding that the best-fit relations are roughly given as

$$\log(M_\star^*/M_\odot) = \begin{cases} 10.9 & \text{for } z < 3, \\ -0.03(z-3)^2 + 10.9 & \text{otherwise,} \end{cases} \tag{2.20}$$

and

$$\log(\phi_\star^*/[\mathrm{Mpc}^{-3}\ \mathrm{dex}^{-1}]) = -0.25(z-3) - 3.7, \tag{2.21}$$

respectively. Our results at $z \sim 0$ and $6-9$ roughly follow this relation. The increasing trends of $M_\star^*$ and $\phi_\star^*$ indicate that the galaxies become massive with cosmic time.

At $z < 3$, however, $M_\star^*$ ceases to increase at $M_\star^* \sim 10^{11}\ M_\odot$ and only $\phi_\star^*$ continues increasing. Due to these behaviors a knee emerges in an SMF; consequently, the SMF

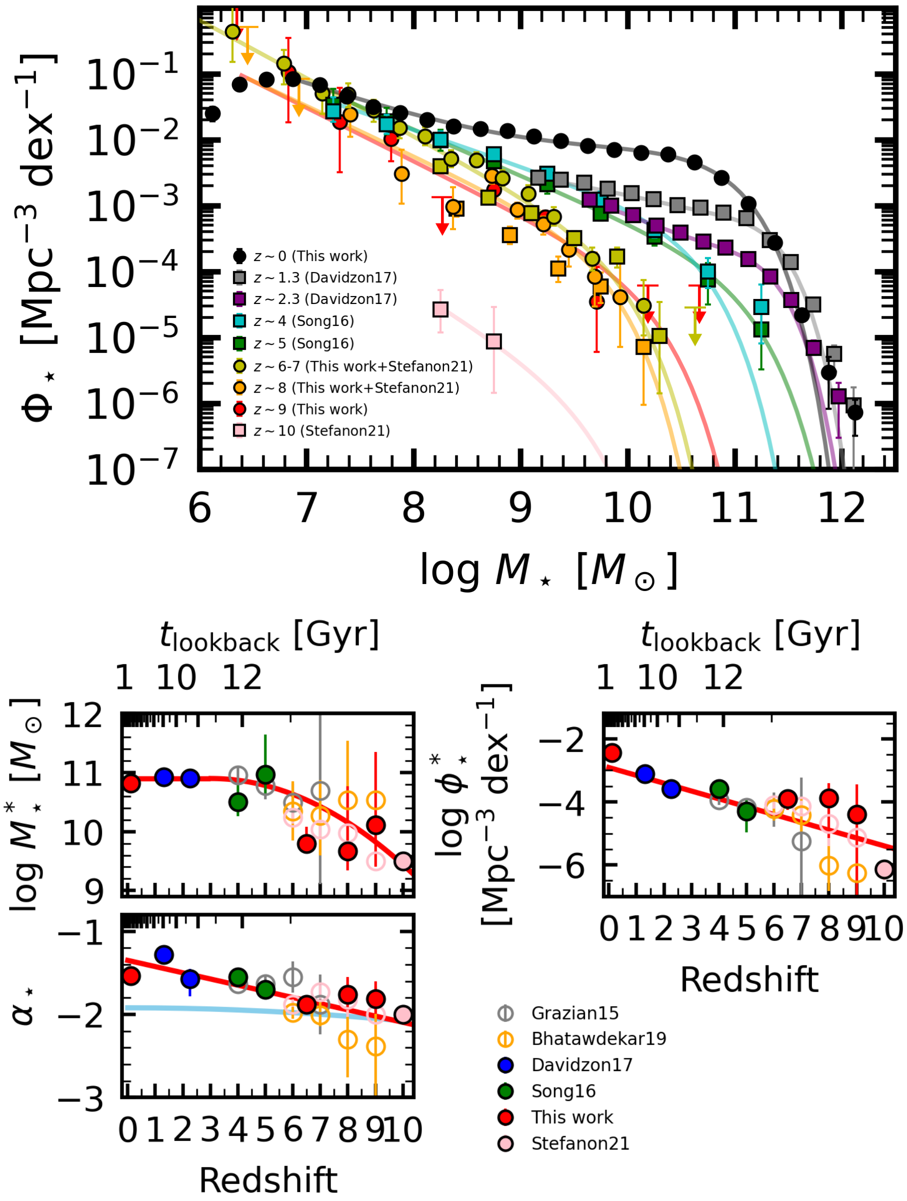

Figure 2.12 **Top:** SMFs at $z \sim 0-10$. The data are taken from this work ($z \sim 0$, $6-7$, 8, and 9), Davidzon et al. (2017, $z \sim 1.3$ and 2.3), Song et al. (2016, $z \sim 4$ and 5), and Stefanon et al. (2021, $z \sim 7$, 8, and 10). The lines are the best-fit double ($z < 3$) and single ($z > 3$) Schechter functions corresponding to the data points with the same colors. **Bottom:** Redshift evolution of the parameters of the Schechter functions. We add the data of Grazian et al. (2015) and Bhatawdekar et al. (2019). For $z < 3$, $\alpha_\star$ and $\phi_\star$ are of the low-mass components and the sum of low- and high-mass components, respectively, of the double Schechter functions. The red lines represent the best-fit models to illustrate the evolutionary trend. The cyan line shows the low-mass-end slope of the Sheth et al. (2001) HMF. The upper and lower horizontal axes represent the lookback time and redshift, respectively.

agrees better with a double Schechter function rather than with a single Schechter function at $z < 3$. These results are possibly attributed to the mass quenching effect caused by AGN feedback or major mergers (Peng et al. 2010; Ilbert et al. 2013; Muzzin et al. 2013). Mass quenching is likely to replace the dominant population from star-forming galaxies to quiescent galaxies. For example, Ilbert et al. (2013) report that the number fraction of quiescent to star-forming galaxies with $M_\star \sim 10^{11}\ M_\odot$ increases from ~ 30 % at $z = 2.5 - 3.5$ to ~ 80 % at $z = 0.2 - 0.5$ (see their Figure 6).

We quickly test whether our comparison of the SMFs at high and low redshifts is fair. First, we need to check the types of the sample. Our $z \sim 6 - 9$ dropouts are sorts of star-forming galaxies (see also Section 2.1.2). Although LBGs may be biased toward evolved and red systems, Stefanon et al. (2017) confirm that LBGs at $z \sim 4$ recover most of the sources selected with photometric redshifts. Given that the fraction of evolved systems is lower at $z > 6$, our selection is likely to be only marginal. At $z \sim 0$, although we do not recognize the galaxy types, our galaxies are also likely to be star-forming, given the fraction of the quiescent galaxies is quite low (< 20 %) particularly in the low-mass range ($< 10^{10}\ M_\odot$) as reported in Ilbert et al. (2013, see their Figure 6). We quickly confirm this by visual inspection.

Papovich et al. (2018) suggest that an SMF may be affected by whether galaxies reside in over- or under-dense regions, which indicates environmental effects in a over-dense region. Binggeli et al. (1987) also find that their optical LFs present different shapes between a field and the Virgo cluster. However, because our samples are mainly field galaxies both at $z > 6$ and ~ 0, this effect is unlikely to affect our results. Nonetheless, some of our galaxies reside in over-dense regions, which may slightly affect the massive ends of the SMFs (e.g., A2744z8OD at $z \sim 8$; Ishigaki et al. 2016).

CHAPTER 3
UV LUMINOSITY FUNCTIONS

In this Chapter, we summarize the UV LFs of galaxies at $z \sim 6-9$ (Section 3.1) and investigate that at $z \sim 0$ (Section 3.2) using the data of GALEX, respectively. The redshift evolution of the UV LFs is discussed in Section 3.3.

3.1 UV LFs at $z > 6$

As mentioned in Section 1.3.1, UV LFs at $z > 6$ are well constrained by the HFF program. HFF is advantageous owing to the combination of the very deep survey and strong lensing magnification by the foreground galaxy clusters. We particularly focus on the results of Ishigaki et al. (2018), who use the full data sets of HFF to reach the faintest magnitudes ever ($M_{\rm UV} \sim -14$ mag). Their UV LFs are shown in Figure 3.1. Because no $z \sim 10$ galaxies are identified in Ishigaki et al. (2018), only upper limits are available at $z \sim 10$. For comparisons, we show the UV LFs at $z \sim 7$, 8, and 9 obtained by HST blank field surveys (Oesch et al. 2018; Bouwens et al. 2021c). As shown in the Figure, the UV LFs of Ishigaki et al. (2018) agree well with these results in each redshift at $M_{\rm UV} \lesssim -17$ mag, and reach the fainter $M_{\rm UV}$ limits.

We also show the best-fit Schechter functions at $z \sim 6-7$, 8, and 9 obtained by Ishigaki et al. (2018). A Schechter function is given as

$$\begin{aligned} &\Phi_{\rm UV}(M_{\rm UV}){\rm d}M_{\rm UV} \\ &\quad = 0.4\ln(10)\phi^*_{\rm UV}10^{-0.4(\alpha_{\rm UV}+1)(M_{\rm UV}-M^*_{\rm UV})}\exp[-10^{-0.4(M_{\rm UV}-M^*_{\rm UV})}]{\rm d}M_{\rm UV}, \end{aligned} \tag{3.1}$$

where the characteristic absolute UV magnitude $M^*_{\rm UV}$, faint-end slope $\alpha_{\rm UV}$, and normalization $\phi^*_{\rm UV}$ are free parameters. Ishigaki et al. (2018) fit a Schechter function to their UV LFs and those taken from the blank field studies (Ouchi et al. 2009; Bradley et al. 2012; Oesch et al. 2013; Bowler et al. 2014; Bouwens et al. 2015; Calvi et al. 2016). They obtain that the best-fit values are $M^*_{\rm UV} = (-20.89^{+0.17}_{-0.13}, -20.35^{+0.20}_{-0.30})$ mag, $\alpha_{\rm UV} = (-2.15^{+0.08}_{-0.06}, -1.965^{+0.18}_{-0.15})$, and $\phi^*_{\rm UV} = (1.66^{+0.69}_{-0.49}, 2.51^{+1.036}_{-1.25}) \times 10^{-4}$ Mpc^{-3} mag^{-1} at $z \sim (6-7, 8)$. The best-fit value of $\phi^*_{\rm UV}$ at $z \sim 9$ is $1.32^{+0.27}_{-0.32} \times 10^{-4}$ Mpc^{-3} mag^{-1} while they fix $M^*_{\rm UV}$ and $\alpha_{\rm UV}$ values at $z \sim 9$ to those at $z \sim 8$. At $z \sim 10$, we show the best-fit Schechter function obtained by Oesch et al. (2018) instead of that

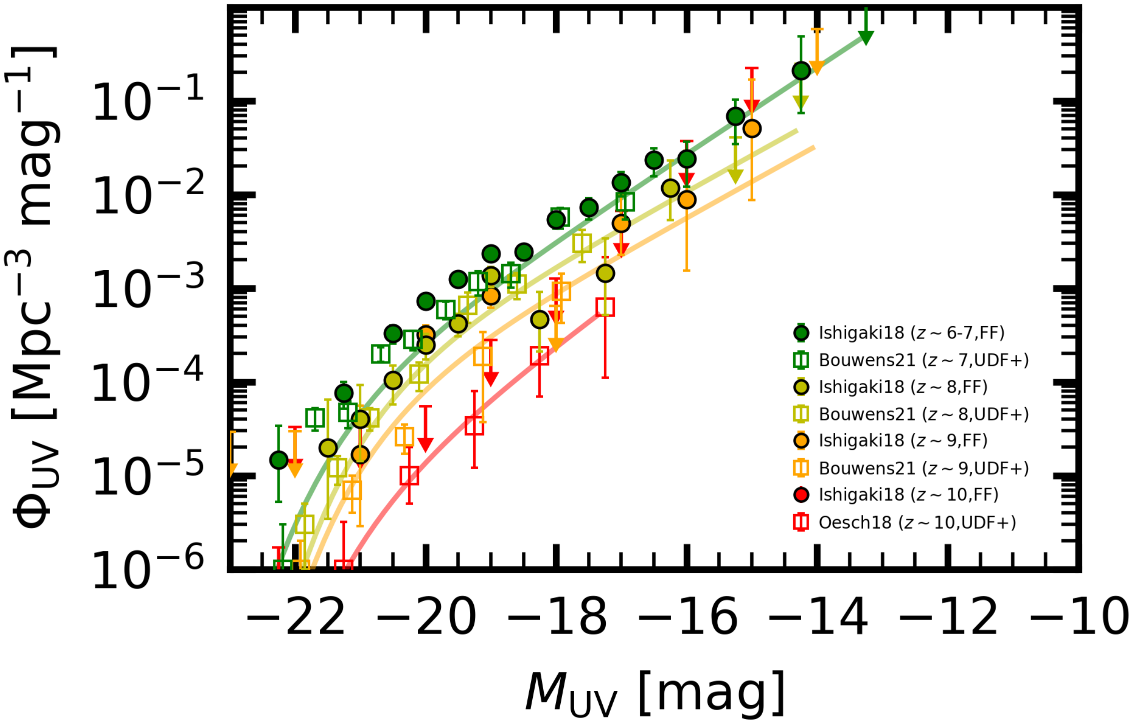

Figure 3.1 UV LFs at $z > 6$. The green, yellow, orange, and red symbols show the UV LFs at $z \sim 6-7$, 8, 9, and 10, respectively. The filled circles and lines represent the UV LFs and the best-fit Schechter functions of Ishigaki et al. (2018). The open boxes are taken from blank field surveys (Oesch et al. 2018; Bouwens et al. 2021c).

of Ishigaki et al. (2018). The best-fit parameters of the LF of Oesch et al. (2018) are -21.19 mag (fixed), $-2.38^{+0.28}_{-0.28}$, and $4.2^{+4.5}_{-2.2} \times 10^{-6}$ Mpc^{-3} mag^{-1}.

It is controversial whether the UV LFs have turnovers or not among literature (e.g., Bouwens et al. 2017b; Livermore et al. 2017; Atek et al. 2018; Yue et al. 2018). This is due to the insufficient observational depths and the large systematic uncertainties of magnification factors among different lensing models. We address this problem in Section 5.2.2 in detail.

3.2 UV LF at $z \sim 0$

3.2.1 Data

To derive the UV LF at $z \sim 0$, we utilize the latest (GR6/7) observational data of All-Sky Imaging Survey (AIS) of GALEX. We use the `GUVmatch` source catalog constructed by Bianchi & Shiao (2020), who eliminated duplicated sources from the GALEX original Merged catalog,[1] and cross-matched it with the SDSS DR14 spectroscopic source catalog. The magnitudes are measured as `MAG_AUTO` magnitudes with the `SExtractor` software (Bertin & Arnouts 1996).

To remove stars and spurious sources, we require the sources to meet the following criteria:

- The sources have counterparts in the SDSS spectroscopic catalog.
- The SDSS morphological flags (`type`) do not indicate `UNKNOWN`.
- The SDSS spectral type flags (`class`) do not indicate `STAR`.
- The spectroscopic redshift measurement is reliable ($\texttt{z} > \texttt{zErr} > 0$).

This selection leaves 644451 secure galaxies, including quasars, whose $M_{\rm UV}$-z distributions are shown with the small gray dots in Figure 3.2. We conservatively choose the galaxies that are brighter than the 5σ limiting magnitude $m_{5\sigma}$ of 19.9 mag (Morrissey et al. 2005, 2007; Bianchi et al. 2017; Bianchi & Shiao 2020) in UV and are in the ranges of $-20 \leq M_{\rm UV}$ and $0.003 \leq z \leq 0.2$. Our final sample consists of 67277 galaxies, which are shown with the black dots in Figure 3.2.

---

[1] `https://galex.stsci.edu/GR6/`

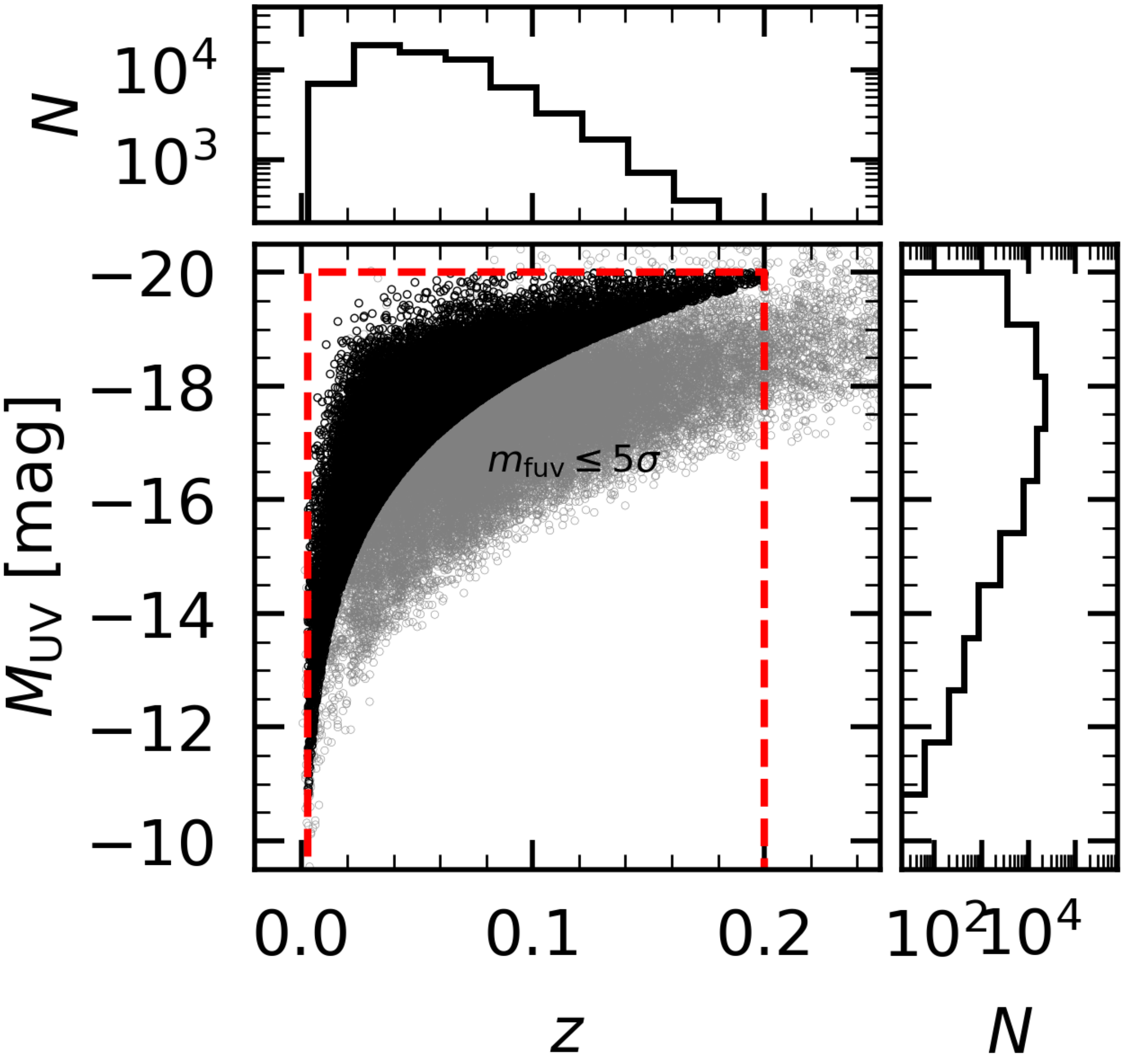

Figure 3.2 **Center:** $M_{\rm UV}$-z distributions. The black dots represent our final sample, which is selected from the secure galaxies (small gray dots). The final sample is defined as the secure galaxies meeting $0.003 \leq z \leq 0.2$, $M_{\rm UV} \geq -20$ mag, and $m_{\rm UV} \leq m_{5\sigma}$ (see text). **Top and Right:** z and $M_{\rm UV}$ histograms of the sample, respectively.

3.2.2 Methods

Completeness

We define the total completeness C_{tot} of the sample in the same manner as described in Section 2.2.2. First, for C_{det}, we assume that C_{det} follows the same function as that in Section 2.2.2, and shift it to $m_{5\sigma} = 19.9$ mag. Next, to estimate C_{specz}, we choose secure photometric sources from `GUVmatch` by removing the `UNKNOWN`-type sources. We define C_{specz} as the number fraction of our sample to the photometric sources. Lastly, C_{tot} is defined as $C_{\mathrm{tot}} = C_{\mathrm{det}} \times C_{\mathrm{specz}}$.

$1/V_{\mathrm{max}}$ Method

To derive a UV LF Φ_{UV}, we use the $1/V_{\mathrm{max}}$ method in the same manner as described in Section 2.2.2 in detail. A UV LF is estimated by

$$\Phi_{\mathrm{UV}}(M_{\mathrm{UV}}) = \frac{1}{\Delta M_{\mathrm{UV}}} \sum_{i=1}^{N} \frac{1}{V_{\mathrm{max},i}}, \tag{3.2}$$

where i runs over the galaxies in the magnitude bin centered at M_{UV} with the width ΔM_{UV}. Here

$$V_{\mathrm{max},i}(M_{\mathrm{UV},i}) = \Omega \int_{z_{\mathrm{l}}}^{z_{\mathrm{u}}} C_{\mathrm{tot}}(m_{\mathrm{UV}}(M_{\mathrm{UV},i}, z)) \frac{\mathrm{d}V}{\mathrm{d}z} \mathrm{d}z, \tag{3.3}$$

where $M_{\mathrm{UV},i}$ is the absolute UV magnitude of the i-th galaxy in the bin, C_{tot} is the total completeness obtained above, $\mathrm{d}V/\mathrm{d}z$ is the differential comoving volume (Equation 2.15). We adopt the integral range as $z_{\mathrm{l}} = 0.003$ and $z_{\mathrm{u}} = 0.2$. We use the `AREAcat` tool (Bianchi et al. 2019) to calculate the area Ω occupied by the galaxies, obtaining that $\Omega = 1.11 \times 10^4$ deg^2 (see also Bianchi & Shiao 2020). The Poisson errors are adopted as the uncertainties of Φ_{UV}.

3.2.3 Results

The result is shown with the red circles in Figure 3.3. We compare our result with those at $z \sim 0$ taken from the previous studies of GALEX (old data releases; $0.07 < z < 0.13$, Budavári et al. 2005 and $z < 0.1$, Wyder et al. 2005), the VIMOS-VLT

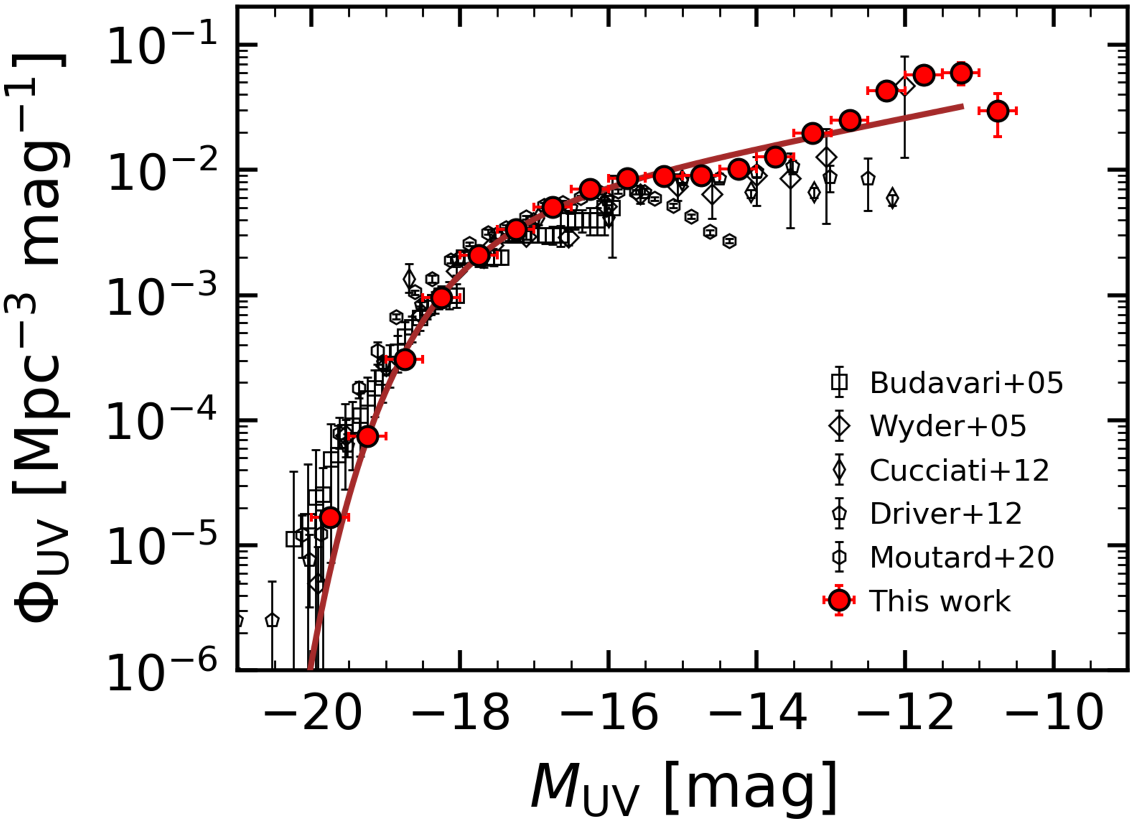

Figure 3.3 UV LFs at $z = 0$. Our UV LF is shown with the red circles, while the open black symbols refer to those obtain in the literature (Budavári et al. 2005; Wyder et al. 2005; Cucciati et al. 2012; Driver et al. 2012; Moutard et al. 2020). The UV LF of Budavári et al. (2005) is of $z = 0.07 - 0.13$. The brown line represents our best-fit Schechter function.

Deep Survey (VVDS, $0.05 < z < 0.2$; Cucciati et al. 2012), the GAMA survey ($0.013 < z < 0.1$; Driver et al. 2012), and the recent CFHT Large Area U-band Deep Survey (CLAUDS) and HSC-SSP ($0.05 < z < 0.3$; Moutard et al. 2020).

Our result is in good agreement with those of the literature in the bright and intermediate $M_{\rm UV}$ range ($M_{\rm UV} < -14$). At $-14 < M_{\rm UV} < -11$, our UV LF shows a hump. This is in line with the UV LF of Wyder et al. (2005), while those of Cucciati et al. (2012) and Driver et al. (2012) underlie our results. Although the physical origin of the hump is unclear, one possibility is the contribution of dwarf irregular and elliptical galaxies. For example, Binggeli et al. (1987) found that the faint end of their B-band LF is dominated by dwarf irregular galaxies, which results in a hump. Driver et al. (2012) obtained UV LFs of spiral and elliptical galaxies, suggesting that the contribution of the elliptical galaxies become larger toward the faint end. We confirm that many of our galaxies with $M_{\rm UV} > -12$ mag are indeed dwarf irregular, according to the visual classification by Ann et al. (2015).

At the faintest end ($M_{\rm UV} \sim -11$ mag), a tentative turnover (downturn) is identified. We reach down below -12 mag for the first time, owing to the much larger number of our galaxies than those in the literature ($N = 105$ at $M_{\rm UV} > -11$ mag). We discuss the hump and turnover in detail in Section 5.2.2.

We fit a Schechter function (Equation 3.1) to our UV LF data points brighter than the turnover ($M_{\rm UV} < -11$ mag). The brown line in Figure 3.3 shows the best-fit Schechter function. The confidence intervals of the parameters are presented in Figure 3.4 and Table 3.1. We find that our estimation roughly agrees with those of the literature, given the large systematic differences among the literature. Our UV LF, together with those from the literature, presents very shallow faint-end slopes of $\alpha_{\rm UV} \sim (-1.5) - (-0.9)$. This may reflect stellar feedback, similarly as we discussed for the low-mass-end slopes of the SMFs (Section 2.3). We note that the best-fit values of the parameters are hardly affected by whether including or excluding the data points around the hump in fitting.

3.3 Redshift Evolution of UV LFs

We investigate the redshift evolution of the UV LFs over $z \sim 0 - 10$ in Figure 3.5. The UV LFs at $z \sim 6 - 9$ and 0 are taken from Ishigaki et al. (2018, Section 3.1)

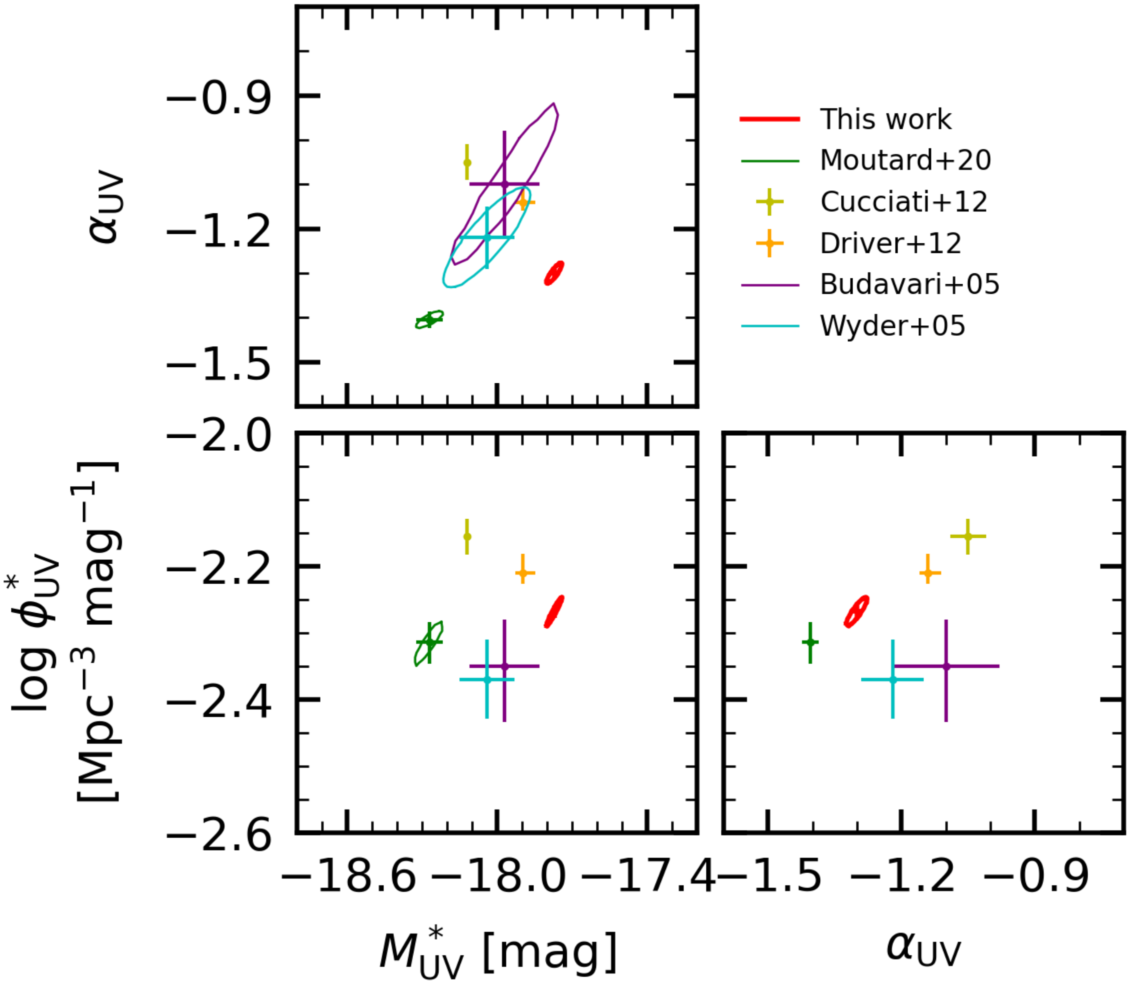

Figure 3.4 Confidence intervals of the parameters of the $z \sim 0$ Schechter functions shown in Figure 3.3. The red contours and crosses show our 3σ confidence intervals, while the other lines denote the 1σ contours and confidence intervals obtained in the literature.

Table 3.1 Best-fit parameters of the $z \sim 0$ Schechter functions.

Reference	$M^*_{\rm UV}$ [mag]	$\alpha_{\rm UV}$	$\phi^*_{\rm UV}$ [10^{-3} Mpc^{-3} mag^{-1}]
This work	-17.77 ± 0.01	-1.30 ± 0.01	5.80 ± 0.12
Moutard et al. (2020)	-18.27 ± 0.05	-1.41 ± 0.02	4.85 ± 0.35
Cucciati et al. (2012)	-18.12 ± 0.00	-1.05 ± 0.04	7.00 ± 0.44
Driver et al. (2012)	$-17.89^{+0.05}_{-0.03}$	$-1.14^{+0.03}_{-0.02}$	$6.17^{+0.41}_{-0.24}$
Budavári et al. (2005)	-17.97 ± 0.14	-1.10 ± 0.12	4.47 ± 0.78
Budavári et al. (2005)	-18.07 ± 0.17	-1.09 ± 0.23	4.68 ± 0.82
Budavári et al. (2005)	-18.15 ± 0.17	-1.03 ± 0.34	4.47 ± 0.66
Wyder et al. (2005)	-18.04 ± 0.11	-1.22 ± 0.07	$4.27^{+0.63}_{-0.55}$

and this work (Section 3.2). We add the UV LFs at intermediate redshifts from the literature: Moutard et al. (2020) and Alavi et al. (2016) at $z \sim 1$, Parsa et al. (2016) at $z \sim 2$ and 3, Bouwens et al. (2021c) at $z \sim 4$, 5, and 6, and Oesch et al. (2018) at $z \sim 10$. The results are shown in the top panel, together with the best-fit Schechter functions. The corresponding parameters of these Schechter functions are displayed in the bottom panels.

We find that $\alpha_{\rm UV}$ becomes linearly flatter toward low redshifts, as has been found in many previous studies (e.g., Alavi et al. 2016; Parsa et al. 2016; Song et al. 2016; Moutard et al. 2020; Bouwens et al. 2015, 2021c). We fit a linear function to $\alpha_{\rm UV}$, finding that the best-fit relation is

$$\alpha_{\rm UV} = -0.11(z-3) - 1.6 \qquad \text{for } 0 < z < 10. \tag{3.4}$$

The steep and flat $\alpha_{\rm UV}$ at high and low redshifts, respectively, support the picture that low-mass galaxies are dominant in the early universe and become gradually massive through merging events, similarly as suggested by the SMFs (Section 2.3). Again, the fitting here is a rough estimation for an illustrative purpose.

The formation of massive galaxies corresponds to an increasing trend of $\phi^*_{\rm UV}$ with redshift at $z > 3$. Meanwhile, $M^*_{\rm UV}$ shows only a slight redshift evolution at $z > 3$. This is probably because the physical mechanisms leading to the exponential cutoff at the bright end do not depend on the redshift. Such mechanisms may include AGN feedback (e.g., Croton et al. 2006) and strong dust attenuation (e.g., Bouwens et al. 2009; Reddy et al. 2010). Assuming that $\phi^*_{\rm UV}$ follows a quadratic function truncated at $z = 3$ and that $M^*_{\rm UV}$ is constant, we find that the best-fit relations are

$$\left.\begin{aligned} \log(\phi^*_{\rm UV}/[\mathrm{Mpc^{-3}\ mag^{-1}}]) &= -0.053(z-3)^2 - 2.5, \\ M^*_{\rm UV} &= -20.8. \end{aligned}\right. \qquad \text{for } z > 3. \tag{3.5}$$

At $z < 3$, $\phi^*_{\rm UV}$ becomes constant, and $M^*_{\rm UV}$ alternatively starts to increase rapidly. These trends may be related to the emergence of quiescent galaxies as mentioned in Section 2.3. We assume that $M^*_{\rm UV}$ follows a quadratic function and a constant $\phi^*_{\rm UV}$, obtaining that the best-fit models are

$$\left.\begin{aligned}\log(\phi^*_{\mathrm{UV}}/[\mathrm{Mpc}^{-3}\ \mathrm{mag}^{-1}]) &= -2.5,\\ M^*_{\mathrm{UV}} &= 0.35(z-3)^2 - 20.8.\end{aligned}\right. \quad \text{for } z < 3. \tag{3.6}$$

These models are similar to those assumed in Bouwens et al. (2021c). We confirm that our best-fit values are comparable to their estimation.

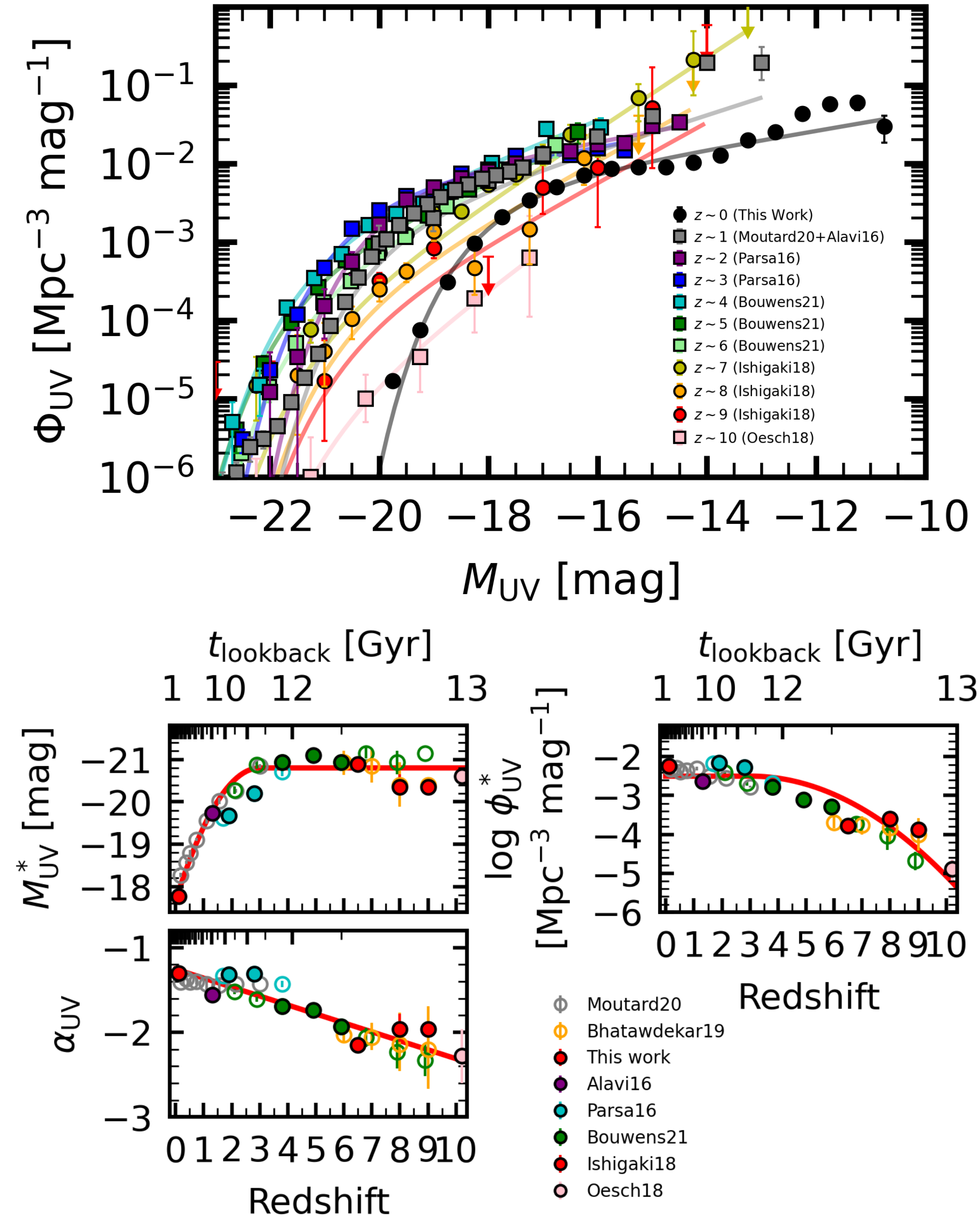

Figure 3.5 **Top:** UV LFs at $z \sim 0-10$. The data are taken from this work ($z \sim 0$), Moutard et al. (2020, $0.9 < z < 1.3$), Alavi et al. (2016, $1 < z < 1.6$), Parsa et al. (2016, $z \sim 2$ and 3), Bouwens et al. (2021c, $z \sim 4$, 5, and 6), Ishigaki et al. (2018, $z \sim 6-7$, 8, and 9), and Oesch et al. (2018, $z \sim 10$). The lines show the best-fit Schechter functions corresponding to the data points with the same colors. **Bottom:** Redshift evolution of the parameters of the Schechter functions. We add the data of Bhatawdekar et al. (2019) at $z \sim 6-9$. The red lines represent the best-fit models to illustrate the evolutionary trend (Equations 3.4, 3.5, and 3.6).

CHAPTER 4
EXTENDED LYα EMISSION

In this Chapter, we investigate Lyα emission around LAEs at $z \sim 2-7$ using the data of Subaru/HSC-SSP and CHORUS projects.

4.1 Data

4.1.1 Images

We use NB and broad-band (BB) imaging data that were obtained in two Subaru/HSC intensive surveys, HSC-SSP and CHORUS. The HSC-SSP and CHORUS data were obtained in March 2014-January 2018 and January 2017-December 2018, respectively. We specifically use the internal data of the S18A release. The HSC-SSP survey is a combination of three layers: Wide, Deep, and UltraDeep (UD). We use the UD layer images in the fields of the Cosmological Evolution Survey (UD-COSMOS; Scoville et al. 2007) and Subaru/XMM Deep Survey (UD-SXDS; Sekiguchi et al. 2005), because the wide survey areas (~ 2 deg^2 for each field) and deep imaging (the 5σ limiting magnitudes are ~ 26 mag in a $2''$-diameter aperture) in these fields are advantageous for the detection of very diffuse Lyα emission. The CHORUS data were obtained over the UD-COSMOS field. The HSC-SSP and CHORUS data were reduced with the HSC pipeline v6.7 (Bosch et al. 2018).

The HSC-SSP program of S18A provides the data of two NB (NB816 and NB921) filters in the UD-COSMOS and UD-SXDS fields, while the CHORUS images are offered in four NB (NB387, NB527, NB718, and NB973) filters in the UD-COSMOS field. In this work, we present the results in the NB387, NB527, NB816, and NB921 filters. The NB718 and NB973 filters are not used in the following sections, because the number of LAEs and the image depths are not sufficient to detect diffuse Lyα emission. The NB387, NB527, NB816, and NB921 filters are centered at 3863, 5260, 8177, and 9215 Å with the FWHMs of 55, 79, 113, and 135 Å, respectively, which cover the observed wavelengths of Lyα emission from $z = 2.178 \pm 0.023$, 3.327 ± 0.032, 5.726 ± 0.046, and 6.580 ± 0.056, respectively. Five BB (g-, $r2$-, $i2$-, z-, and y-band) filters are also available in both HSC-SSP and CHORUS. Figure 4.1 shows the NB and BB filter throughputs, and Table 4.1 summarizes the images and filters.

Bright sources in the NB and BB images must be masked since they contaminate diffuse emission. We thus mask pixels flagged with either `DETECT` or `BRIGHT_OBJECT` using the masks provided by the HSC pipeline (termed *original* masks). A pixel is flagged with `DETECT` or `BRIGHT_OBJECT` when the pixel is covered by a detected ($\geq 5\sigma$) object or is affected by nearby bright sources, respectively. However, because part of bright sources are missed in the *original* masks due to bad photometry, the HSC-SSP team offered new masks that mitigated this problem (hereafter termed *revised* masks).[1] We adopt the *revised* masks in addition to the *original* masks to flag `BRIGHT_OBJECT`. We use the *revised* g-, $r2$-, z-, and y-band masks for NB387, NB527, NB816, and NB921 images, respectively, because the *revised* masks are offered only in the BB filters. For the BB images, we use the *revised* masks defined for each BB filter. We visually confirm that these criteria successfully cover bright sources and contaminants in the images.

4.1.2 LAE Sample

We use the LAE catalog constructed by Ono et al. (2021) as a part of the Systematic Identification of LAEs for Visible Exploration and Reionization Research Using Subaru HSC (SILVERRUSH) project (Ouchi et al. 2018, see also Shibuya et al. 2018a,b; Konno et al. 2018; Harikane et al. 2018b; Inoue et al. 2018; Higuchi et al. 2019; Harikane et al. 2019; Goto et al. 2021; Kakuma et al. 2021). Ono et al. (2021) selected LAE candidates based on color and removed contaminants by a convolutional neural network (CNN) and visual inspection. Their final catalog includes (542, 959, 395, 150) LAEs at z = (2.2, 3.3, 5.7, 6.6) in the UD-COSMOS field, and (560, 75) LAEs at z = (5.7, 6.6) in the UD-SXDS field.

The NB images of the UD-COSMOS and UD-SXDS fields are deepest at the center and become shallower toward the edges (Hayashi et al. 2020; Inoue et al. 2020). We thus exclude LAEs outside of the boundaries that are shown with the black dashed circles shown in Figure 4.2.

---

[1] `https://hsc-release.mtk.nao.ac.jp/doc/index.php/bright-star-masks-2/`

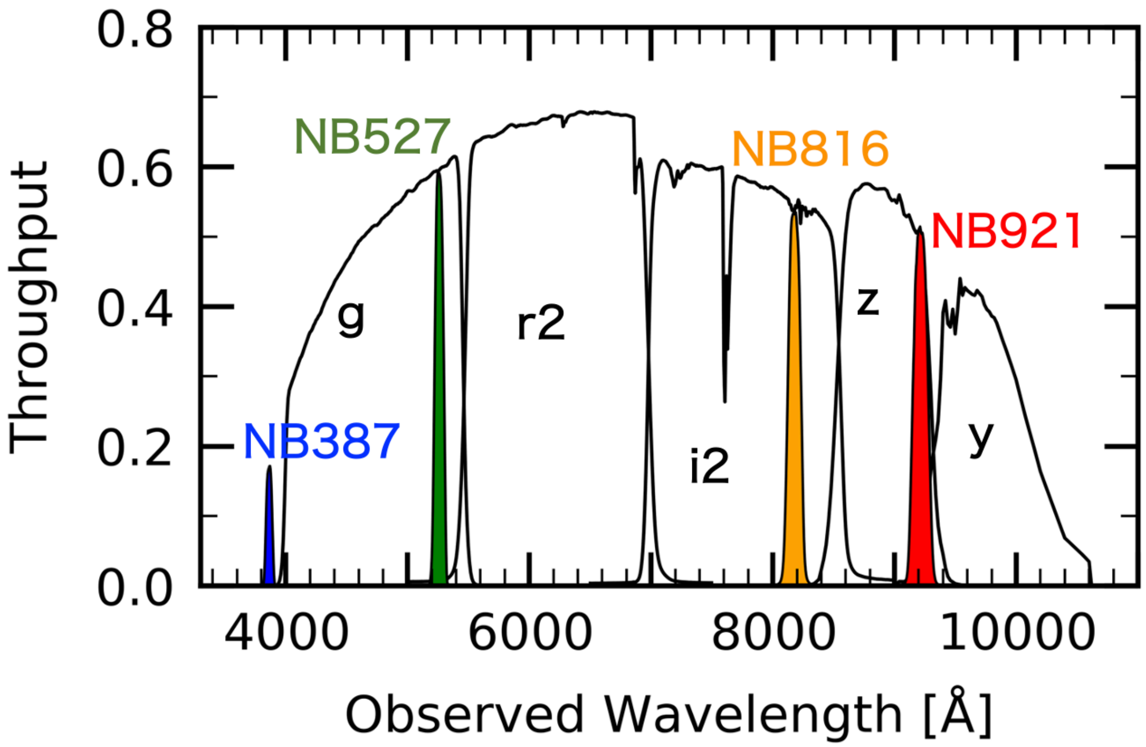

Figure 4.1 Effective response curves of the HSC NB filters: NB387 (blue), NB527 (green), NB816 (orange), and NB921 (red), and BB filters: g, $r2$, $i2$, z, and y (black). These response curves include the quantum efficiency of the HSC CCD, the transmittance of the dewar window and the Primary Focus Unit, the reflectivity of the Primary Mirror, and the airmass at the Telescope site.

Table 4.1 Summary of the NB filters and images.

				UD-COSMOS		UD-SXDS	
NB	λ_c [Å]	FWHM [Å]	$z_{\rm LAE}$	Area [deg^2]	$m_{\rm NB,5\sigma}$ [mag]	Area [deg^2]	$m_{\rm NB,5\sigma}$ [mag]
(1)	(2)	(3)	(4)	(5)	(6)	(7)	(8)
NB387 (CHORUS)	3863	55	2.178 ± 0.023	1.561	25.67	—	—
NB527 (CHORUS)	5260	79	3.327 ± 0.032	1.613	26.39	—	—
NB816 (HSC-SSP)	8177	113	5.726 ± 0.046	2.261	25.75	2.278	25.61
NB921 (HSC-SSP)	9215	135	6.580 ± 0.056	2.278	25.48	2.278	25.31

Columns: (1) NB filter. (2)-(3) Central wavelength (λ_c) and FWHM of the NB filter transmission curve. (4) Redshift range of the LAEs whose Lyα emission enters the NB filter. (5)-(6) Effective area and 5σ limiting NB magnitude ($m_{\rm NB,5\sigma}$) in the UD-COSMOS field. The $m_{\rm NB,5\sigma}$ value is measured with a $2''$-diameter aperture in each patch, and then averaged over the field. See Inoue et al. (2020) and Hayashi et al. (2020) for the spatial variance of $m_{\rm NB,5\sigma}$. The $m_{\rm NB,5\sigma}$ value in NB387 is corrected for the systematic zero-point offset by 0.45 mag (see Section 4.1.2). (7)-(8) Same as Columns (5)-(6), but for the UD-SXDS field. The values in this Table are cited from Ono et al. (2021).

We estimate the Lyα line luminosities ($L_{\mathrm{Ly}\alpha}$) following Shibuya et al. (2018a, see also Itoh et al. 2018). First, we measure the NB (BB) magnitudes m_{NB} (m_{BB}) of the LAEs at $z = 2.2$, 3.3, 5.7, an 6.6 in the NB387 (g-band), NB527 ($r2$-band), NB816 (z-band), and NB921 (y-band) filters, respectively. The magnitudes are measured with a $2''$-diameter aperture because it efficiently covers the PSF, whose FWHM is $0.''8 - 1.''1$ (Ono et al. 2021). The NB387 magnitudes are corrected for the systematic zero-point offset by 0.45 mag, following the recommendation by the HSC-SSP team.[2] Next, we follow Shibuya et al. (2018a) to derive the Lyα line fluxes ($f_{\mathrm{Ly}\alpha}$) from m_{NB} and m_{BB}, adopting the IGM attenuation model from Inoue et al. (2014). Lastly, the values of $L_{\mathrm{Ly}\alpha}$ are derived via $L_{\mathrm{Ly}\alpha} = 4\pi d_{\mathrm{L}}(z_{\mathrm{LAE}})^2 f_{\mathrm{Ly}\alpha}$, where $d_{\mathrm{L}}(z_{\mathrm{LAE}})$ denotes the luminosity distance to the LAE at redshift z_{LAE}.

Although the completeness of the LAEs is as high as $\gtrsim 90$ % at $m_{\mathrm{NB}} \lesssim 24.5$ in the CNN of Ono et al. (2021), faint LAEs may be missed in the observations and selection. To ensure completeness, we use only LAEs whose $L_{\mathrm{Ly}\alpha}$ values are larger than the modes (peaks) of the $L_{\mathrm{Ly}\alpha}$ histograms, which are represented as $L_{\mathrm{Ly}\alpha}^{\mathrm{min}}$ in Table 4.2. This sample, termed the *all* sample, consists of (289, 762, 210, 56) LAEs at $z = (2.2, 3.3, 5.7, 6.6)$ and (393, 24) LAEs at $z = (5.7, 6.6)$ in the UD-COSMOS and UD-SXDS fields, respectively. To accurately compare the LAEs of different redshifts at similar $L_{\mathrm{Ly}\alpha}$ values, we further exclude faint LAEs from the *all* sample such that the mean $L_{\mathrm{Ly}\alpha}$ values are equal to $10^{42.9}$ erg s^{-1} at each redshift. This selection results in (37, 123, 125) LAEs at $z = (2.2, 3.3, 5.7)$ and 313 LAEs at $z = 5.7$ in the UD-COSMOS and UD-SXDS fields, respectively, which we hereafter refer to as the *bright* subsample. At $z = 6.6$, since the mean $L_{\mathrm{Ly}\alpha}$ values of the *all* sample are $10^{43.0}$ erg s^{-1} in both the UD-COSMOS and UD-SXDS fields, we also use the *all* sample as the *bright* subsample. In summary, we use a total of 1781 and 717 LAEs in the UD-COSMOS+UD-SXDS fields as the *all* sample and the *bright* subsample, respectively. The $L_{\mathrm{Ly}\alpha}$ values and sample sizes are summarized in Table 4.2. The sky distributions of the LAEs in the UD-COSMOS and UD-SXDS fields are presented in Figures 4.2.

As mentioned in Section 1.4.3, Kakuma et al. (2021) recently investigated extended Lyα emission using HSC data. Our major update compared to Kakuma et al. (2021) is that we add new 1051 LAEs at $z = 2.2$ and 3.3 using the CHORUS data. The catalog

---

[2] `https://hsc-release.mtk.nao.ac.jp/doc/index.php/known-problems-2/#hsc-link-10`

of $z = 5.7$ and 6.6 LAEs are also updated in that we use the latest catalog constructed by Ono et al. (2021) based on HSC-SSP S18A images, while Kakuma et al. (2021) used the S16A catalog taken from Shibuya et al. (2018a). Although the number of the LAEs increased owing to the improved limiting magnitudes, we excluded faint LAEs from those included in Ono et al. (2021), which results in comparable numbers of the LAEs. The sky and $L_{\mathrm{Ly}\alpha}$ distributions are also similar. We use the same images as Kakuma et al. (2021, i.e., those taken from the HSC-SSP S18A release) in NB816 and NB921, while our masking prescription may be different from theirs.

4.2 Methods

4.2.1 Intensity Mapping

We perform the intensity mapping technique to estimate Lyα emission around the LAEs. As schematically shown in Figure 4.3 for example, the Lyα intensity traced with an NB921 image and the positions of LAEs at $z = 6.6$ should be correlated (this also holds for the other NB image-LAE pairs). Meanwhile, the positions of foreground objects should not be correlated with the Lyα intensity because they are at different redshifts. Therefore, we can measure the Lyα emission signals around the LAEs by subtracting those around the foreground objects. This is the basic idea of the intensity mapping technique. This technique is robust against contamination from foreground objects.

We compute SB as a cross-correlation function between given band (XB) emission intensities and given objects (OBJs), $\mathrm{SB}_{\mathrm{XB}\times\mathrm{OBJ}}$,[3] via

$$\mathrm{SB}_{\mathrm{XB}\times\mathrm{OBJ},\nu}(r) = \frac{1}{N_{r,\mathrm{OBJ}}} \sum_{i=1}^{N_{r,\mathrm{OBJ}}} \mu_{\nu,i}^{(\mathrm{XB})} \tag{4.1}$$

---

[3] The right-hand side of Equation 4.1 represents a cross-correlation function, which has usually been referred to as ξ in previous work (e.g. Croft et al. 2016, 2018; Bielby et al. 2017; Momose et al. 2021a,b). However, we refer to this function as “SB,” since the cross-correlation function is equivalent to surface brightness in our analyses.

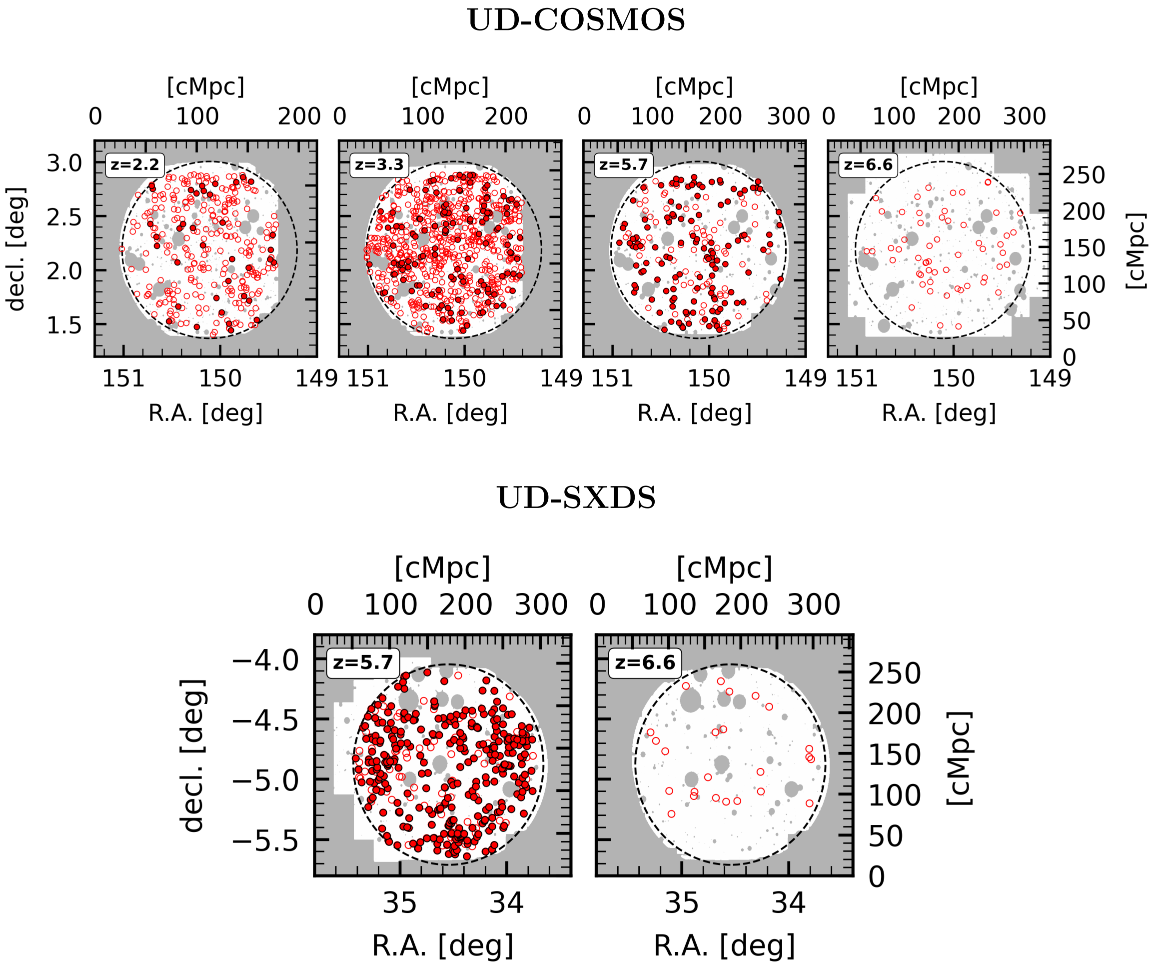

Figure 4.2 **Top:** Sky distributions of the LAEs in the UD-COSMOS field at $z = 2.2$, 3.3, 5.7, and 6.6, from left to right. The open red circles show the positions of the LAEs included in the *all* sample but not in the *bright* subsample, while the filled red circles indicate those of the *bright* subsample LAEs (i.e., *all* sample LAEs are represented by the open+filled red circles). We use the LAEs inside the black dashed circles. The background white shaded area shows the NB387, NB527, NB816, and NB921 images, from left to right. The gray shaded area shows the regions where the pixel is masked or the UD image is not offered. Note that the distribution of the *bright* subsample at $z = 6.6$ is not displayed, because we treat the *all* sample also as the *bright* subsample at $z = 6.6$. **Bottom:** Same as the top panels, but for the UD-SXDS field at $z = 5.7$ (left) and 6.6 (right).

Table 4.2 Summary of the sample.

	UD-COSMOS			UD-SXDS		
$z_{\rm LAE}$ (1)	$\log L_{\rm Ly\alpha}^{\rm min}$ [erg s^{-1}] (2)	$\log L_{\rm Ly\alpha}^{\rm mean}$ [erg s^{-1}] (3)	$N_{\rm LAE}$ (4)	$\log L_{\rm Ly\alpha}^{\rm min}$ [erg s^{-1}] (5)	$\log L_{\rm Ly\alpha}^{\rm mean}$ [erg s^{-1}] (6)	$N_{\rm LAE}$ (7)
all sample						
2.2	42.2	42.5	289	—	—	—
3.3	42.1	42.5	762	—	—	—
5.7	42.6	42.8	210	42.5	42.8	393
6.6	42.8	43.0	56	42.9	43.0	24
Total			1317			464
bright subsample						
2.2	42.6	42.9	37	—	—	—
3.3	42.6	42.9	123	—	—	—
5.7	42.7	42.9	125	42.6	42.9	313
6.6	42.8*	43.0*	56*	42.9*	43.0*	24*
Total			341			376

Columns: (1) Redshift. (2)-(3) Minimum and mean Lyα luminosities of the *all* sample LAEs measured with a $2''$-diameter aperture in the UD-COSMOS field. (4) Number of the LAEs. The total number of the LAEs over $z = 2.2 - 6.6$ is shown in the bottom row. (5)-(7) Same as Columns (2)-(4), but for the UD-SXDS field.

$*$ At $z = 6.6$, we treat the *all* sample also as the *bright* subsample in each field (see text).

and

$$\mathrm{SB}_{\mathrm{XB}\times\mathrm{OBJ}}(r) = \mathrm{SB}_{\mathrm{XB}\times\mathrm{OBJ},\nu}(r) \times \mathrm{FWHM}_{\mathrm{XB}}. \tag{4.2}$$

The pixel of the i-th pixel-OBJ pair has a pixel value of $\mu_{\nu,i}^{(\mathrm{XB})}$ in the XB image in units of erg s^{-1} cm^{-2} Hz^{-1} arcsec^{-2}. In NB387, we multiply $\mu_{\nu,i}^{(\mathrm{NB387})}$ by 1.5 to correct for the zero-point offset of 0.45 mag (see Section 4.1.2). The summation runs over the $N_{r,\mathrm{OBJ}}$ pixel-OBJ pairs that are separated by a spatial distance r. We use pixels at distances of between $1\overset{\prime\prime}{.}5$ and $40''$ from each OBJ (corresponding to the outer part of the CGM and outside), which were then divided into six radial bins. $\mathrm{FWHM}_{\mathrm{XB}}$ represents the XB filter width (in units of Hz) corrected for IGM attenuation, derived via

$$\mathrm{FWHM}_{\mathrm{XB}} = \frac{\int_0^\infty e^{-\tau_{\mathrm{eff}}(\nu)} T_{\mathrm{XB}}(\nu) \mathrm{d}\nu/\nu}{T_{\mathrm{XB}}(\nu_\alpha)/\nu_\alpha}, \tag{4.3}$$

where $T_{\mathrm{XB}}(\nu)$ denotes the transmittance of the XB filter, and ν_α is the observed Lyα line frequency. We adopt the IGM optical depth $\tau_{\mathrm{eff}}(\nu)$ from Inoue et al. (2014).

The statistical uncertainty of $\mathrm{SB}_{\mathrm{XB}\times\mathrm{OBJ}}$ is estimated by the bootstrap method. We randomly resample OBJ while keeping the sample size and calculated $\mathrm{SB}_{\mathrm{XB}\times\mathrm{OBJ}}$. We then repeat the resampling 10^4 times, adopting the 1σ standard deviation of the $\mathrm{SB}_{\mathrm{XB}\times\mathrm{OBJ}}$ values as the 1σ statistical uncertainty of the original $\mathrm{SB}_{\mathrm{XB}\times\mathrm{OBJ}}$.

4.2.2 NonLAE Sample

Although the intensity mapping technique can remove spurious signals from low-redshift interlopers, other systematics, such as the sky background and PSF, may still contaminate LAE signals. To estimate the contribution from these systematics, we use foreground sources, which we hereafter term "NonLAEs." Because NonLAEs should correlate only with the systematics, but not with Lyα emission from LAEs, we can estimate these systematics by applying the intensity mapping technique to NonLAEs.

We construct NonLAE samples as follows. First, we detect sources in the NB images using `SExtractor` (Bertin & Arnouts 1996). Second, we select only sources that are sufficiently bright ($\lesssim 26$ mag) in the g, $r2$, and $i2$ bands, to remove spurious sources and artifacts. Third, we randomly select the sources such that they have the same sky, NB FWHM ($\mathrm{FWHM}_{\mathrm{NB}}$), and m_{NB} distributions as those of the LAEs

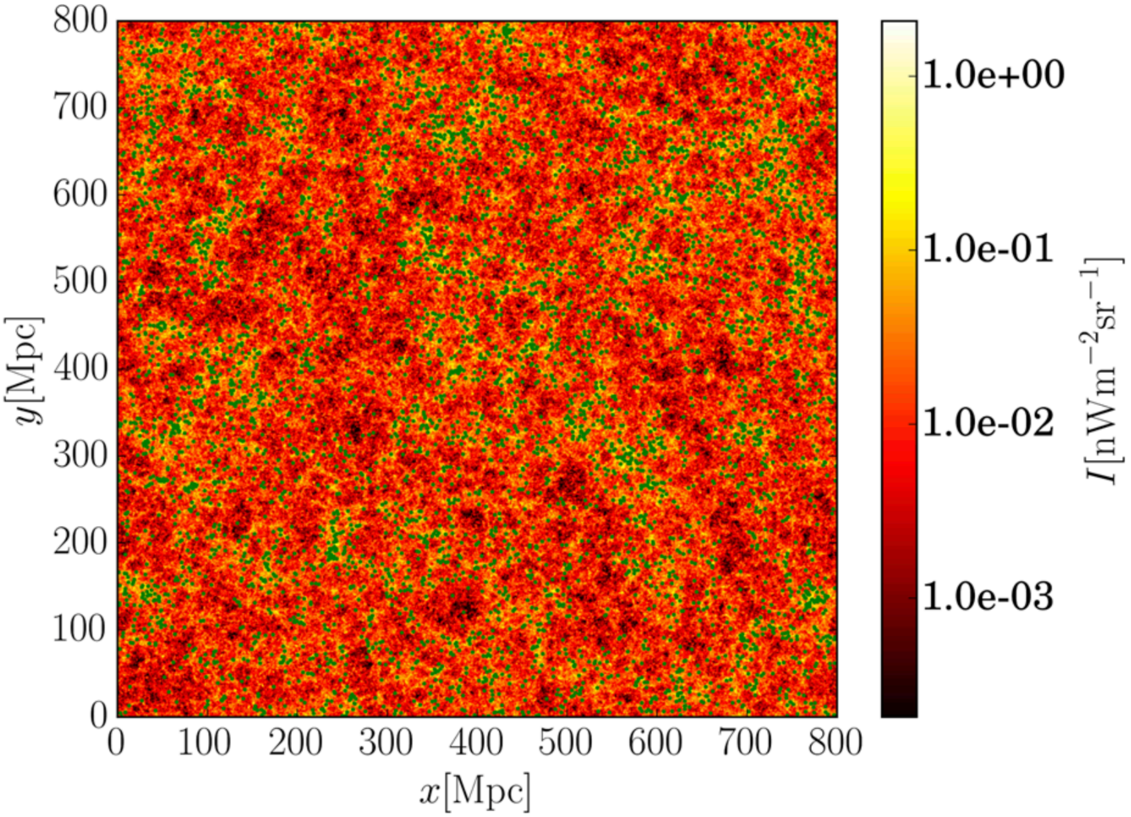

Figure 4.3 Schematic view of the basic idea of the intensity mapping technique. The colors represent the intensity of Lyα emission from $z = 6.6$ measured with an NB image. The overlaid green dots show the positions of LAEs at $z = 6.6$. One can see that the yellow colors (Lyα emission) and the green dots (LAE positions) are correlated. Adopted from the semi-numerical simulation of Comaschi & Ferrara (2016a).

in each field at each redshift. In this way, $\sim 10^3$ sources are selected, which we define as NonLAEs. Figure 4.4 shows the FWHM$_{\rm NB}$-$m_{\rm NB}$ distributions of the $z = 3.3$ LAEs and corresponding NonLAEs, as an example. We note that only < 1 % of the NonLAEs meet the color selection criteria of LAEs defined by Ono et al. (2021, see their Section 2).

4.3 Results

4.3.1 NB Surface Brightness

We estimate the SB of Lyα emission (SB$_{{\rm Ly}\alpha}$) around the LAEs as follows. First, we subtract the systematics (SB$_{\rm NB\times NonLAE}$) from the emission from the LAEs (SB$_{\rm NB\times LAE}$) via

$$\mathrm{SB}_{\rm NB} = \mathrm{SB}_{\rm NB\times LAE} - \mathrm{SB}_{\rm NB\times NonLAE}. \tag{4.4}$$

Uncertainties in SB$_{\rm NB}$ propagate from those of SB$_{\rm NB\times LAE}$ and SB$_{\rm NB\times NonLAE}$. We present the radial profiles of the SB$_{\rm NB\times LAE}$, SB$_{\rm NB\times NonLAE}$, and SB$_{\rm NB}$ of the *all* sample and *bright* subsample in Figure 4.5.

We use Fisher's method (Fisher 1970) to estimate the S/N ratios of SB$_{\rm NB}$ over all the radial bins, following Kakuma et al. (2021). In general, a p-value is expressed as

$$p = \int_{\rm S/N}^{\infty} \mathcal{N}(x; \mu = 0, \sigma = 1)\mathrm{d}x, \tag{4.5}$$

where $\mathcal{N}(x; \mu = 0, \sigma = 1)$ is a Gaussian distribution with an expected value $\mu = 0$ and a variance $\sigma^2 = 1$. We thus use this equation to convert the S/N ratio in the i-th radial bin (S/N$_i$) into the p-value in that bin (p_i). The χ^2 value over all the radial bins ($1 \leq i \leq N$), $\hat{\chi}^2$, is then calculated as $\hat{\chi}^2 = -2\sum_{i=1}^{N} \ln(p_i)$. Since $\hat{\chi}^2$ follows a χ^2_{2N} distribution with $2N$ degrees of freedom, $\chi^2(x; \mathrm{dof} = 2N)$, the p-value over all the radial bins, $\hat{p}$, is derived as

$$\hat{p} = \int_{\hat{\chi}^2}^{\infty} \chi^2(x; \mathrm{dof} = 2N)\mathrm{d}x. \tag{4.6}$$

We convert this to the S/N ratio over all the radial bins by solving Equation (4.5) for S/N. We use the radial bins at < 1 cMpc.

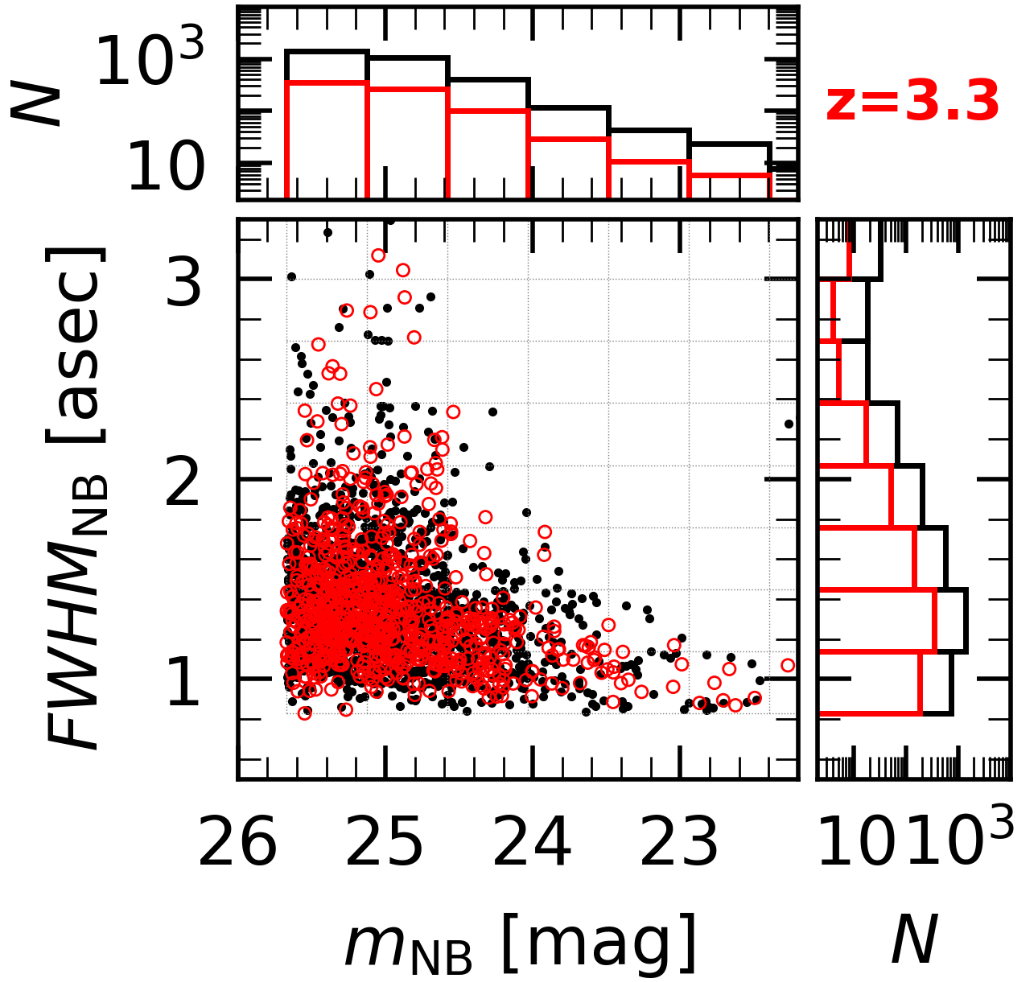

Figure 4.4 **Center:** FWHM$_{\rm NB}$ and $m_{\rm NB}$ distributions of the *all* sample at $z = 3.3$ (red circles), and the corresponding NonLAEs (black dots). **Top:** $m_{\rm NB}$ histogram of the LAEs and NonLAEs (red and black bars, respectively). **Right:** Same as the top panel, but for FWHM$_{\rm NB}$.

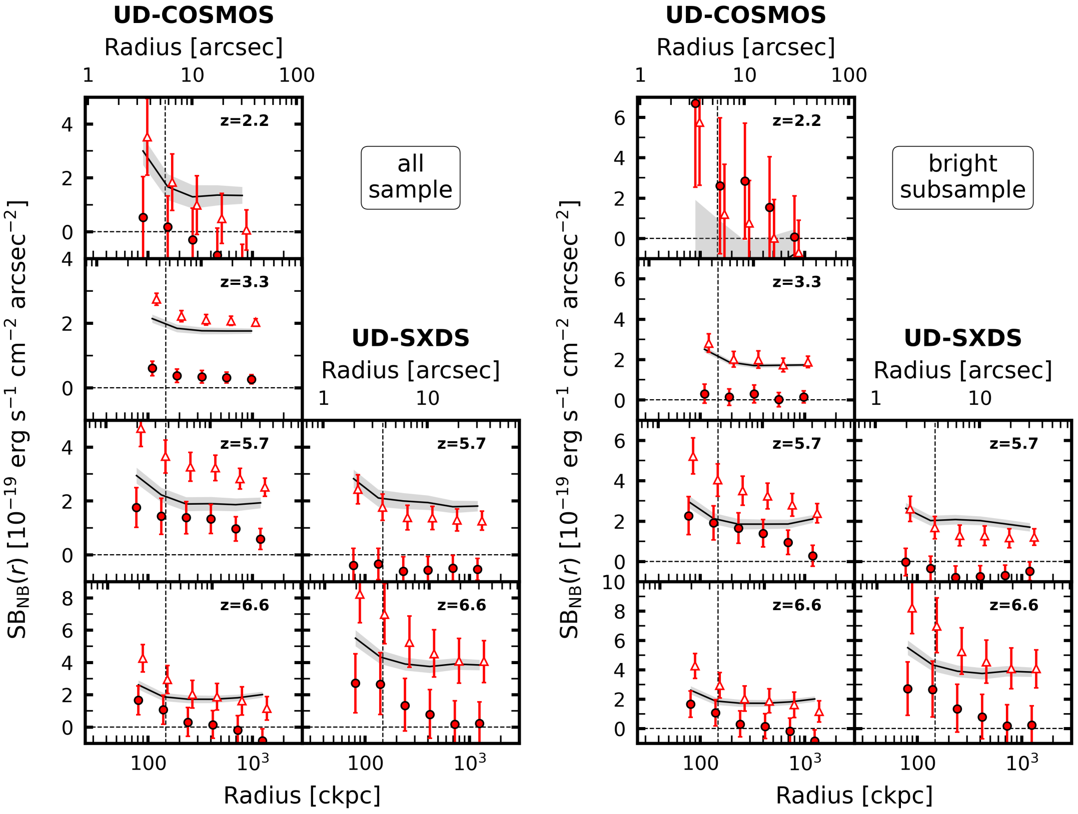

(a) (b)

Figure 4.5 **Left:** SB radial profiles of the *all* sample in the UD-COSMOS (left column) and UD-SXDS (right column) fields, at $z = 2.2$, 3.3, 5.7, and 6.6 (from top to bottom rows). The red triangles and circles show SB before and after systematics subtraction ($\mathrm{SB_{NB\times LAE}}$ and $\mathrm{SB_{NB}}$), respectively. The black solid lines represent the systematics that are estimated with the NonLAEs ($\mathrm{SB_{NB\times NonLAE}}$). The red error bars and gray shaded area are the 1σ uncertainties estimated by the bootstrap method. The vertical black dashed line represents R_{vir} of a DMH with $M_{\mathrm{h}} = 10^{11}\ M_{\odot}$, while the horizontal black line represents SB $= 0$. The data points of $\mathrm{SB_{NB\times LAE}}$ are slightly shifted along the horizontal axis for clarity. **Right:** Same as the left panels, but for the *bright* subsample.

The black vertical dashed lines in Figure 4.5 indicate $R_{\rm vir}$. Following the observational results by Ouchi et al. (2010) and Kusakabe et al. (2018), we assume that the DMHs hosting LAEs have $M_{\rm h}$ of 10^{11} $M_\odot$ at all the redshifts, which corresponds to a $R_{\rm vir}$ value of ~ 150 ckpc.

As presented in the Figure, at $z = 2.2$, we unfortunately see no clear detection for the *all* sample, although $\rm SB_{NB\times LAE}$ slightly exceeds $\rm SB_{NB\times NonLAE}$ for the *bright* subsample with S/N = 1.5. At $z = 3.3$, $\rm SB_{NB}$ of the *all* sample is significantly positive over wide scales from ~ 100 ckpc to 1 cMpc with S/N = 4.1. At $z = 5.7$, $\rm SB_{NB}$ is significantly positive at $\sim 80 - 10^3$ ckpc for the *all* sample and *bright* subsample in the UD-COSMOS field with S/N = 4.6 and 4.1, respectively. Averaging $\rm SB_{NB}$ of the *all* sample in both fields with weights of the number of the LAEs in each field, we identify a tentatively positive signal with S/N = 1.6. At $z = 6.6$, $\rm SB_{NB}$ are positive at $\sim 80 - 200$ ckpc in both fields. Averaging $\rm SB_{NB}$ over the two fields, we tentatively identify a positive signal with S/N = 2.3. We find that the emission SB at $z = 3.3 - 6.6$ is as diffuse as $\sim 10^{-20} - 10^{-19}$ erg s^{-1} cm^{-2} arcsec^{-2}. We note that $\rm SB_{NB\times LAE}$ in the UD-SXDS field is systematically lower than $\rm SB_{NB\times NonLAE}$, as reported in Kakuma et al. (2021).

4.3.2 UV Continuum Surface Brightness

UV continuum emission might contribute to the $\rm SB_{NB}$ in addition to the Lyα line emission. We thus estimate SB of the UV continuum emission, $\mathrm{SB}_{\mathrm{cont},\nu}$, using

$$\mathrm{SB}_{\mathrm{cont},\nu} < \mathrm{SB}_{\mathrm{BB},\nu} \equiv \mathrm{SB}_{\mathrm{BB\times LAE},\nu} - \mathrm{SB}_{\mathrm{BB\times random},\nu}, \tag{4.7}$$

where $\mathrm{SB}_{\mathrm{BB\times LAE},\nu}$ ($\mathrm{SB}_{\mathrm{BB\times random},\nu}$) represents the SB value that is derived from the cross-correlation function between the BB images and LAEs (random sources) in units of erg s^{-1} cm^{-2} Hz^{-1} arcsec^{-2}. Here $SB_{\mathrm{BB\times random},\nu}$ is for estimating the sky background. We use random sources, not NonLAEs, since it is difficult to match the $\mathrm{FWHM_{NB}}$-$m_{\rm NB}$ distributions of NonLAEs with those of the LAEs due to the faintness of the LAEs in the BB. Since $\mathrm{SB}_{\mathrm{BB\times random},\nu}$ neglects signals from the PSF, $\mathrm{SB}_{\mathrm{BB},\nu}$ should be treated as the upper limit of $\mathrm{SB}_{\mathrm{cont},\nu}$. We find that the values of $\mathrm{SB}_{\mathrm{cont},\nu}$ at $z = 2.2 - 6.6$ are consistent with null detection within $\sim (1 - 2)\sigma$ uncertainties. Additionally, we confirm that the UV continuum emission contributing to $\rm SB_{NB}$, i.e.,

$\mathrm{SB}_{\mathrm{cont},\nu} \times \mathrm{FWHM}_{\mathrm{NB}}$, is roughly negligible compared to $\mathrm{SB}_{\mathrm{NB}}$. Therefore, we hereafter assume that $\mathrm{SB}_{\mathrm{NB}}$ is equivalent to $\mathrm{SB}_{\mathrm{Ly}\alpha}$.

4.3.3 Lyα Surface Brightness

Given that $\mathrm{SB}_{\mathrm{NB}} = \mathrm{SB}_{\mathrm{Ly}\alpha}$, we identify very diffuse ($\sim 10^{-20} - 10^{-19}$ erg s^{-1} cm^{-2} arcsec^{-2}) Lyα signals beyond R_{vir} around the *all* sample LAEs at $z = 3.3$ at the 4.1σ level. We also potentially detect positive signals around the *all* sample LAEs at $z = 5.7$ and 6.6 and *bright* subsample LAEs with S/N ~ 2 when we take the averages over the two fields. A very tentative (1.5σ) signal is found around the *bright* sample LAEs at $z = 2.2$. These results imply the potential existence of Lyα emission that is diffusely extended outside R_{vir} around the LAEs at $z = 3.3 - 6.6$, and potentially at $z = 2.2$.

Again, a major update compared to Kakuma et al. (2021) is that we apply the intensity mapping technique newly to the CHORUS data to investigate extended Lyα emission at $z = 2.2 - 3.3$. In particular, we identify extended Lyα emission around the $z = 3.3$ LAEs with the S/N levels comparable or higher than those at $z = 5.7$ and 6.6, probably thanks to the good image sensitivity ($\sim 2 \times 10^{-20}$ erg s^{-1} cm^{-2} arcsec^{-2}) and the large number of LAEs at $z = 3.3$ ($N_{\mathrm{LAE}} = 762$). Our results at $z = 5.7$ and 6.6 are consistent with those obtained in Kakuma et al. (2021), which is as expected from similar properties of the LAEs of Kakuma et al. (2021) and our *all* sample, such as N_{LAE}, the L_{Lya} ranges, and the sky distributions (Section 4.1.2). In the next section, we compare our results with previous work including Kakuma et al. (2021) in detail.

4.3.4 Comparison with Previous Work

We compare our $\mathrm{SB}_{\mathrm{Ly}\alpha}$ radial profiles with those of previous studies at $z \sim 2.2$, 3.3, 5.7, and 6.6 in Figure 4.6. We compile the data taken from Momose et al. (2014), Momose et al. (2016), Leclercq et al. (2017), Wisotzki et al. (2018), Wu et al. (2020), and Kakuma et al. (2021), which are summarized in Table 4.3. Because SB is affected by the cosmological dimming effect, all the $\mathrm{SB}_{\mathrm{Ly}\alpha}$ profiles, including ours, are scaled by $(1+z)^{-4}$ to $z = 2.2$, 3.3, 5.7, and 6.6 in each panel. We also shift the radii of the $\mathrm{SB}_{\mathrm{Ly}\alpha}$ profiles in units of cpkc by $(1+z)$, while fixing the radii in pkpc. For our samples at $z = 5.7$ and 6.6, we hereafter present $\mathrm{SB}_{\mathrm{Ly}\alpha}$ averaged at each redshift over the UD-COSMOS and UD-SXDS fields weighting by the number of LAEs in each field, unless otherwise stated.

Although the $\mathrm{SB}_{\mathrm{Ly}\alpha}$ profiles are measured under different seeing sizes, the typical image PSF FWHMs are as small as $\lesssim 1.''5$, corresponding to $\lesssim 40-60$ ckpc at $z = 2-7$ (e.g. Momose et al. 2014; Ono et al. 2021). Since we focus on $\mathrm{SB}_{\mathrm{Ly}\alpha}$ profiles at larger scales of $\gtrsim 100$ ckpc, PSF differences are unlikely to affect the following discussions.

Momose et al. (2016) found that $\mathrm{SB}_{\mathrm{Ly}\alpha}$ profiles depend on $L_{\mathrm{Ly}\alpha}$ of the galaxy. To avoid this dependency, we take the data from Momose et al. (2014), Momose et al. (2016), and Kakuma et al. (2021), because their LAEs have $L_{\mathrm{Ly}\alpha}$ values similar to those of our *all* samples in the same $2''$-diameter aperture size. We additionally take the data from Leclercq et al. (2017), Wisotzki et al. (2018), and Wu et al. (2020), but these samples have different $L_{\mathrm{Ly}\alpha}$ values measured in different aperture sizes. Therefore, for precise comparisons, we normalize the $\mathrm{SB}_{\mathrm{Ly}\alpha}$ profiles of these samples such that $\mathrm{SB}_{\mathrm{Ly}\alpha}$ integrated over a central $2''$-diameter aperture ($= 4\pi d_{\mathrm{L}}^2 \int_{0''}^{1''} \mathrm{SB}_{\mathrm{Ly}\alpha}(r) \cdot 2\pi r dr$) becomes equal to $L_{\mathrm{Ly}\alpha}$ of our *all* sample at each redshift.

The top left panel in Figure 4.6 presents $\mathrm{SB}_{\mathrm{Ly}\alpha}$ radial profiles at $z = 2.2$. We compare the results of Momose et al. (2016, $L_{\mathrm{Ly}\alpha} = 10^{42.6}$ erg s^{-1} subsample) against our *all* sample. We found that the $\mathrm{SB}_{\mathrm{Ly}\alpha}$ profile of Momose et al. (2016) is in good agreement with that of our *all* sample at $r \sim 100$ ckpc.

In the top right panel of Figure 4.6, we show the $\mathrm{SB}_{\mathrm{Ly}\alpha}$ profiles at $z = 3.3$. We compare the results of Momose et al. (2014, $z = 3.1$ LAEs), Leclercq et al. (2017, an individual LAE MUSE#106), and Wisotzki et al. (2018, $L_{\mathrm{Ly}\alpha} > 10^{42}$ erg s^{-1} subsample at $z = 3 - 4$), and our *all* sample. The $\mathrm{SB}_{\mathrm{Ly}\alpha}$ profiles from the literature approximately agree with that of our *all* sample even at $r \sim R_{\mathrm{vir}}$. We additionally show the results from a subsample of Matsuda et al. (2012) with continuum magnitudes $BV \equiv (2B + V)/3$ of $26 < BV < 27$ (typical value range for LAEs), where B and V are B- and V-band magnitudes measured with the Subaru/SC. The $\mathrm{SB}_{\mathrm{Ly}\alpha}$ profile of Matsuda et al. (2012) also agrees with that of our *all* sample around $r \sim R_{\mathrm{vir}}$. We note that, although the results of Leclercq et al. (2017) are represented by their individual LAE MUSE#6905, their LAEs have similar $\mathrm{SB}_{\mathrm{Ly}\alpha}$ profiles when the amplitudes are normalized to match the $L_{\mathrm{Ly}\alpha}$ values at $r \leq 1''$.

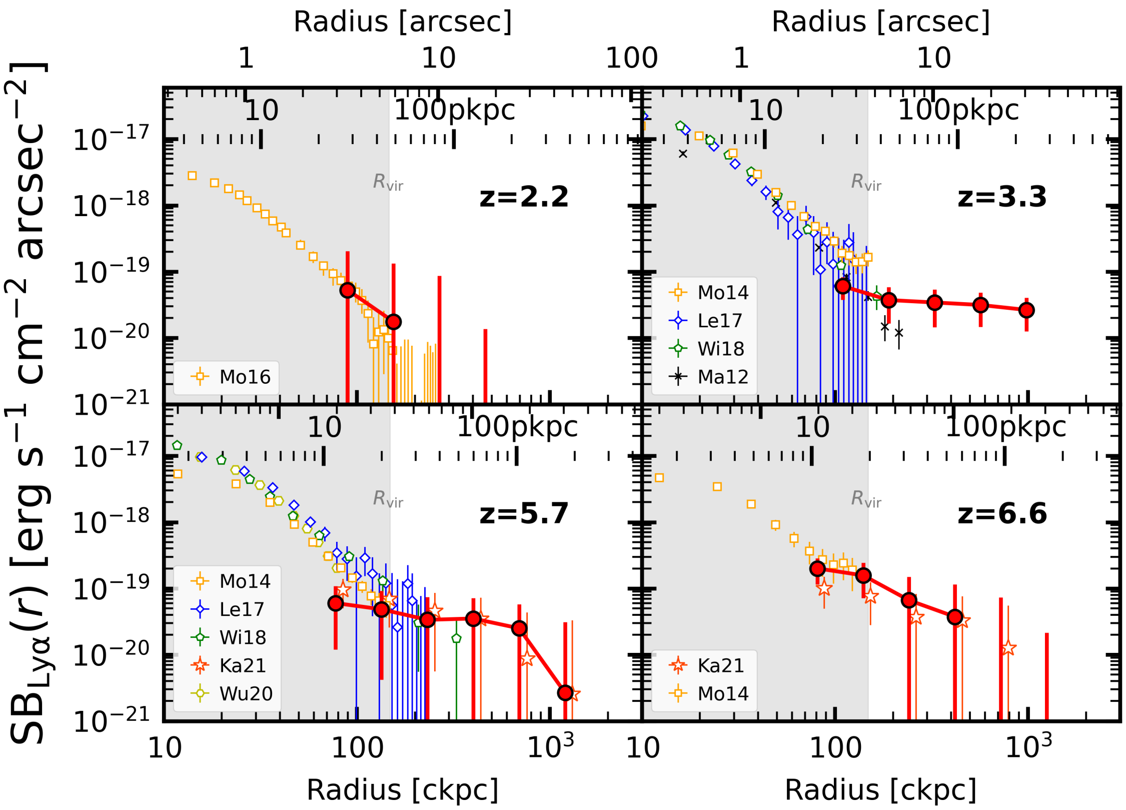

Figure 4.6 Comparison of the $\mathrm{SB_{Ly\alpha}}$ radial profiles at $z = 2.2$ (top left), 3.3 (top right), 5.7 (bottom left), and 6.6 (bottom right). All the $\mathrm{SB_{Ly\alpha}}$ profiles are corrected by $(1+z)^{-4}$ to match to each redshift. The gray shaded area illustrates the regions whose radius is smaller than $R_{\rm vir}$ of a DMH with $M_{\rm h} = 10^{11}\ M_\odot$. The filled red circles show the $\mathrm{SB_{Ly\alpha}}$ profiles of our *all* sample. The profiles at $z = 5.7$ and 6.6 are averaged over the UD-COSMOS and UD-SXDS fields. The other symbols represent the profiles taken from previous studies: Matsuda et al. (2012, Ma12: black crosses), Momose et al. (2014, 2016, Mo14, Mo16: orange squares), Leclercq et al. (2017, Le17: blue diamonds), Wisotzki et al. (2018, Wi18: green pentagons), Wu et al. (2020, Wu20: yellow hexagons), and Kakuma et al. (2021, Ka21: red stars). See Table 4.3 for details of these samples. We omit the data points below the detection limits defined in the literature. The $\mathrm{SB_{Ly\alpha}}$ profiles taken from Leclercq et al. (2017), Wisotzki et al. (2018), and Wu et al. (2020) are normalized such that $L_{\rm Ly\alpha}$ values measured in a central 2″ diameter equal to those of our *all* sample at each redshift. Some data points are slightly shifted along the horizontal axes for clarity. The $\mathrm{SB_{Ly\alpha}}$ profiles of our *all* sample are in good agreement with those taken from the literature.

Table 4.3 Summary of the observational studies used for comparison.

Reference	z	$\log L_{\mathrm{Ly}\alpha}$ [erg s^{-1}]	Sample	Method
$z \sim 2.2$				
This Work (*all* sample)	2.2	42.5	289 LAEs	intensity mapping (mean)
Momose et al. (2016)	2.2	42.6	710 LAEs ($L_{\mathrm{Ly}\alpha} \geq 10^{42.4}$ erg s^{-1})	stacking (mean)
$z \sim 3.3$				
This Work (*all* sample)	3.3	42.5	762 LAEs	intensity mapping (mean)
Momose et al. (2014)	3.1	42.7	316 LAEs	stacking (mean)
Leclercq et al. (2017)	3.28	[42.5]	LAE MUSE#106*	individual detection
Wisotzki et al. (2018)	$3-4$	[42.5]	18 LAEs ($L_{\mathrm{Ly}\alpha} > 10^{42}$ erg s^{-1})	stacking (median)
Matsuda et al. (2012)	3.1	—	894 LAEs ($26 < BV < 27$)†	stacking (median)
$z \sim 5.7$				
This Work (*all* sample)	5.7	42.8	650 LAEs	intensity mapping (mean)
Momose et al. (2014)	5.7	42.7	397 LAEs	stacking (mean)
Leclercq et al. (2017)	5.98	[42.8]	LAE MUSE#547*	individual detection
Wisotzki et al. (2018)	$5-6$	[42.8]	6 LAEs ($L_{\mathrm{Ly}\alpha} > 10^{42}$ erg s^{-1})	stacking (median)
Wu et al. (2020)	5.7	[42.8]	310 LAEs	stacking (median)
Kakuma et al. (2021)	5.7	42.9	425 LAEs	intensity mapping (mean)
$z \sim 6.6$				
This Work (*all* sample)	6.6	43.0	80 LAEs	intensity mapping (mean)
Momose et al. (2014)	6.6	42.7	119 LAEs	stacking (mean)
Kakuma et al. (2021)	6.6	42.8	396 LAEs	intensity mapping (mean)

Columns: (1) Reference. (2) Redshift. (3) Mean or median Lyα luminosity of the sample within a $2''$-diameter aperture. We normalize the SB$_{\mathrm{Ly}\alpha}$ profiles of Leclercq et al. (2017), Wisotzki et al. (2018), and Wu et al. (2020) such that SB$_{\mathrm{Ly}\alpha}$ integrated over a central $2''$-diameter aperture becomes equal to $L_{\mathrm{Ly}\alpha}$ of our *all* sample at each redshift, which are indicated by the brackets. (4) Sample used for comparison. The parentheses indicate specific subsamples. (5) Method for deriving the SB$_{\mathrm{Ly}\alpha}$ profiles.

* ID of the individual LAE. See Section 4.3.4 for the variance among the individual LAEs.

† $BV \equiv (2B + V)/3$.

The $\mathrm{SB_{Ly\alpha}}$ profiles at $z = 5.7$ are displayed in the bottom left panel of Figure 4.6. We compare the results of Momose et al. (2014, $z = 5.7$ LAEs), Leclercq et al. (2017, an individual LAE MUSE#547), Wisotzki et al. (2018, $L_{\mathrm{Ly\alpha}} > 10^{42}$ erg s^{-1} subsample at $z = 5 - 6$), Wu et al. (2020, $z = 5.7$ LAEs), Kakuma et al. (2021, $z = 5.7$ LAEs), and our *all* sample. The $\mathrm{SB_{Ly\alpha}}$ profile of our *all* sample agrees well with those of Momose et al. (2014), Leclercq et al. (2017), Wisotzki et al. (2018) and Wu et al. (2020) at $r \sim 80 - 200$ ckpc, and with that of Kakuma et al. (2021) up to $r \sim 1$ cMpc.

The bottom right panel of Figure 4.6 shows $\mathrm{SB_{Ly\alpha}}$ profiles at $z = 6.6$ taken from Momose et al. (2014, $z = 6.6$ LAEs), Kakuma et al. (2021, $z = 6.6$ LAEs), and our *all* sample. The $\mathrm{SB_{Ly\alpha}}$ profile of our *all* sample is consistent with those of Momose et al. (2014) and Kakuma et al. (2021) up to the scales of $r \sim 100$ ckpc and 1 cMpc, respectively.

In summary, our $\mathrm{SB_{Ly\alpha}}$ profiles are in good agreement with those of the previous studies at each redshift, provided that the LAEs have similar $L_{\mathrm{Ly\alpha}}$ values at $r \leq 1''$. Our $\mathrm{SB_{Ly\alpha}}$ profiles ($r \gtrsim 80$ ckpc) are smoothly connected with the inner ($r \lesssim 100$ ckpc) profiles taken from the literature at ~ 100 ckpc, and extend to larger scales.

In Figure 4.7, we compare the $\mathrm{SB_{cont,\nu}}$ radial profiles between Momose et al. (2014, 2016) and our *all* sample at $z = 2.2$, 3.3, and 5.7 (the data of Momose et al. 2014, 2016 are of the same LAEs as used in Figure 4.6). We find that the $\mathrm{SB_{cont,\nu}}$ profiles roughly agree at $r \lesssim 400$ ckpc, although the uncertainties are large. The $\mathrm{SB_{cont,\nu}}$ profiles are much less extended than $\mathrm{SB_{Ly\alpha}}$ profiles, which was also suggested by Momose et al. (2014), Momose et al. (2016), and Wu et al. (2020). We note the profiles at $z = 6.6$ are not compared here because our sample is ~ 0.3 dex brighter than that of Momose et al. (2014).

4.4 Redshift Evolution of Lyα Emission Radial Profiles

In Figure 4.8, we compare the $\mathrm{SB_{Ly\alpha}}$ profiles of our *bright* subsamples at $z = 2.2 - 6.6$ as a function of radius in units of ckpc. We also present the results taken from Momose et al. (2014, $z = 5.7$ and 6.6 LAEs) and Wisotzki et al. (2018, $L_{\mathrm{Ly\alpha}} > 10^{42}$ erg s^{-1} subsample at $z = 3 - 4$). Because our *bright* subsamples have uniform $L_{\mathrm{Ly\alpha}}$ values ($\sim 10^{42.9} - 10^{43.0}$ erg s^{-1}) over $z = 2.2 - 6.6$, the $L_{\mathrm{Ly\alpha}}$ differences between the

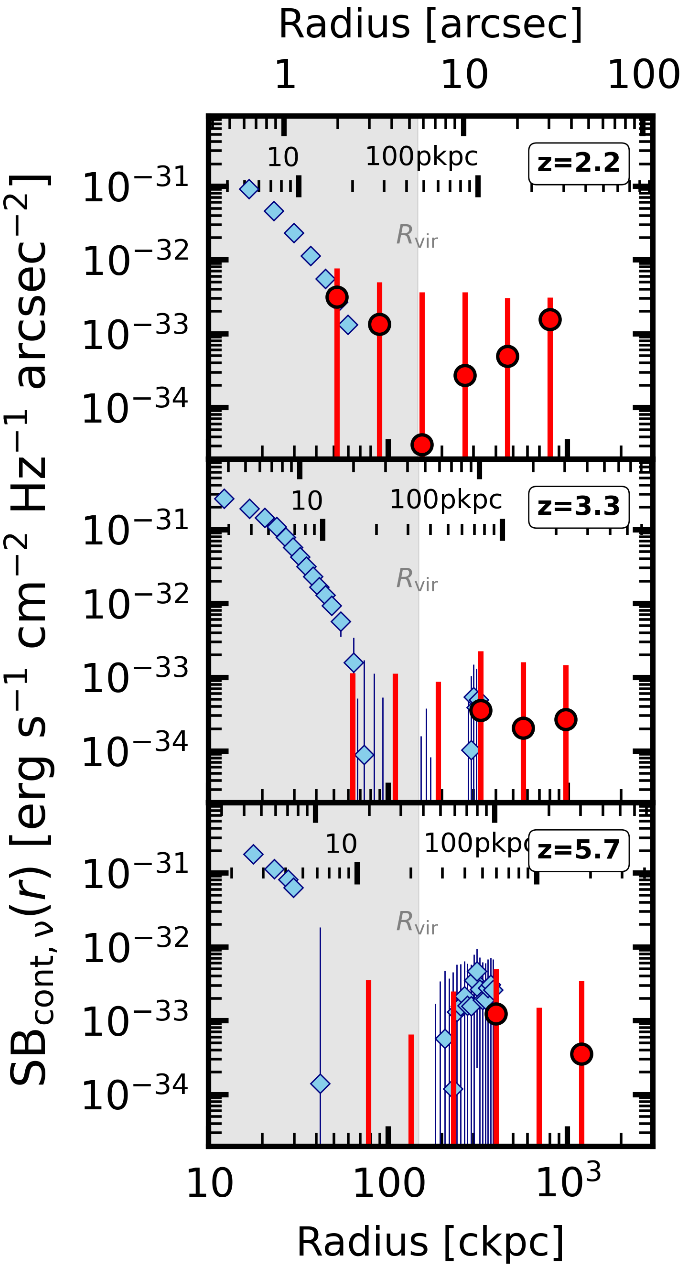

Figure 4.7 Comparison of the $\mathrm{SB}_{\mathrm{cont},\nu}$ radial profiles at $z = 2.2$ (top), 3.3 (middle), and 5.7 (bottom). The red circles and cyan diamonds show the $\mathrm{SB}_{\mathrm{cont},\nu}$ profiles of our *all* sample and Momose et al. (2014, 2016), respectively (we use the data of Momose et al. 2016 at $z = 2.2$, and of $z = 3.1$ and 5.7 LAEs of Momose et al. 2014 at $z = 3.3$ and 5.7, respectively). The gray shaded area illustrates the regions inside $R_{\rm vir}$ of a DMH with $M_{\rm h} = 10^{11}\ M_\odot$. The $\mathrm{SB}_{\mathrm{cont},\nu}$ profiles of our *all* sample are in good agreement with those of Momose et al. (2014, 2016).

redshifts are unlikely to influence the following discussion.

The top panel of Figure 4.8 shows the observed $\mathrm{SB}_{\mathrm{Ly}\alpha}$ profiles. We identify no significant difference among the $\mathrm{SB}_{\mathrm{Ly}\alpha}$ profiles beyond the 1σ uncertainties at $r \sim 100 - 1000$ ckpc over $z = 2.2 - 6.6$, while the uncertainties are large. This finding is consistent with that of Kakuma et al. (2021) at $z = 5.5 - 6.6$. There is no significant difference also in the profiles at $r < 100$ ckpc, which was also suggested by MUSE observations (Leclercq et al. 2017, see also Figure 11 of Byrohl et al. 2021) at $3 < z < 6$.

Observed $\mathrm{SB}_{\mathrm{Ly}\alpha}$ profiles are affected by the cosmological dimming effect. To correct for this effect, we shift the observed $\mathrm{SB}_{\mathrm{Ly}\alpha}$ profiles vertically by $(1+z)^4/(1+3.3)^4$ and horizontally by $(1+3.3)/(1+z)$, which are hereafter termed as the *intrinsic* profiles[4] (we match the profiles to $z = 3.3$ just for visibility). The *intrinsic* profiles are presented in the bottom panel of Figure 4.8. There is a roughly decreasing trend toward low redshifts, although those at $z = 2.2$ and 3.3 remain comparable due to the large uncertainties or might show an opposite trend.

To quantitatively investigate the evolution, we derive the *intrinsic* $\mathrm{SB}_{\mathrm{Ly}\alpha}$ profiles amplitudes at $r = 200$ ckpc, termed as $\mathrm{SB}^{\mathrm{intr}}_{\mathrm{Ly}\alpha}(r = 200\ \mathrm{ckpc})$, as a function of redshift. We fit the relation with $\mathrm{SB}^{\mathrm{intr}}_{\mathrm{Ly}\alpha}(r = 200\ \mathrm{ckpc}) \propto (1+z)^b$, where b is a constant, weighting $\mathrm{SB}^{\mathrm{intr}}_{\mathrm{Ly}\alpha}(r = 200\ \mathrm{ckpc})$ with $\sqrt{N_{\mathrm{LAE}}}$ at each redshift. We find that the best-fit value of b is ~ 3.1, which implies that the *intrinsic* $\mathrm{SB}_{\mathrm{Ly}\alpha}$ profile amplitudes decrease toward low redshifts roughly by $(1+z)^{-3}$ at a given radius in units of ckpc. This trend might correspond to decreasing density of hydrogen gas with cosmic time due to the cosmic expansion. Nevertheless, it is still difficult to draw a conclusion due to large uncertainties. We cannot rule out other or additional possibilities, such as Lyα escape fractions (e.g., Hayes et al. 2011; Konno et al. 2016). We also need to investigate the potential impact of the cosmic reionization on the neutral hydrogen density at $r \sim 100 - 1000$ ckpc around LAEs.

---

[4] The *intrinsic* here means correction for the cosmological dimming effect, not for the lensing effect as in Sections 1.5 and 2.1.

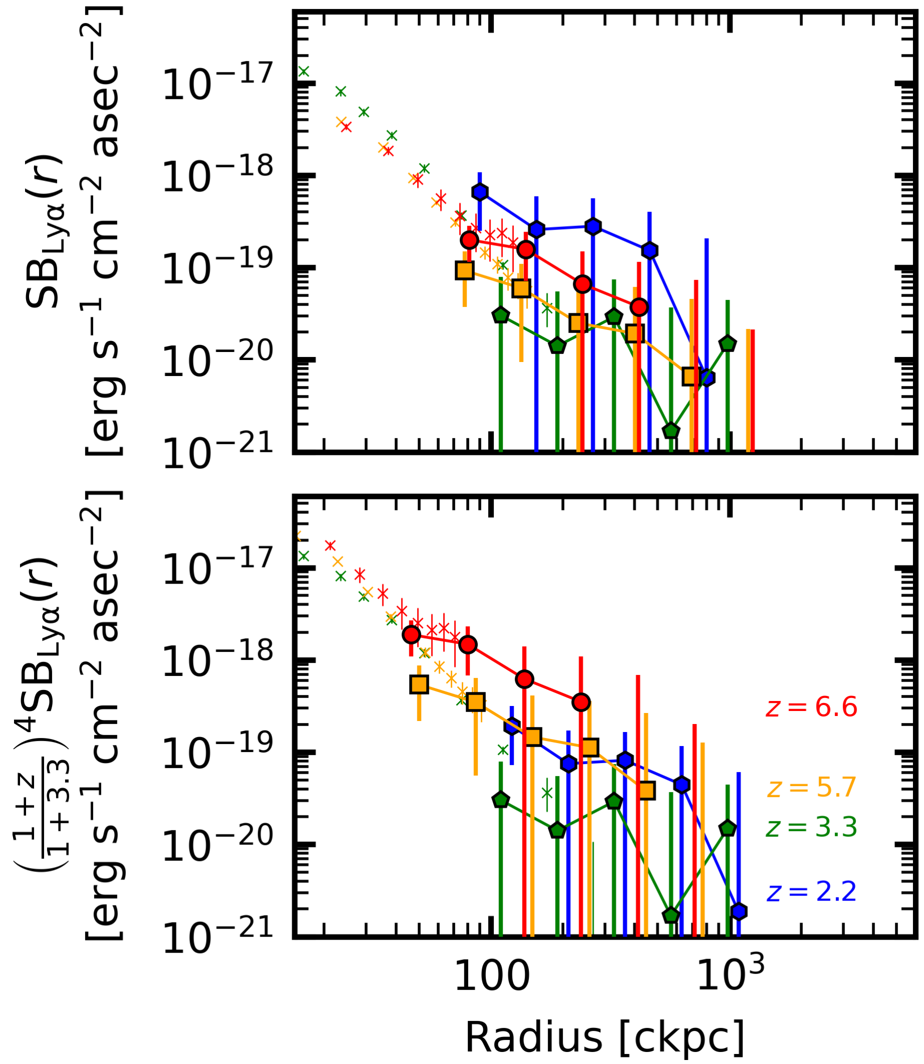

Figure 4.8 Comparison between $SB_{Ly\alpha}$ radial profiles at $z = 2.2 - 6.6$. **Top:** Observed $SB_{Ly\alpha}$ profiles. The blue hexagons, green pentagons, orange squares, and red circles represent the profiles of our *bright* subsamples at $z = 2.2$, 3.3, 5.7, and 6.6, respectively. The green, orange, and red crosses denote profiles taken from Wisotzki et al. (2018), Momose et al. (2014), and Momose et al. (2014), which are normalized to $z = 3.3$, 5.7, and 6.6, respectively. The $SB_{Ly\alpha}$ profile of Wisotzki et al. (2018) is normalized such that L_{Lya} in $r \leq 1''$ matches to that of our *all* sample (see Section 4.3.4). We again note that our profiles here are based on *bright* subsamples and thus differ from those shown in Figure 4.6. **Bottom:** Same as the top panel, but showing the profiles corrected for the cosmological dimming effect, i.e., the *intrinsic* $SB_{Ly\alpha}$ profiles. We tentatively identify an increasing trend roughly by $(1+z)^3$ toward high redshifts, albeit with the large uncertainties.

CHAPTER 5
DISCUSSIONS

5.1 Fractional Number Densities

In Chapters 2, we found that our SMFs reach $\sim 10^6\ M_\odot$ both at $z > 6$ and ~ 0 for the first time. Owing to these mass limits, we can now estimate how such low-mass galaxies are dominant in the cosmic history. This can be tested also in UV LFs, because the UV LFs reach -14 mag at both redshifts (Section 3).

In the top panel of Figure 5.1, we show the fractional number densities of galaxies of different stellar masses,

$$\frac{N(M_{\star,1}, M_{\star,2})}{N(10^6\ M_\odot, 10^{13}\ M_\odot)} = \frac{\int_{\log M_{\star,1}}^{\log M_{\star,2}} \Phi_\star(\log M_\star) \mathrm{d} \log M_\star}{\int_6^{13} \Phi_\star(\log M_\star) \mathrm{d} \log M_\star}, \tag{5.1}$$

as functions of the stellar-mass bin $[M_{\star,1}, M_{\star,2}]$ and redshift. The bins are defined as $[\log M_{\star,1}, \log M_{\star,2}] = [6, 7]$, [7,8], [8,10] and [10,13]. We adopt the Schechter function $\Phi_\star$ of Song et al. (2016, $z \sim 4$ and 5) and this work ($z \sim 0$, $6-7$, 8, and 9). Since the SMFs of Song et al. (2016) are not obtained down to $10^6\ M_\odot$, we extrapolate their Schechter functions to $M_\star = 10^6\ M_\odot$. The blue region shows the number fraction of the galaxies with $10^6 \leq M_\star \leq 10^7\ M_\odot$. The result shows that > 60 % of the all galaxies are less massive than $10^7\ M_\odot$ over $0 < z < 9$, which again highlights the prevalence of low-mass galaxies all through the cosmic history. The galaxies heavier than $10^8\ M_\odot$ and $10^{10}\ M_\odot$ emerge roughly at $z < 6$ and $z < 3$, respectively, as a result of galaxy growth. The latter appears as the knees in the SMFs (high-mass components of the double Schechter functions).

The bottom panel shows the fractional stellar mass densities (SMDs):

$$\frac{\rho_\star(M_{\star,1}, M_{\star,2})}{\rho_\star(10^6\ M_\odot, 10^{13}\ M_\odot)} = \frac{\int_{\log M_{\star,1}}^{\log M_{\star,2}} M_\star \Phi_\star(\log M_\star) \mathrm{d} \log M_\star}{\int_6^{13} M_\star \Phi_\star(\log M_\star) \mathrm{d} \log M_\star}. \tag{5.2}$$

The definitions of the bins and $\Phi_\star$ are the same as Equation (5.1). Even in the fractional SMDs, we find that the galaxies with $M_\star < 10^8\ M_\odot$ dominate ~ 30 % of the total SMDs at $z > 5$. The $M_\star^*$ galaxies ($10^8 < M_\star / M_\odot < 10^{10}$) also abundant ubiquitously over $0 < z < 9$. The massive ($M_\star > 10^{10}\ M_\odot$) galaxies start to contribute to the total SMDs at $z < 6$.

The evolutionary trend of the total SMD is shown in Figure 5.2. Here we adopt the total SMDs as an integration between the 10^8 and 10^{13} $M_\odot$ galaxies, which has widely been used in previous studies (e.g., Elsner et al. 2008; González et al. 2011; Mortlock et al. 2011; Stark et al. 2013; Duncan et al. 2014; Grazian et al. 2015; Song et al. 2016; Bhatawdekar et al. 2019).

We also derive the total SMDs below. For $z \sim 0$ and $6 - 9$, first, we randomly select a set of Schechter parameters from those sampled by the MCMC algorithm during the fitting of our SMFs. Second, we integrate the Schechter functions with the selected set of parameters over $10^8 \leq M_\star/M_\odot \leq 10^{13}$. Repeating these two steps 10^3 times generates a histogram of 10^3 SMDs in each z. We take the median values and the 68.3 percentiles as our best-fit values and 1σ statistical uncertainties of the total SMDs. We also add in quadrature the cosmic variance to the statistical uncertainty using the values of 0.3, 0.4, and 0.5 dex at $z \sim 6-7$, 8, and 9, respectively (Robertson et al. 2014; Ishigaki et al. 2015; Bhatawdekar et al. 2019), because the area of our data (HFF) is limited.

We show our total SMDs with the red circles in Figure 5.2. The results are compared with those taken from Elsner et al. (2008), Mortlock et al. (2011), González et al. (2011), Stark et al. (2013), Duncan et al. (2014), Oesch et al. (2014), Grazian et al. (2015), Song et al. (2016), and Bhatawdekar et al. (2019). Our total SMDs at $z \sim 0$ and $6 - 7$ agree with the increasing trend found in the literature, while those at $z \sim 8$ and 9 are slightly larger than those of Oesch et al. (2014) and Bhatawdekar et al. (2019).

If the total SMDs and the cosmic star-formation rate densities (SFRDs) are accurately measured, the time integral of the SFRDs should be consistent with the total SMDs. We show the evolution of the time-integrated SFRD model of Madau & Dickinson (2014) with the black solid curve, which decreases slowly by $(1+z)^{-3.9}$ at $z > 8$. Similar trends of the SFRD evolution were found in the studies of Finkelstein et al. (2015), McLeod et al. (2016), and Bhatawdekar et al. (2019; see also Ellis et al. 2013 and Madau 2018). Meanwhile, Oesch et al. (2018) claim that the SFRDs evolve more rapidly by $(1 + z)^{-10.9}$ at $z > 8$, which is shown with the blue solid curve. We calculate χ^2 values with our total SMDs against the smooth evolution model of Madau & Dickinson (2014) and the rapid evolution model of Oesch et al. (2018). We find that

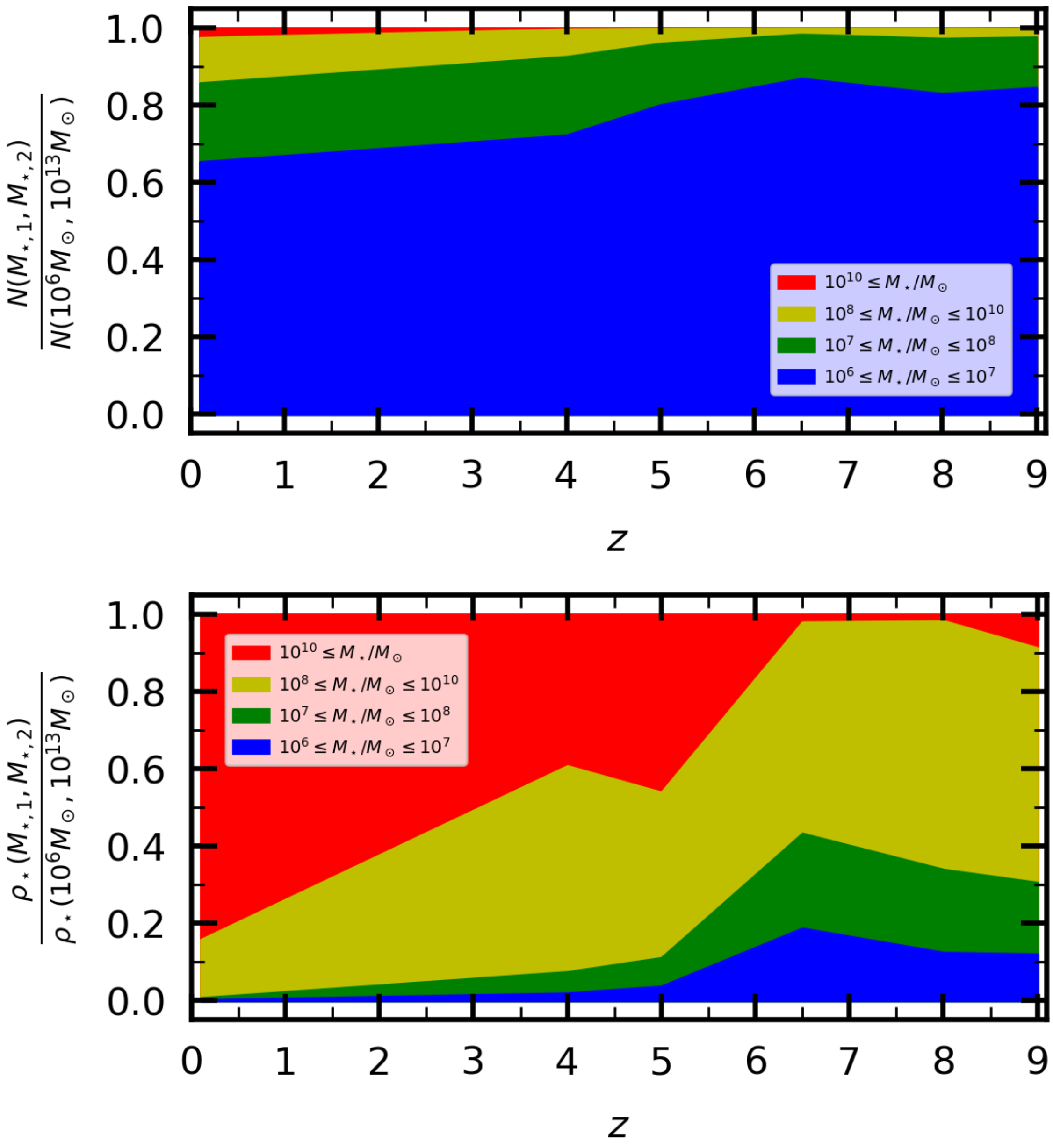

Figure 5.1 Fractional number and stellar mass densities of the galaxies (top and bottom panels, respectively). The $M_\star$ bins are shown in the legends.

χ^2 is the smaller for the smooth evolution model than for the rapid evolution model by a factor of ~ 6, implying that our results support the smooth evolution of the SFRDs at $z > 8$. The smooth evolution suggests that the star-formation efficiency is large at $z > 8$ (Harikane et al. 2018a; Oesch et al. 2018).

We next derive the fractional number densities of the galaxies in different UV magnitude bins:

$$\frac{N(M_{\rm UV,1}, M_{\rm UV,2})}{N(M_{\rm UV} \leq -14)} = \frac{\int_{M_{\rm UV,1}}^{M_{\rm UV,2}} \Phi_{\rm UV}(M_{\rm UV}){\rm d}M_{\rm UV}}{\int_{-\infty}^{-14} \Phi_{\rm UV}(M_{\rm UV}){\rm d}M_{\rm UV}}, \tag{5.3}$$

and the fractional contributions of the UV luminosity densities:

$$\frac{\rho_{\rm UV}(M_{\rm UV,1}, M_{\rm UV,2})}{\rho_{\rm UV}(M_{\rm UV} \leq -14)} = \frac{\int_{M_{\rm UV,1}}^{M_{\rm UV,2}} L_{\rm UV}\Phi_{\rm UV}(M_{\rm UV}){\rm d}M_{\rm UV}}{\int_{-\infty}^{-14} L_{\rm UV}\Phi_{\rm UV}(M_{\rm UV}){\rm d}M_{\rm UV}}, \tag{5.4}$$

where $L_{\rm UV}$ is the UV luminosity density corresponding to $M_{\rm UV}$, and $\Phi_{\rm UV}(M_{\rm UV})$ is the best-fit Schechter functions (this work at $z \sim 0$, Parsa et al. 2016 at $z \sim 1.9$ and 2.8, Bouwens et al. 2021c at $z \sim 3.8$, 4.9, and 5.9, and Ishigaki et al. 2018 at $z \sim 6-7$, 8, and 9). We adopt $[M_{\rm UV,1}, M_{\rm UV,2}] = [-16, -14]$, $[-18, -16]$, $[-20, -18]$, and $(-\infty, -20]$.

The results are shown in Figure 5.3. In the number fraction, we find that the faint galaxies with $M_{\rm UV} < -16$ mag are prevalent (> 60 %) all over the cosmic history. This result again implies the importance of investigating low-mass galaxies. Similarly, the luminosity densities are contributed largely from the galaxies fainter than -18 mag ($\sim 30-60$ %). The fraction of the $M_{\rm UV}^*$ galaxies ($M_{\rm UV} \sim (-21)-(-18)$ mag) are also large.

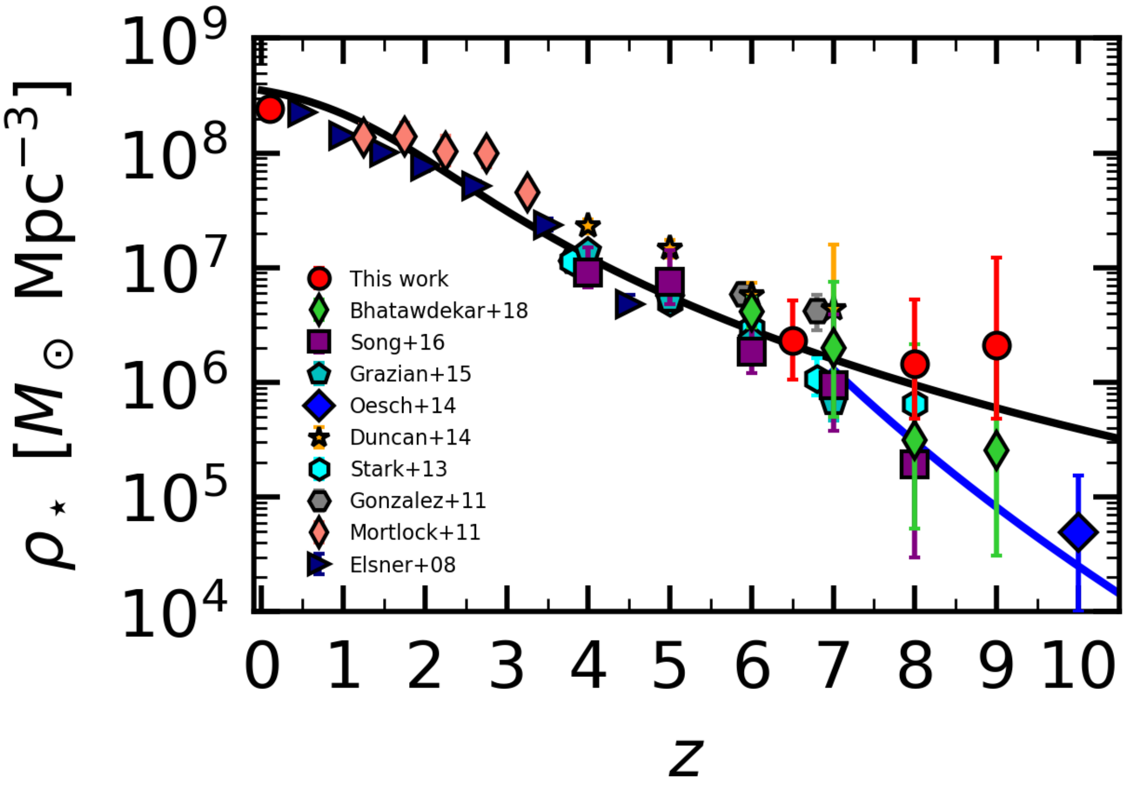

Figure 5.2 Redshift evolution of the total SMDs. The red circles show our total SMDs at $z \sim 0, 6-7, 8$, and 9. The other data points are taken from previous studies: Elsner et al. (2008, navy triangles), Mortlock et al. (2011, magenta diamonds), González et al. (2011, gray hexagons), Stark et al. (2013, cyan hexagons), Duncan et al. (2014, orange stars), Oesch et al. (2014, a blue diamond), Grazian et al. (2015, cyan pentagons), Song et al. (2016, purple boxes), and Bhatawdekar et al. (2019, green diamonds). The black and blue solid curves represent the time integration of the SFRD evolution presented in Madau & Dickinson (2014) and Oesch et al. (2018), respectively.

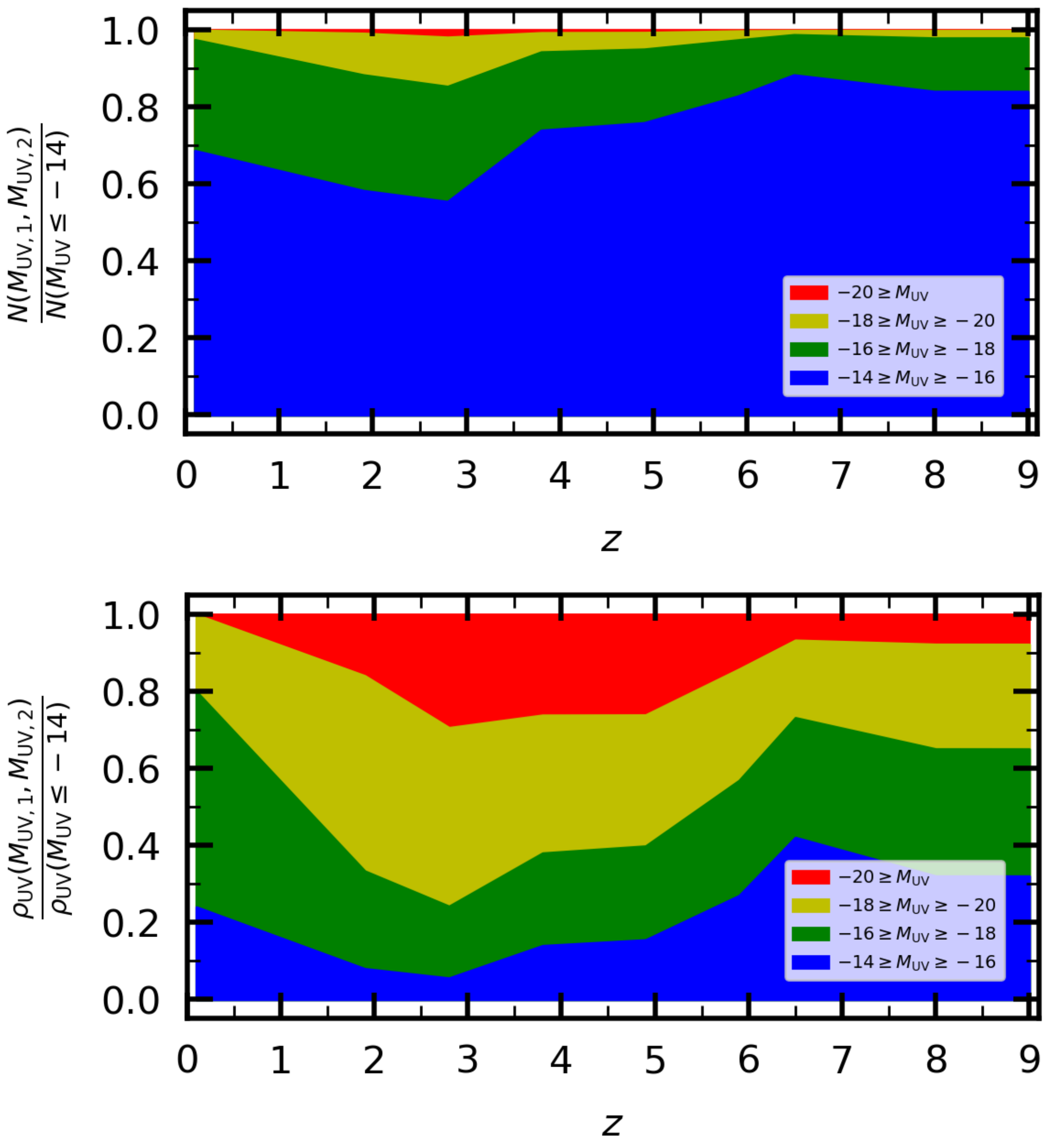

Figure 5.3 Fractional number and UV luminosity densities of the galaxies (top and bottom panels, respectively). The $M_{\rm UV}$ bins are shown in the legends.

5.2 Turnovers

In Chapter 2, we found that our SMF at $z \sim 0$ sharply drops at $M_\star \sim 10^6 - 10^7\ M_\odot$, while no such turnover is seen in the SMFs at $z > 6$ (Figure 2.10). Similarly in Chapter 3, we tentatively identified a turnover also in our UV LF at $z \sim 0$ around $M_{\rm UV} \sim -12$ to -11 mag (Figure 3.3), while UV LF turnovers at $z > 6$ are still controversial (Section 3.1). In this Section, we quantify at what stellar mass and UV absolute magnitude (turnover stellar mass, $M_\star^{\rm T}$, and magnitude, $M_{\rm UV}^{\rm T}$) and compare the results with predictions by simulations.

5.2.1 SMF Turnovers

At $z \sim 6 - 9$, we confirm no clear turnovers down to $M_\star \sim 10^6\ M_\odot$ in our SMFs. This implies that $M_\star^{\rm T} \lesssim 10^6\ M_\odot$. In the top panel of Figure 5.4, we show the best-fit Schechter function derived in Section 2.1 with the blue line.

To quantify $M_\star^{\rm T}$ at $z \sim 0$, we parametrize our SMF at $z \sim 0$ with

$$\Phi_\star(\log M_\star) = \begin{cases} \hat{\Phi}_{\star,{\rm Sch}}(\log M_\star) & \text{for } \log M_\star \geq \log M_\star^{\rm thr}, \\ \hat{\Phi}_{\star,{\rm Sch}}(\log M_\star) \times 10^{-\gamma_\star (\log M_\star - \log M_\star^{\rm thr})^2} & \text{otherwise,} \end{cases} \tag{5.5}$$

following Bouwens et al. (2017b) and Atek et al. (2018). We hereafter term this function as a truncated Schechter function. A threshold mass $M_\star^{\rm thr}$ and curvature $\gamma_\star$ are free parameters, and $\hat{\Phi}_{\star,{\rm Sch}}(\log M_\star)$ is the best-fit double Schechter function at $z \sim 0$ (Section 2.2). The best-fit truncated Schechter function is shown with the red solid line, whose parameters are $(\log M_\star^{\rm thr}, \gamma_\star) = (6.88^{+0.46}_{-0.40}, 1.56^{+3.44}_{-1.17})$. The value of $M_\star^{\rm T}$ is defined as the stellar mass at the peak of the SMF; i.e., $\frac{{\rm d}\Phi_\star}{{\rm d}\log M_\star}|_{M_\star = M_\star^{\rm T}} = 0$. Given that $M_\star^{\rm T} \ll M_\star^*$, $M_\star^{\rm T}$ is approximated as

$$\log M_\star^{\rm T} \sim \log M_\star^{\rm thr} - \frac{\alpha_{\star,{\rm low}} + 1}{2\gamma_\star}. \tag{5.6}$$

Using this equation, we obtain that $\log M_\star^{\rm T} = 6.71^{+0.60}_{-0.42}$. The red star represents the point where $M_\star = M_\star^{\rm T}$.

We compare $M_\star^{\rm T}$ at different redshifts in the bottom panel of Figure 5.4. The red point shows $M_\star^{\rm T}$ at $z \sim 0$ derived above. At $z \sim 1 - 5$, we show the lowest $M_\star$ limits

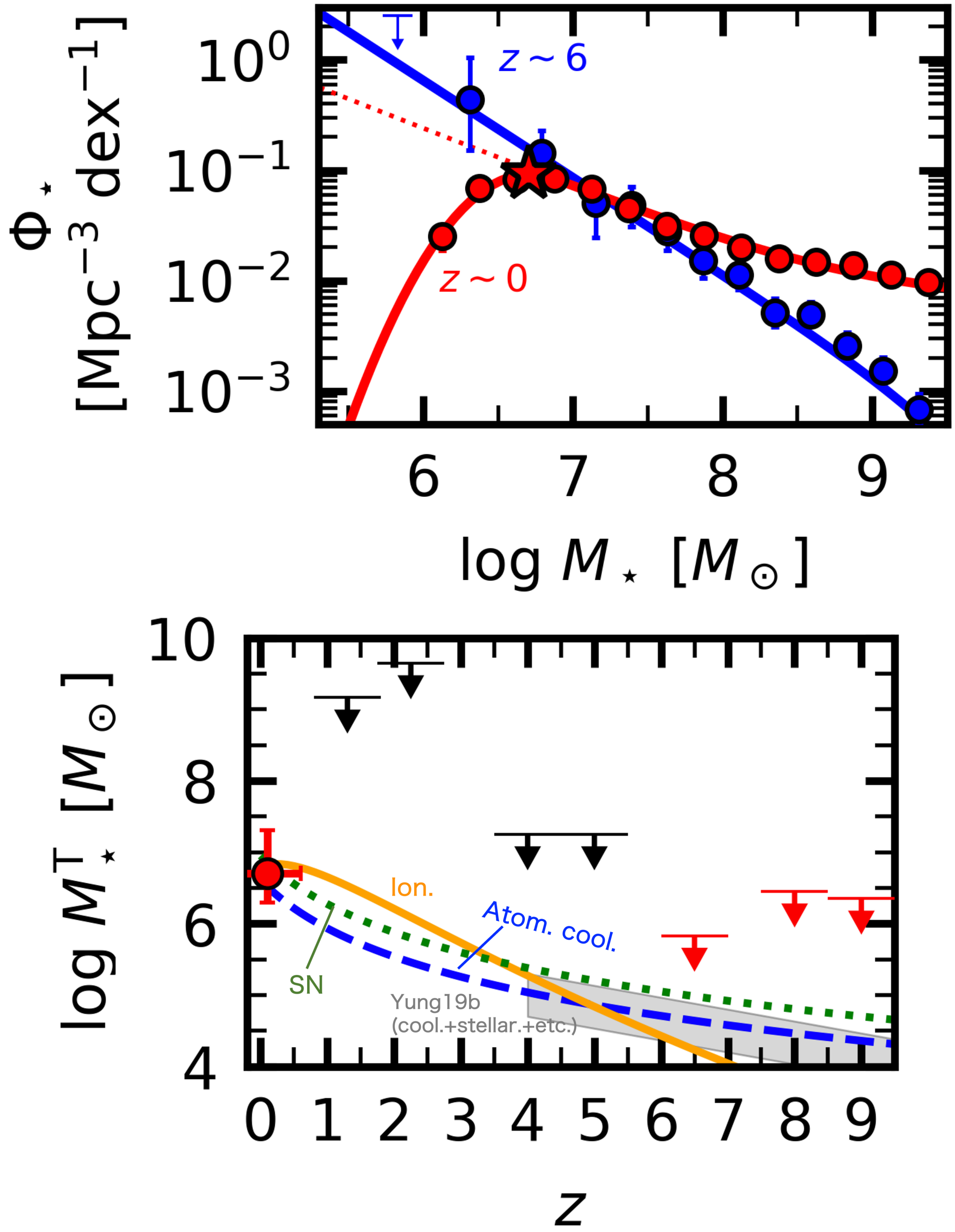

Figure 5.4 **Top:** SMFs at $z \sim 6-7$ (blue) and 0 (red). The blue line is the best-fit Schechter function at $z \sim 6-7$. The red solid and dotted lines represent the best-fit truncated Schechter and extrapolated Schechter functions, respectively, at $z \sim 0$. The red star indicates $M_\star = M^{\rm T}_\star$. **Bottom:** Comparison of $M^{\rm T}_\star$ at different redshifts. The $z \sim 0$ data point represents our estimation, while the upper limits refer to the lowest $M_\star$ limits of the SMFs (Davidzon et al. 2017 for $z \sim 1-2$, Song et al. 2016 for $z \sim 4$ and 5, and this work for $z \sim 6-9$). The orange solid, green dotted, and blue dashed lines show the models of the photoionization, SN feedback, and the cooling limit, respectively. The gray shaded area indicates the model of Yung et al. (2019b).

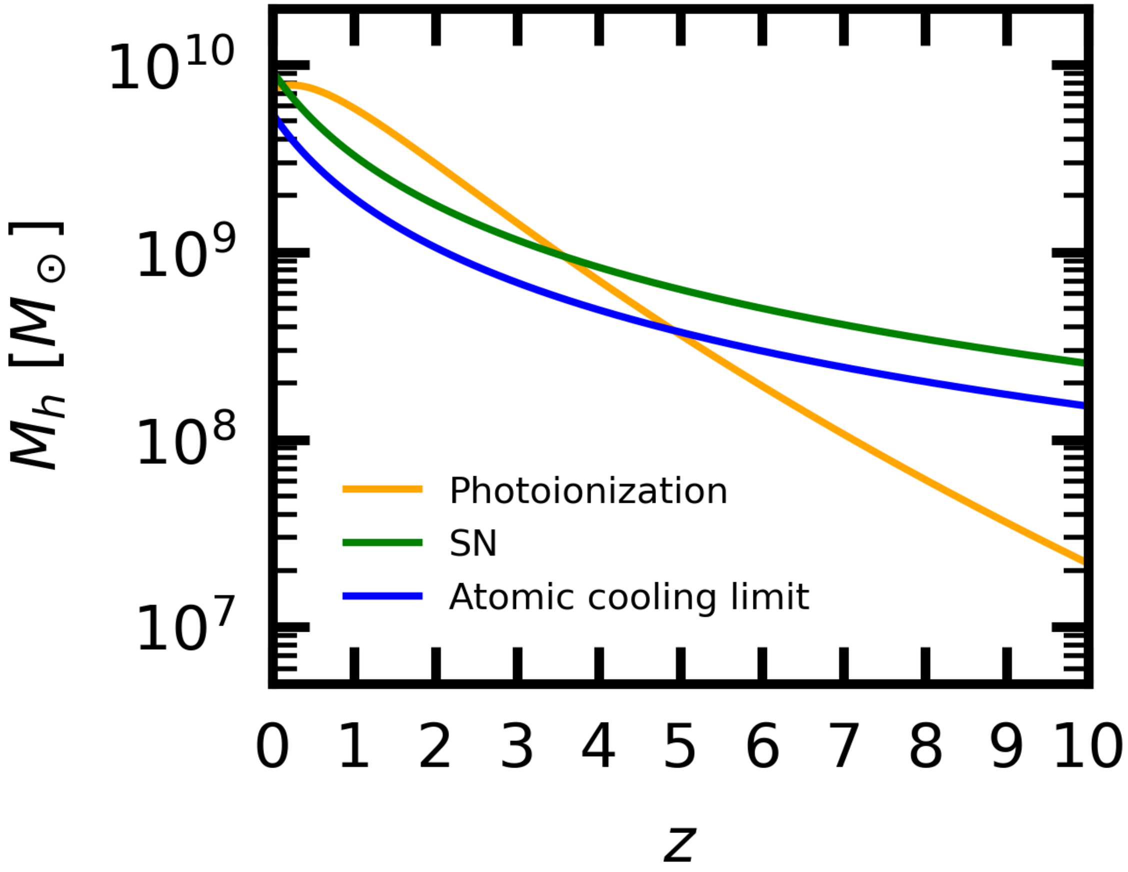

Figure 5.5 Redshift evolution of the critical halo masses in the models of the photoionization by the UVB (orange), SN feedback (green), and the atomic gas cooling limit (blue).

of the SMFs of Song et al. (2016) and Davidzon et al. (2017) as the upper limits of $M_\star^*$, since no turnovers are seen in their SMFs. Particularly comparing our $M_\star^{\rm T}$ at $z \sim 0$ and $6-7$, we can speculate that $M_\star^{\rm T}$ roughly increases with cosmic time, although the trend at $1 < z < 6$ are poorly constrained.

We compare our results with predictions by theoretical work. The blue dashed, green dotted, and orange solid lines represent the critical stellar masses, below which star formation is completely suppressed. These models are converted from the critical halo masses defined by the suppression mechanisms mentioned in Section 1.2.1: the atomic gas cooling limit, stellar feedback, and the photoionization by the UVB radiation.

- *Atomic gas cooling limit.* The critical halo mass corresponding to the atomic cooling limit, $M_{\rm cool,h}$, is given as

  $$M_{\rm cool,h} = 5.5 \times 10^9 (1+z)^{-1.5}\ M_\odot \tag{5.7}$$

  (Equation 5 of Fukugita & Kawasaki 2021; see also Hutter et al. 2021; Muñoz et al. 2021). Because the potential of a halo for a fixed $M_{\rm h}$ becomes shallower in lower redshifts (Barkana & Loeb 2001), the corresponding $T_{\rm vir}$ also becomes lower. Therefore, $M_{\rm h}$ needs to become larger in lower redshifts to compensate for decreasing $T_{\rm vir}$.

- *Stellar feedback.* We can obtain the critical halo mass by equating the energy output of SNe and the energy budget of gas, resulting in the constant circular velocity $V_{\rm cir}$ (e.g., Dayal et al. 2014; Hutter et al. 2021). For a fixed $M_{\rm h}$, the potential is shallower in lower redshifts, and thus $V_{\rm cir}$ is smaller (see also Okamoto et al. 2010). Therefore, we need larger $M_{\rm h}$ to compensate for decreasing $V_{\rm cir}$, which leads to the increasing trend of the critical halo mass $M_{\rm SN,h}$:

  $$M_{\rm SN,h} = 0.93 \times 10^{10} (1+z)^{-1.5}\ M_\odot. \tag{5.8}$$

- *Photoionization.* We adopt the result of Okamoto et al. (2008), who perform a cosmological HD simulation to derive the halo mass $M_{\rm ion,h}$ at which a DMH loses half of its baryon mass due to photoionization by the UVB (see also Castellano et al. 2016; Finlator et al. 2017; Hutter et al. 2021). They found that $M_{\rm ion,h}$

> rapidly increases with cosmic time from $\sim 10^7\ M_\odot$ at $z \sim 9$ to $\sim 10^{10}\ M_\odot$ at $z \sim 0$. This trend is basically because the intensity of the UVB is stronger in lower redshifts (e.g., Bouwens et al. 2015), and thus more massive halos are required to sustain star formation by self-shielding (e.g., Kitayama et al. 2001; Susa & Umemura 2004). Although the UVB intensity decreases at $z < 2$ (e.g., Haardt & Madau 2012), $M_{\rm ion,h}$ continues slowly increasing. This may be because $M_{\rm h}$ should be larger such that $V_{\rm cir}$ is equal to the sound speed of photoionized gas, or, radiative cooling becomes effective.

The redshift evolutions of these critical halo masses ($M_{\rm atom,h}$,$M_{\rm SN,h}$,$M_{\rm ion,h}$) are shown in Figure 5.5. To convert these to the critical stellar masses ($M_{\rm atom,\star}$,$M_{\rm SN,\star}$,$M_{\rm ion,\star}$), we use the SHMRs of Behroozi et al. (2013) extrapolated linearly down to $M_{\rm h} < 10^{10}\ M_\odot$.

We find that $M_{\rm atom,\star}$, $M_{\rm SN,\star}$, and $M_{\rm ion,\star}$ coincidentally agree with one another at $z \sim 0$. Moreover, these values reproduce the observed $M_\star^{\rm T}$ value. These results imply that the turnover in the $z \sim 0$ SMF is attributed either to the insufficient cooling, SN feedback, and/or photoionization by the UVB.

At $z > 6$, our models are well consistent with the semi-analytic model of Yung et al. (2019b), which includes inefficient cooling and stellar wind feedback. Given that $M_\star^{\rm T} = \max(M_{\rm atom,\star}, M_{\rm SN,\star}, M_{\rm ion,\star})$, the models predict that $M_\star^{\rm T} < 10^5\ M_\odot$ at $z > 6$. Therefore, we need to push the current observational limits of the SMFs by $\sim 1-2$ dex to identify $M_\star^{\rm T}$ at high redshifts.

5.2.2 UV LF Turnovers

We compare the faint ends of UV LFs in the top panel of Figure 5.6. At $z \sim 6$, although several previous studies have claimed that UV LFs at $z \sim 6$ potentially show turnovers using the HFF data, the magnification uncertainties of the assumed lens models have made it difficult to draw a firm conclusion. For example, Atek et al. (2018, the blue solid line) claim that $M_{\rm UV}^{\rm T} = -14.93^{+0.61}_{-0.52}$ mag, integrating multiple lens models to estimate the magnification uncertainties. Bouwens et al. (2017b, the cyan dashed line) suggest that $M_{\rm UV}^{\rm T}$ is larger than ~ -15 mag under multiple lens models (see their Table 2 and Figure 8, see also Yue et al. 2018). Meanwhile, Ishigaki et al. (2018, the purple dotted line) do not confirm a turnover down to -14 mag under the `glafic` lens model (Oguri 2010).

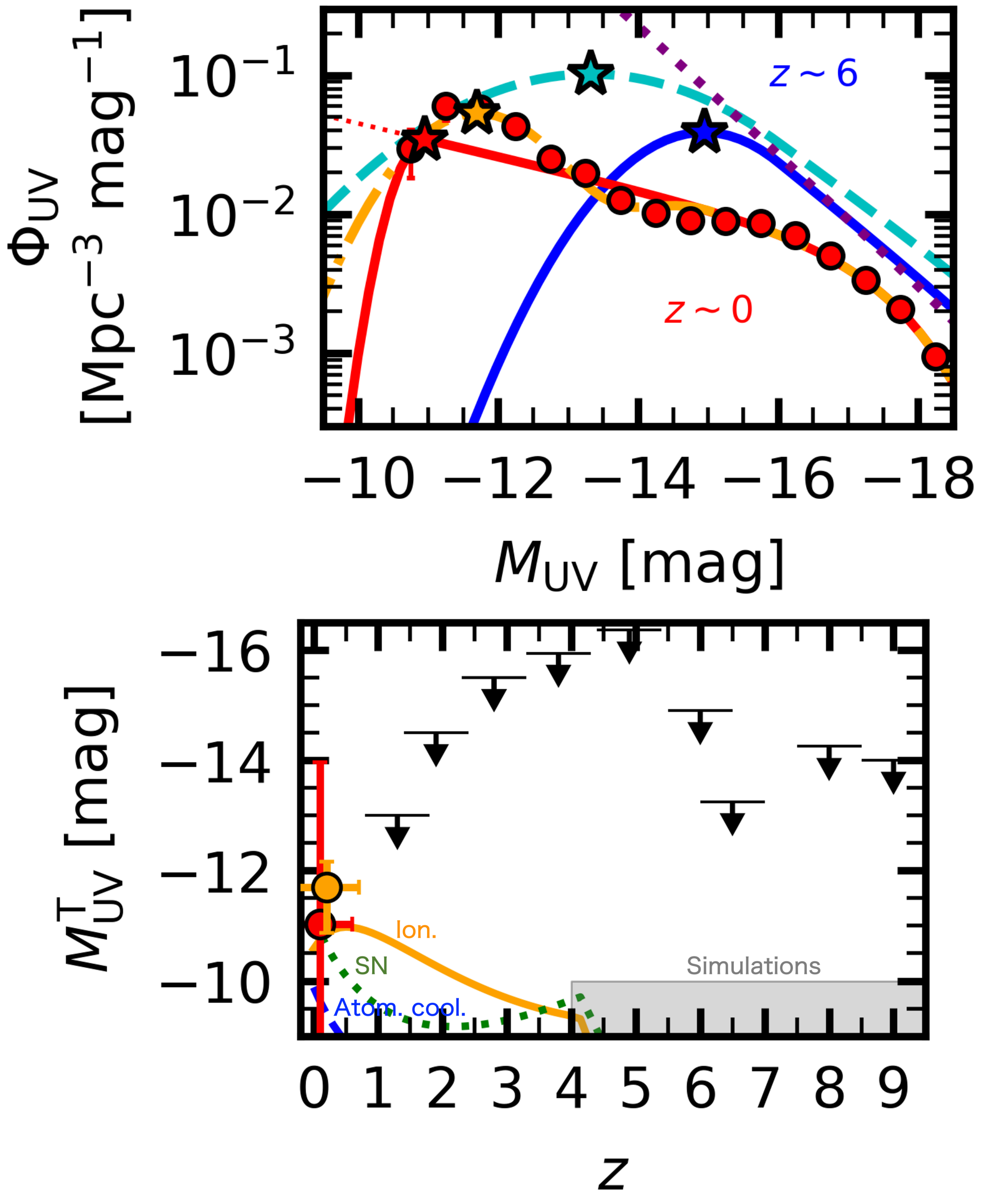

Figure 5.6 **Top:** UV LFs at $z \sim 0$ and 6. The red solid, orange dashed, and red dotted lines show the best-fit truncated, extrapolated, and humped Schechter functions, respectively, at $z \sim 0$. The blue solid, cyan dashed, and purple dotted lines represent the UV LFs taken from Atek et al. (2018), Bouwens et al. (2017b, `CATS` model), and Ishigaki et al. (2018). The stars show the positions of $M_{\rm UV}^{\rm T}$. **Bottom:** Comparison of $M_{\rm UV}^{\rm T}$ at different redshifts. The $z \sim 0$ data point represents our estimation, while the upper limits refer to the faintest $M_{\rm UV}$ limits of the UV LFs (Alavi et al. 2016 for $z \sim 1-2$, Parsa et al. 2016 for $z \sim 3$, Bouwens et al. 2021c for $z \sim 4$, 5, and 6, and Ishigaki et al. (2018) for $z \sim 6-9$). The orange solid, green dotted, and blue dashed lines show the models of the photoionization, SN feedback, and the atomic cooling limit, respectively. The gray shaded area roughly indicates the prediction by multiple numerical studies.

Our UV LF at $z \sim 0$ is presented with the red circles. To estimate the turnover magnitude $M_{\mathrm{UV}}^{\mathrm{T}}$, we fit a truncated Schechter function

$$\Phi_{\mathrm{UV}}(M_{\mathrm{UV}}) = \begin{cases} \hat{\Phi}_{\mathrm{UV,Sch}}(M_{\mathrm{UV}}) & \text{for } M_{\mathrm{UV}} \leq M_{\mathrm{UV}}^{\mathrm{thr}}, \\ \hat{\Phi}_{\mathrm{UV,Sch}}(M_{\mathrm{UV}}) \times 10^{-0.4\gamma_{\mathrm{UV}}(M_{\mathrm{UV}}-M_{\mathrm{UV}}^{\mathrm{thr}})^2} & \text{otherwise,} \end{cases} \tag{5.9}$$

to our UV LF. Here, $M_{\mathrm{UV}}^{\mathrm{thr}}$ and γ_{UV} are free parameters, and $\hat{\Phi}_{\mathrm{UV,Sch}}(M_{\mathrm{UV}})$ is the best-fit Schechter function derived in Section 3.2. We obtain that the best-fit parameter set is $(M_{\mathrm{UV}}^{\mathrm{thr}}, \gamma_{\mathrm{UV}}) = (-11.0^{+11.0}_{-2.9}, 4.26^{+0.74}_{-4.26})$ mag. Defining $M_{\mathrm{UV}}^{\mathrm{T}}$ such that $\frac{\mathrm{d}\Phi_{\mathrm{UV}}}{\mathrm{d}M_{\mathrm{UV}}}|_{M_{\mathrm{UV}}=M_{\mathrm{UV}}^{\mathrm{T}}} = 0$, we obtain that $M_{\mathrm{UV}}^{\mathrm{T}} = -11.0^{+11.0}_{-2.9}$ mag. However, the lack of data points fainter in the faint-end ($M_{\mathrm{UV}} > -11$ mag) prevents us to put a significant constraint on $M_{\mathrm{UV}}^{\mathrm{T}}$.

When we take into account the hump around $M_{\mathrm{UV}} \sim -12$ mag, Equation (5.9) is slightly changed by adding a Gaussian term,

$$\Phi_{\mathrm{UV}}(M_{\mathrm{UV}}) = \Phi_{\mathrm{UV,TruncSch}}(M_{\mathrm{UV}}) + \psi_{\mathrm{UV}} \mathrm{e}^{-\delta_{\mathrm{UV}}(M_{\mathrm{UV}}-M_{\mathrm{UV}}^{\mathrm{T}})^2}, \tag{5.10}$$

following previous studies on optical LFs (e.g., Trentham et al. 2005; Popesso et al. 2006; Bañados et al. 2010; Lee et al. 2016; Yamanoi et al. 2012; Karademir et al. 2022). We term this as a humped Schechter function. Here, $\Phi_{\mathrm{UV,TruncSch}}(M_{\mathrm{UV}})$ is a truncated Schechter function, and ψ_{UV} and δ_{UV} are free parameters. The peak of the Gaussian term is approximately equivalent to $M_{\mathrm{UV}}^{\mathrm{T}}$. We find that the best-fit value is $M_{\mathrm{UV}}^{\mathrm{T}} = -11.70^{+0.83}_{-0.46}$ mag. The best-fit truncated and humped Schechter functions are shown with the red solid and orange dashed lines, respectively. The red and orange stars denote the points where $M_{\mathrm{UV}} = M_{\mathrm{UV}}^{\mathrm{T}}$. Because the values of $M_{\mathrm{UV}}^{\mathrm{T}}$ are comparable both when we assume truncated and humped Schechter functions, the choice of the two $M_{\mathrm{UV}}^{\mathrm{T}}$ values is unlikely to affect the following discussions.

In the bottom panel of Figure 5.6, we compare $M_{\mathrm{UV}}^{\mathrm{T}}$ at different redshifts. The red and orange circles show our estimation assuming truncated and humped Schechter functions, respectively, at $z \sim 0$. At $1 < z < 6$, we use the faintest M_{UV} limits of UV LFs of Alavi et al. (2016), Parsa et al. (2016), and Bouwens et al. (2021c) as the upper limits of $M_{\mathrm{UV}}^{\mathrm{T}}$, because no turnovers are confirmed in their UV LFs. At $z > 6$, the upper limits of $M_{\mathrm{UV}}^{\mathrm{T}}$ obtained by Bouwens et al. (2017b, based on the `CATS` lens model) and Ishigaki et al. (2018) are displayed. Since the constraints at $z > 1$ are too weak, it is impossible to tell the evolutionary trend of $M_{\rm UV}^{\rm T}$ with the current data.

We compare these results with predictions by theoretical studies. First, the blue dashed, green dotted, and orange solid lines represent the $M_{\rm UV}$ values corresponding to $M_{\rm atom,h}$, $M_{\rm SN,h}$, and $M_{\rm ion,h}$, respectively. To convert these halo masses to the critical UV magnitudes ($M_{\rm atom,UV}$, $M_{\rm SN,UV}$, and $M_{\rm ion,UV}$), we use the $M_{\rm UV}$-$M_{\rm h}$ relations of Harikane et al. (2021, see also Harikane et al. 2016, 2018a). We extrapolate their best-fit double power law (DPL; their Equation 54) down to $M_{\rm h} < 10^{11}\ M_\odot$. In the extrapolation, we fit linear functions to their parameters of the DPL versus the redshifts.[1]. We find that both $M_{\rm ion,UV}$ and $M_{\rm SN,UV}$ roughly agree with the observed $M_{\rm UV}^{\rm T}$ at $z \sim 0$ both in the cases for the truncated and humped Schechter functions. The value of $M_{\rm cool,UV}$ may fall slightly below our $M_{\rm UV}^{\rm T}$. These results may imply that the UV LF turnovers are controlled mainly by photoionization and/or SN feedback, while the contribution of insufficient cooling cannot also be ruled out. However, we should be cautious that the values of $M_{\rm atom,UV}$, $M_{\rm SN,UV}$, and $M_{\rm ion,UV}$ are very subject to the assumed $M_{\rm UV}$-$M_{\rm h}$ relations. The relations are not constrained at the magnitude range considered here, which prevents the conclusion.

At $z > 4$, multiple theoretical studies predict turnovers around -10 to -8 mag, which is shown with the gray box (e.g., Cai et al. 2014; O'Shea et al. 2015; Castellano et al. 2016; Gnedin 2016; Liu et al. 2016; Park et al. 2019; Yung et al. 2019a, 2020; Ocvirk et al. 2020; Qin et al. 2021). Because the current observations are limited to $M_{\rm UV} < -14$ mag, we need much deeper observations such that we can reach > 4 mag fainter magnitudes in UV LFs than the current observational limits to identify turnovers.

---

[1] We individually fit the relations at $z < 4$ and $z > 4$, because the parameters show different redshift evolutionary trends before and after $z \sim 4$.

5.3 Size-Mass Relations

One of the key properties of a galaxy is its morphology (or size; e.g., Shibuya et al. 2015, 2019; Kawamata et al. 2018).

At high redshifts, in particular, because the size of a galaxy is one of the very few pieces of the galaxy properties available with photometric observations, it is worth investigating the sizes of the low-mass galaxies. In the context of galaxy formation, the size of a galaxy determines the depth of its potential wall, and then affects how the galaxy is susceptible to feedback. This motivates us to investigate the relations between the effective radii R_{e} and $M_\star$ of our $z \sim 6-9$ dropouts. Size measurements of low-mass galaxies, which are likely to be compact, are helped by the high resolving power of the HST. Additionally, a lensed galaxy is stretched along critical curves, allowing the structures to be studied at high spatial resolution.

The values of R_{e} are taken from Kawamata et al. (2018), who obtain the best-fit value by fitting ellipsoidal Sérsic profiles to the observed profiles corrected for the lensing effect. We estimate $M_\star$ of the dropouts by multiplying the best-fit $M_\star$-M_{UV} relations (Figure 2.6) to the observed M_{UV} values. If M_{UV} is outside of the range where the best-fit $M_\star$-M_{UV} relations hold, then we use the extrapolated best-fit relations to derive $M_\star$. The uncertainties of the $M_\star$-M_{UV} relations propagate to those of $M_\star$.

We plot the R_{e}-$M_\star$ relations of our $z \sim 6-9$ dropouts with the yellow to red circles in Figure 5.7. We compare the R_{e}-$M_\star$ distributions with those of the stellar systems in the local universe (Norris et al. 2014 and the references therein). Surprisingly, we find that part of our dropouts have small R_{e} and $M_\star$ values comparable to local globular clusters (GCs) and ultra-compact dwarfs (UCDs; blue diamonds). In particular, the R_{e} and $M_\star$ values of four of our $z \sim 6-7$ dropouts, HFF2C-1181-3480, HFF4C-3595-4157, HFF5C-4260-1364, and HFF5C-4039-1566, are equal to or less than 40 pc and 10^7 $M_\odot$, respectively, which are comparable to the Milky Way GCs (e.g. Pal 5, Pal 14, and NGC 5139; Baumgardt & Hilker 2018). We here term these dropouts as "tiny" sources. The values of R_{e} and $M_\star$ of these tiny sources are listed in Table 5.1.

We test our estimation against the magnification uncertainties. In Figure 5.8, we show the differences of the magnification factors at the positions of the tiny sources among lens models. Here, μ_{m} and μ_{glafic} denote the magnification factors derived with a given lens model m and `glafic`, respectively. We use ten independent lens

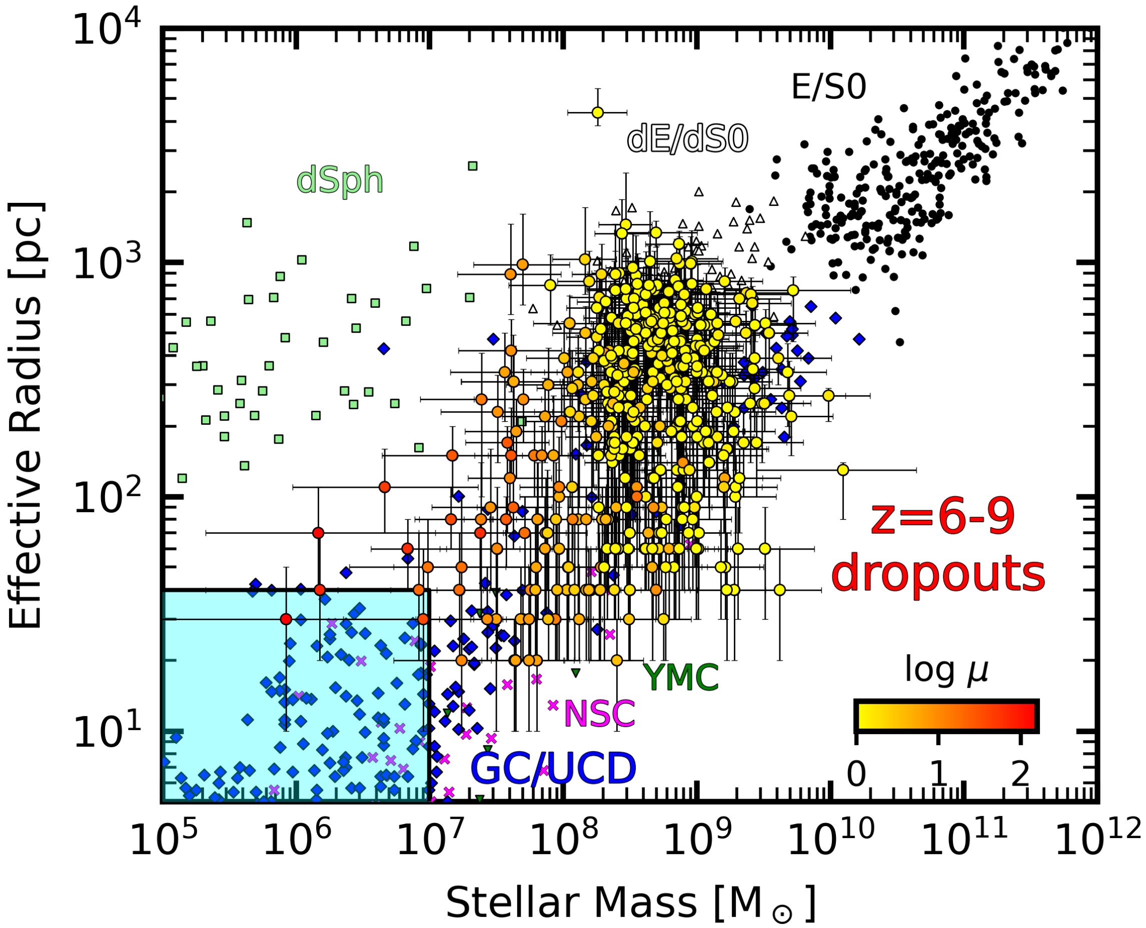

Figure 5.7 Distributions of R_e versus $M_\star$. Our $z \sim 6-9$ dropouts are presented with the large circles whose colors indicate their magnification factors. The other symbols show the distributions of the local elliptical/S0 galaxies (E/S0s; black circles), dwarf elliptical/S0 galaxies (dEs/dS0s; gray triangles), dwarf spheroids (dSphs; light-green squares), nuclear star clusters (NSCs; orange crosses), young massive clusters (YMCs; green down-pointing triangles), and GCs/UCDs (blue hexagons) obtained by Norris et al. (2014) and the references therein. The cyan shade represents the region where the Milky Way GCs are located.

models from `glafic`, `CATS` (v2 for M0416C, v1 for M1149C and A1063C), Sharon & Johnson (`Lenstool`; v2.1 for M1149C, v2 for M0416C and A1063C), Zitrin-NFW (v3 for M0416C, v1 for A1063C), Zitrin-LTM (v1 for the three clusters), Zitrn-LTM-Gauss (v3 for M0416C, v1 for M1149C and A1063C), Williams (`GRALE`; v3.1 for M0416C, v1 for M1140C and A1063C), Bradač & Hoag (v1 for the three clusters), Diego (`WSLAP+`; v3 for M0416C), and Merten (`SaWLens`; v1 for the three clusters).[2] We confirm that the magnification factors are broadly consistent among most of the models for HFF2C-1181-3480, HFF5C-4260-1364, and HFF5C-4039-1566. These results support our estimation that they have very compact sizes and low masses. We note that, in the second panel, half of the models implies μ smaller than $\mu_{\rm glafic}$ at $> 1\sigma$, so we cannot rule out the possibility that HFF4C-3595-4157 have larger $R_{\rm e}$ and $M_\star$ values than our estimation.

Similarly to our work, Bouwens et al. (2017a) use the HFF data to investigate the $R_{\rm e}$-$M_\star$ relations of $z \sim 6-8$ galaxies. They also report that part of their galaxies have $R_{\rm e}$ and $M_\star$ comparable to those of local GCs, super star complexes, and star-cluster complexes in the local universe (see also Bouwens et al. 2021a,b). However, they *assume* $M_\star$-$M_{\rm UV}$ relations to estimate $M_\star$, while we provide observational (*not* assumed) values of $M_\star$. The assumption of Bouwens et al. (2017a) is shown with the blue dashed and dotted line in Figure 2.6. They use the latter model (100-Myr star formation duration) to convert $M_{\rm UV}$ to $M_\star$. We find that our $M_\star$-$M_{\rm UV}$ relations follow the latter model, which now confirms their assumption.

Indeed, M0416I-6118103480 of Bouwens et al. (2017a) is also selected in our sample (HFF2C-1181-3480). Their estimation is $M_{\rm UV} = -15.0^{+1.3}_{-1.0}$, $\mu = 33.6^{+81.6}_{-19.9}$, and $R_{\rm e} = 16^{+29}_{-13}$, all of which agree with ours. The number of tiny sources is larger in Bouwens et al. (2017a) sample than in ours, probably due to magnification uncertainties and/or the different definition of tiny sources. We select the tiny sources meeting both $R_{\rm e} \leq 40$ and $M_\star \leq 10^7\ M_\odot$, while the definition in Bouwens et al. (2017a) is only $R_{\rm e} \leq 40$.

As a reference, the number of our tiny sources increases from four to 13 when we include the dropouts whose 1σ lower limits of $R_{\rm e}$ and $M_\star$ meet the definition. For example, our HFF2C-1156-3446 ($M_{\rm UV} = -16.15 \pm 0.09$) is estimated to have

---

[2] See `https://archive.stsci.edu/prepds/frontier/lensmodels/` for the details of these models.

Table 5.1 Catalog of our tiny sources.

ID	2C-1181-3480	4C-3595-4157	5C-4260-1364	5C-4039-1566
R.A.	64.049226	177.399818	342.177526	342.168321
decl.	-24.063349	$+22.404384$	-44.526786	-44.532412
$M_{\rm UV}$ [mag]	-15.59 ± 0.08	-13.45 ± 0.14	-15.52 ± 0.18	-13.98 ± 0.17
$M_\star$ [10^6 $M_\odot$]	$9.0^{+26.4}_{-6.7}$	$0.84^{+7.0}_{-0.75}$	$8.3^{+25.3}_{-6.3}$	$1.5^{+9.8}_{-1.3}$
$R_{\rm e}$ [pc]	30^{+30}_{-20}	30^{+20}_{-20}	40^{+30}_{-20}	40^{+30}_{-20}
${\mu_{\rm best}}^*$	5.85	157.63	19.12	77.69

$*$ Best-fit magnification factor.

$R_{\rm e} = 40^{+30}_{-20}$ pc and $M_\star = 1.7^{+3.7}_{-1.2} \times 10^7\ M_\odot$. This dropout is also reported as a tiny source M0416I-6115434445 in Bouwens et al. (2017a), and as a compact star-forming region GC1 in Vanzella et al. (2017). The values of $R_{\rm e}$ and $M_\star$ estimated in Bouwens et al. (2017a), Vanzella et al. (2017), and our work are broadly consistent within the $\sim (1-2)\sigma$ uncertainties.

5.4 Physical Origins of Extended Lyα Emission

In this Section, we investigate the mechanism of extended Lyα emission production. A production process is a combination of 1) where Lyα photons originate; 2) how Lyα photons are produced; and 3) how these photons transfer in the surrounding materials (see also Section 1.3.2).

1) We distinguish Lyα emission according to where it originates from: i) the ISM of the targeted galaxy (*central galaxy*), ii) the *CGM* surrounding the central galaxy, iii) *satellite galaxies*, or iv) *other halos*. Other halos refer to halos of dwarf galaxies that are $> R_{\rm vir}$ away from the central galaxy; i.e., we distinguish satellite galaxies and other halos in that the former and latter lie inside and outside the $R_{\rm vir}$ of the DMH, respectively.

2) We consider that Lyα photons are produced in the processes of *recombination* or *collisional excitation* (*cooling radiation*).

3) We distinguish whether models take into account the scattering process or not. This discrimination is motivated by the fact that an observed SB profile depends on radiative transfer (Byrohl et al. 2021).

In Figure 5.9, we compare the observed $\mathrm{SB}_{\mathrm{Ly}\alpha}$ profiles and those predicted by theoretical work. The observational results are taken from Section 4.3.3: Momose et al. (2016, $L_{\mathrm{Ly}\alpha} = 10^{42.6}$ erg s^{-1} subsample at $z = 2.2$), Wisotzki et al. (2018, $L_{\mathrm{Ly}\alpha} > 10^{42}$ erg s^{-1} subsample at $z = 3-4$), Momose et al. (2014, $z = 5.7$ and 6.6 LAEs), and our *all* samples ($z = 2.2-6.6$). Predicted profiles are taken from Zheng et al. (2011), Dijkstra & Kramer (2012), Lake et al. (2015), Mas-Ribas et al. (2017b), Kakiichi & Dijkstra (2018), and Byrohl et al. (2021), which are summarized in Table 5.2. We plot these observational and theoretical results at the nearest redshifts among

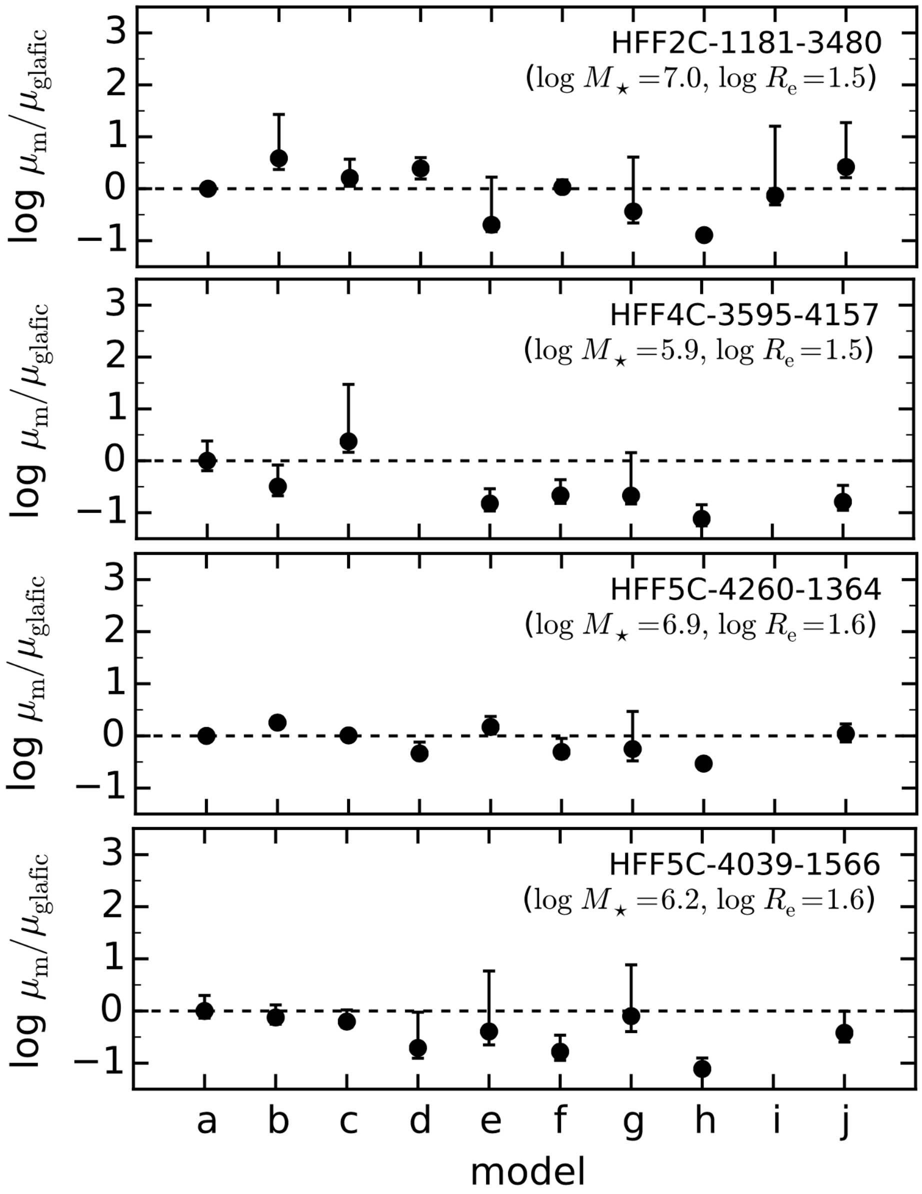

Figure 5.8 Comparison of the magnification factors at the positions of the tiny sources between the lens model m ($\mu_{\rm m}$) and `glafic` ($\mu_{\rm glafic}$). The horizontal axes show models: a) `glafic` (this work), b) `CATS`, c) Sharon, d) Zitrin-NFW, e) Zitrin-LTM, f) Zitrin-NFW-Gauss, g) Williams, h) Bradač, i) Diego, j) Merten. At the upper right corner of each panel lists the ID and the estimation of $M_\star$ and $R_{\rm e}$ with `glafic`. We note that $\log(R_{\rm e}/{\rm pc}) = 1.6$ when $R_{\rm e} = 40$ pc.

$z = 2.2$, 3.3, 5.7, and 6.6, except that the model of Mas-Ribas et al. (2017b) is presented at all the redshifts, with the correction for the cosmological dimming effect. We normalize all the profiles such that they match at $r = 1''$ in amplitude for precise comparison under the same Lyα luminosity of the central galaxy (the profiles of Zheng et al. 2011, Lake et al. 2015 and Byrohl et al. 2021 are normalized after summing up those of the different origins). We compare these observational and theoretical results in the context of the Lyα photon origins in the following subsections. While our data points are mainly outside $R_{\rm vir}$, below we discuss the physical origins both inside and outside $R_{\rm vir}$ based on the observed profiles of the literature and ours.

5.4.1 Central Galaxy

To discuss the contribution from the *central galaxy*, we compare the models of Zheng et al. (2011), Dijkstra & Kramer (2012), Lake et al. (2015), Kakiichi & Dijkstra (2018), and Byrohl et al. (2021). They applied Lyα radiative transfer modeling to cosmological HD galaxy formation simulations at $z = 5.7$, 3.1, $2-3$, and $2-5$, respectively, to investigate Lyα photons produced by SF in the central galaxy and resonantly scattered into the CGM. We take the "one-halo" term model from Zheng et al. (2011), where Lyα photons are scattered not only in the CGM but also in the IGM. The model of Lake et al. (2015) takes into account the contribution from cooling radiation in addition to that from SF. The model of Kakiichi & Dijkstra (2018) is taken in an approximated form of their Equation (28). The model of Byrohl et al. (2021) considers recombination caused by ionizing photons from SF and UVB as well as cooling via collisional de-excitation.

The black lines in Figure 5.9 represent the contribution from the central galaxy: Kakiichi & Dijkstra (2018, dotted, $z = 2.2$), Byrohl et al. (2021, solid, $z = 3.3$), Lake et al. (2015, dash-dotted, $z = 3.3$), Dijkstra & Kramer (2012, dotted, $z = 3.3$), and Zheng et al. (2011, dotted, $z = 5.7$). These models successfully reproduce the observed $\mathrm{SB}_{\mathrm{Ly}\alpha}$ profiles inside the CGM ($r < R_{\rm vir}$) at $z = 3.3$ and 5.7, implying resonant scattering as a major source powering Lyα emission. This finding is also supported by previous studies in other aspects, such as halo properties (e.g., a halo luminosity-mass relation; Kusakabe et al. 2019) and kinematics (e.g., a correlation between the peak velocity shift and the width of a Lyα line, Leclercq et al. 2020; red peak dominated Lyα spectra, Chen et al. 2021).

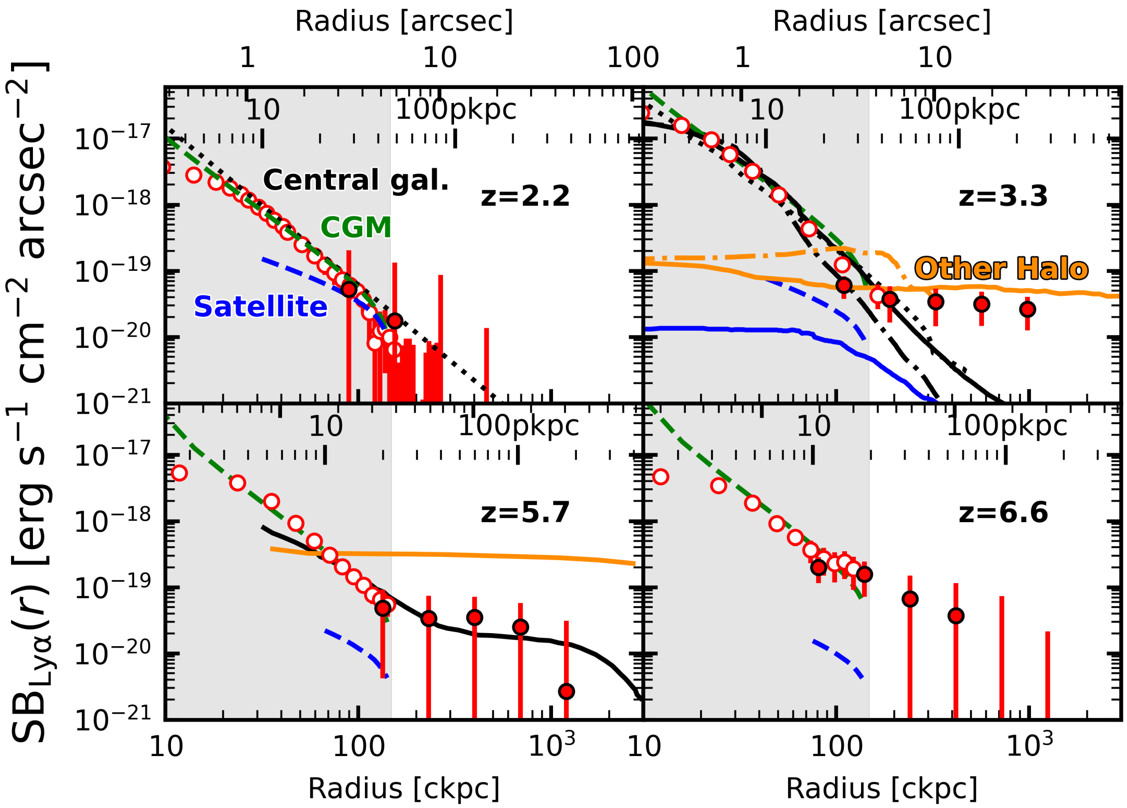

Figure 5.9 Comparison of the $\mathrm{SB}_{\mathrm{Ly}\alpha}$ radial profiles between the observational and theoretical studies at $z = 2.2$ (top left), 3.3 (top right), 5.7 (bottom left), and 6.6 (bottom right). The filled red circles depict the observational results taken from our *all* sample ($z = 2.2 - 6.6$), while the open red circles show the results from previous observational work (Momose et al. 2016 at $z = 2.2$, Wisotzki et al. 2018 at $z = 3.3$, and Momose et al. 2014 at $z = 5.7$ and 6.6). The $\mathrm{SB}_{\mathrm{Ly}\alpha}$ amplitude of Wisotzki et al. (2018) is normalized such that L_{Lya} in $r \leq 1''$ matches to that of our *all* sample (see Section 4.3.4). We represent the theoretical work with the lines, whose colors indicate the Lyα emission originations: the central galaxy (black), CGM (green), satellite galaxies (blue), and other halos (orange). The models are taken from Mas-Ribas et al. (2017b, green and blue dashed lines at $z = 2.2$, 3.3, 5.7, 6.6), Kakiichi & Dijkstra (2018, black dotted line at $z = 2.2$), Byrohl et al. (2021, black, blue, and orange solid lines at $z = 3.3$), Lake et al. (2015, black and orange dash-dotted lines at $z = 3.3$), Dijkstra & Kramer (2012, black dotted line at $z = 3.3$), and Zheng et al. (2011, black and orange solid lines at $z = 5.7$). See Table 5.2 for details of these models. We normalize the $\mathrm{SB}_{\mathrm{Ly}\alpha}$ profiles from the model predictions such that the central galaxy ($r \leq 1''$) has the $L_{\mathrm{Ly}\alpha}$ value similar to that observed at each redshift. The gray shades illustrate the regions inside R_{vir} of a DMH with $M_{\mathrm{h}} = 10^{11}\ M_{\odot}$.

Table 5.2 Summary of the theoretical studies used for comparison.

Reference	$z_{\rm model}$	$z_{\rm plot}$	Origin	Process	Scattering	$M_{\rm h}$ $[M_\odot]$
Mas-Ribas et al. (2017b)	5.7, 6.6	2.2, 3.3, 5.7, 6.6	CGM/Sat.	Rec.	n	10^{11} *
Kakiichi & Dijkstra (2018)	$2-3$	2.2	Cen.	Rec.	y	$\sim 10^{12}$
Byrohl et al. (2021)	$2-5$	3.3	Cen./Sat./Other.	Rec./Cool.	y	$\sim 10^{11}$ #
Dijkstra & Kramer (2012)	~ 2.65	3.3	Cen.	Rec.	y	—
Lake et al. (2015)	3.1	3.3	Cen./Other.	Rec./Cool.	y	$10^{11.5}$
Zheng et al. (2011)	5.7	5.7	Cen./Other.	Rec.	y	$10^{11.2}$

Columns: (1) Reference. (2) Redshift assumed in the model. (3) Redshift where we plot the model in Figure 5.9. (4) Origins of Lyα photons (where Lyα photons are produced): the central galaxy (Cen.), CGM, satellite galaxies (Sat.), and other halos (Other.). (5) Physical processes of Lyα emission production (how Lyα emission is produced): recombination (Rec.), and cooling radiation (Cool.). (6) Whether the model takes into account Lyα radiative transfer (i.e., resonant scattering) or not. (7) Assumed halo mass.

* We fix $M_{\rm h}$ to 10^{11} $M_\odot$, while $M_{\rm h}$ is a free parameter in the model.

This value was converted from the assumed $M_\star$ of $10^{8.5} - 10^{9.5}$ $M_\odot$ with the SHMR of Behroozi et al. (2019).

The one-halo term of Zheng et al. (2011) reproduces the observed $\mathrm{SB}_{\mathrm{Ly}\alpha}$ profile also from $r \sim R_{\mathrm{vir}}$ up to ~ 1 cMpc at $z = 5.7$. They considered resonant scattering in the IGM in addition to the CGM. This effect leads to a plateau-like feature in the $\mathrm{SB}_{\mathrm{Ly}\alpha}$ profile at $r \sim 0.3 - 1$ cMpc (see also Jeeson-Daniel et al. 2012), which is similar to those at $z = 3.3$ and 5.7. Therefore, we may interpret that the observed extended Lyα emission outside the CGM is produced by resonant scattering in the IGM, although the uncertainties are large. At $z = 3.3$, however, the models adopted here (Lake et al. 2015, Dijkstra & Kramer 2012, and Byrohl et al. 2021) produce values lying far below the observed $\mathrm{SB}_{\mathrm{Ly}\alpha}$ profile beyond 300 ckpc and do not reproduce a plateau-like shape, unlike the one-halo term of Zheng et al. (2011). One possibility is that the contribution from the central galaxy decreases from $z = 5.7$ to 3.3, but there is no evidence to confirm this. Alternatively, we suppose that this discrepancy can be attributed to the different assumptions and incorporated physics in the models, such as treatment of stellar radiation, dust, and scattering, especially beyond R_{vir}. Nevertheless, since the one-halo term of Zheng et al. (2011) reproduces the observed $\mathrm{SB}_{\mathrm{Ly}\alpha}$ profile at $z = 5.7$, we cannot rule out the possibility that scattered Lyα photons originating from the central galaxy contribute to extended Lyα emission beyond R_{vir}. We need additional inputs on the neutral hydrogen gas distribution outside R_{vir} to further determine the contribution of resonant scattering.

The assumptions on M_{h} values are unlikely to affect our discussion here, because the models above use roughly similar M_{h} values: $10^{11.2}$ and $10^{11.5}$ $M_{\odot}$ for Zheng et al. (2011) and Lake et al. (2015), respectively. Byrohl et al. (2021) assume a stellar mass $M_{\star}$ range of $10^{8.5} - 10^{9.5}$ $M_{\odot}$ at $z = 3$, which corresponds to $M_{\mathrm{h}} \sim 10^{11}$ $M_{\odot}$ given the $M_{\star}/M_{\mathrm{h}}$ ratio obtained in Behroozi et al. (2019, see also Kusakabe et al. 2018). These values are similar to those obtained in the previous observations (e.g., Ouchi et al. 2010; Kusakabe et al. 2018).

5.4.2 CGM

We next use the model from Mas-Ribas et al. (2017b) to investigate the Lyα emission produced in the *CGM*. They constructed an analytical model of fluorescent emission in the CGM caused by ionizing radiation from SF in the central galaxy at $z = 5.7$ and 6.6 (we apply this model also to $z = 3.3$ and 2.2; see also Mas-Ribas & Dijkstra 2016). The model of Mas-Ribas et al. (2017b) includes three free parameters: 1) the CGM structure, 2) SF rate (SFR), and 3) radius $R_{\rm max}$. 1) We adopt the simplified clumpy outflow model of Steidel et al. (2010) as the CGM structure (the choice here has only a small impact on $\mathrm{SB}_{\mathrm{Ly}\alpha}$ profiles; see Figure 2 of Mas-Ribas & Dijkstra 2016). 2) We normalize the model with SFR $= 1$, 10, 10, and 20 $M_\odot$ yr^{-1} at $z = 2.2$, 3.3, 5.7, 6.6, respectively. 3) $\mathrm{SB}_{\mathrm{Ly}\alpha}(b)$ is derived as the integration of Lyα emissivity at radius r over $b \leq r \leq R_{\rm max}$, where b denotes the impact parameter (see Equations 4 and 2 of Mas-Ribas & Dijkstra 2016 and Mas-Ribas et al. 2017b, respectively). Here $R_{\rm max}$ represents the extent to which Lyα emission contributes to $\mathrm{SB}_{\mathrm{Ly}\alpha}$. We assume that $R_{\rm max}$ is equivalent to $R_{\rm vir}$ for a DMH of $M_{\rm h} = 10^{11}$ $M_\odot$ ($=46$, 34, 22, and 20 pkpc at $z = 2.2$, 3.3, 5.7, and 6.6, respectively). Their model ignores the effect of resonant scattering.

The green dashed lines in Figure 5.9 represent the model of Mas-Ribas et al. (2017b). The $\mathrm{SB}_{\mathrm{Ly}\alpha}$ profiles predicted by their model are in good agreement with those observed inside $R_{\rm vir}$ at all the redshifts. However, because $\mathrm{SB}_{\mathrm{Ly}\alpha}$ profiles drop sharply at $r = R_{\rm max}$ according to this model, the emission originating from the CGM cannot contribute to extended emission beyond $R_{\rm vir}$. Mas-Ribas & Dijkstra (2016) and Mas-Ribas et al. (2017b) arbitrarily adopted much larger $R_{\rm max}$ values (> 100 pkpc) to reproduce the profiles obtained in Momose et al. (2014), bust such large $R_{\rm max}$ values correspond to $M_{\rm h} > 10^{12}$ $M_\odot$, which is much larger than those observed (e.g., Ouchi et al. 2010; Kusakabe et al. 2018). If $R_{\rm max}$ is larger than $R_{\rm vir}$, materials should exist outside the CGM ($\gtrsim 3$ times larger scales than $R_{\rm vir}$) and produce fluorescent emission contributing to extended Lyα emission. In either case, the observed $\mathrm{SB}_{\mathrm{Ly}\alpha}$ profiles beyond 300 cpkc at $z = 3.3$ cannot be reproduced even with larger values of $R_{\rm max}$.

Overall, fluorescence in the CGM can power Lyα emission inside $R_{\rm vir}$ according to the model of Mas-Ribas et al. (2017b), while it plays only a marginal role beyond $R_{\rm vir}$. This behavior was also suggested by MUSE UDF data (Gallego et al. 2018; Bacon et al. 2021). We note that the model of Mas-Ribas et al. (2017b) ignores the scattering effect, which leads to a sharp drop of $\mathrm{SB}_{\mathrm{Ly}\alpha}$ at $r = R_{\rm max}$. Hence, it is necessary to incorporate resonant scattering to extend Lyα emission when we rely on the CGM fluorescence scenario.

The contribution from cooling radiation in the CGM remains unclear. Byrohl et al. (2021) argued that cooling radiation dominates ~ 30 % of the total Lyα emission at $r \gtrsim 20$ pkpc. On the other hand, Rosdahl & Blaizot (2012) found that Lyα emission from cooling radiation is centrally ($r < 10$ pkpc) concentrated for a DMH with $M_{\rm h} = 10^{11}\ M_{\odot}$. We need additional models at larger scales to further discuss whether cooling radiation contributes to extended Lyα emission or not.

5.4.3 Satellite Galaxies

We adopt another model from Mas-Ribas et al. (2017b), which predicts the contribution from SF in *satellite galaxies* (see also Mas-Ribas et al. 2017a). There are three free parameters in their model: 1) a clustering description, 2) Lyα escape fraction ($f^{\rm esc}_{\rm Lya}$), and 3) $R_{\rm max}$. 1) We assume that clustering follows a power-law two-point cross-correlation function $\xi(r)$ of $\xi(r) = (r/r_0)^{-\alpha}$ with the scale length $r_0 = 4$ cMpc and index $\alpha = 1.8$ (e.g., Ouchi et al. 2010; Harikane et al. 2016; Bielby et al. 2017). 2) We fix $f^{\rm esc}_{\rm Lya}$ to 0.4, while ${\rm SB}_{{\rm Ly}\alpha}$ linearly depends on $f^{\rm esc}_{\rm Lya}$. 3) Satellite galaxies are assumed to exist from $r = 10$ pkpc to $R_{\rm max}$, which we assume is equal to $R_{\rm vir}$ in the same way as for the fluorescence model (Section 5.4.2). We additionally take the "outer halo" model from Byrohl et al. (2021).

The blue dashed and solid lines represent the models of Mas-Ribas et al. (2017b) and Byrohl et al. (2021), respectively. We find that the contribution from satellite galaxies are negligible compared to the other contributions, except at $r \sim 100$ ckpc at $z = 2.2$. While we choose a power-low correlation function to describe the clustering, other choices, such as the Navarro-Frenk-White (NFW) profile (Navarro et al. 1997), reduce the ${\rm SB}_{{\rm Ly}\alpha}$ values at $r > 40$ ckpc (see the left panel of Figure 2 of Mas-Ribas et al. 2017a). When a power-law correlation function is assumed, larger r_0 values increase the overall profiles. However, unrealistically large values of r_0 and $R_{\rm max}$ are necessary to reproduce extended Lyα emission beyond $R_{\rm vir}$ with satellite galaxies alone. Additionally, the model overpredicts the observed ${\rm SB}_{{\rm cont},\nu}$ values when the model is tuned to reproduce the observed ${\rm SB}_{{\rm Ly}\alpha}$ profiles (Mas-Ribas et al. 2017a).

For these reasons, we conclude that satellite galaxies are unlikely to contribute to extended Lyα emission beyond $R_{\rm vir}$. This conclusion is supported by the fact that emission is more extended in Lyα than in UV continuum (Section 4.3.3; see also Momose et al. 2014, 2016; Wu et al. 2020), because the ${\rm SB}_{{\rm cont},\nu}$ profiles should be extended similarly as the ${\rm SB}_{{\rm Ly}\alpha}$ profiles if satellite galaxies contribute to ${\rm SB}_{{\rm Ly}\alpha}$.

5.4.4 Other Halos

Lastly, we compare the models for *other halos* taken from Zheng et al. (2011), Lake et al. (2015), and Byrohl et al. (2021). From Lake et al. (2015) we specifically adopt the model in which Lyα emission originates from 'knots,' the regions with high Lyα emissivity around the central galaxy. The 'two-halo' term model is taken from Zheng et al. (2011).

We show these models with the orange lines in Figure 5.9: Byrohl et al. (2021, solid, $z = 3.3$), Lake et al. (2015, dash-dotted, $z = 3.3$), and Zheng et al. (2011, solid, $z = 5.7$). At $z = 3.3$, the contribution from other halos predicted by Byrohl et al. (2021) agrees with the observed $\mathrm{SB}_{\mathrm{Ly}\alpha}$ profiles within the 1σ uncertainties. Although the knots model of Lake et al. (2015) is limited to $r \lesssim 300$ cpkc, it roughly reproduces the observed profiles at $r \sim (200 - 300)$ ckpc. On the other hand, the two-halo term of Zheng et al. (2011) at $z = 5.7$ significantly overestimates the $\mathrm{SB}_{\mathrm{Ly}\alpha}$ values beyond 100 ckpc. The amplitudes of the models of Zheng et al. (2011) and Byrohl et al. (2021) differ by ~ 1 dex, similarly as we found in Section 5.4.1.

Kakuma et al. (2021) argue that the difference is caused because they masked out bright objects. However, this interpretation is not necessarily appropriate, since the profile of Byrohl et al. (2021) has an amplitude similar to (or rather slightly higher than) profiles observed at $z = 3.3$. The two-halo term of Zheng et al. (2011) also overpredicts the $\mathrm{SB}_{\mathrm{Ly}\alpha}$ values of Momose et al. (2014). Nevertheless, we cannot rule out the possibility that other halos contribute to extended Lyα emission beyond R_{vir}, since the model of Byrohl et al. (2021) agrees with the observed $\mathrm{SB}_{\mathrm{Ly}\alpha}$ profiles. This suggestion is consistent with Bacon et al. (2021), who identified very extended (> 300 arcsec^2 or $> 2 \times 10^4$ pkpc^2) Lyα emission at $z \sim 3$ using MUSE data; they found that 70 % of the total Lyα luminosity originates from filamentary structures beyond the CGM. They argued that the extended Lyα emission can be reproduced by a population of extremely faint ($< 10^{40}$ erg s^{-1}) galaxies under certain conditions, which correspond to other halos considered in this subsection.

We note that the $\mathrm{SB}_{\mathrm{Ly}\alpha}$ profile of our *all* sample at $z = 5.7$ is larger in the UD-COSMOS field than that averaged over the UD-COSMOS and UD-SXDS fields. This results in a smaller amplitude gap between the two-halo term of Zheng et al. (2011) and our profile. However, our profile based solely on the UD-COSMOS field disagrees with those from the previous observational studies. Thus the averaged profile is more appropriate for comparison against the models.

5.4.5 Overall Interpretation

In summary, $\mathrm{SB}_{\mathrm{Ly}\alpha}$ profiles inside the CGM ($< R_{\mathrm{vir}}$) are possibly explained either by scattered Lyα emission originating from the central galaxy and/or fluorescent emission in the CGM. Meanwhile, extended Lyα emission beyond R_{vir} is possibly powered either by resonant scattering at large scales and/or contributed from other halos. Fluorescence in the CGM and satellite galaxies are not sufficient to reproduce the observed $\mathrm{SB}_{\mathrm{Ly}\alpha}$ profiles beyond R_{vir}.

We note that the processes and origins of Lyα emission may differ among LAEs. They may also vary according to the radius and redshift even when we focus on averaged profiles around different LAEs. However, our systematic investigation of extended Lyα emission at $z = 2 - 7$ is advantageous for a comprehensive understanding of the processes and origins of extended Lyα emission.

More simulations focusing on large scales will help to distinguish the processes and origins. On the observational side, applying the intensity mapping technique to multiple lines, such as Hα and [O III], will help to distinguish physical processes and origins of extended Lyα emission, because they trace different components (see Figures 6 and 12 of Mas-Ribas et al. 2017a and Fujimoto et al. 2019). These emission lines will be observed with next-generation facilities, such as the *James-Webb* Space Telescope (JWST), the *Nancy Grace Roman* Space Telescope (NGRST), and Spectro-Photometer for the History of the Universe, Epoch of Reionization and Ices Explorer (SPHEREx).

5.5 Overview of Galaxy Formation

5.5.1 Physical Processes of Low-Mass Galaxy Formation

Before closing this Chapter, we summarize the results obtained in this thesis, and overview populations, formation processes, and redshift evolution of the galaxies in the aspects of SMFs, UV LFs, and Lyα emission.

Figure 5.10 (5.11) compares the SMFs (UV LFs) at $z \sim 6$ and ~ 0. At $z \sim 0$, we use our best-fit truncated Schechter SMF and UV LF that are obtained in Section

5.2. At $z \sim 6$, no clear turnovers have yet to be observationally identified. We thus assume that $M_\star^{\mathrm{T}} = 10^{4.7}\ M_\odot$ and $M_{\mathrm{UV}}^{\mathrm{T}} = -9$ mag at $z \sim 6$ based on the theoretical predictions (see Figures 5.4 and 5.6, respectively), and fix $\gamma_\star$ and γ_{UV} to those at $z \sim 0$.

We suggest that there are three key $M_\star$ and M_{UV} ranges in galaxy formation, which are presented with the gray arrows.

- *Low-mass (faint) end:* $M_\star \lesssim M_\star^{\mathrm{T}}$ and $M_{\mathrm{UV}} \gtrsim M_{\mathrm{UV}}^{\mathrm{T}}$. The turnovers are observed with the possible increasing trends of $M_\star^{\mathrm{T}}$ and $M_{\mathrm{UV}}^{\mathrm{T}}$ toward low redshifts. The values of $M_\star^{\mathrm{T}}$ and $M_{\mathrm{UV}}^{\mathrm{T}}$ reflect the photoionization by the UVB, SN feedback, and/or the atomic gas cooling limit. The SMFs and UV LFs just rightward of the turnovers are steep at high redshifts and flat at low redshifts, which implies the hierarchical galaxy formation.

- *Low-mass (faint) regime:* $M_\star^{\mathrm{T}} \lesssim M_\star \lesssim M_\star^*$ and $M_{\mathrm{UV}}^{\mathrm{T}} \gtrsim M_{\mathrm{UV}} \gtrsim M_{\mathrm{UV}}^*$. The SMFs and UV LFs in these regimes are flatter than the HMFs particularly at low redshifts. This feature is attributed to SN feedback.

- *Massive (bright) end:* $M_\star \gtrsim M_\star^*$ and $M_{\mathrm{UV}} \lesssim M_{\mathrm{UV}}^*$. Low-mass galaxies grow to be massive through merging events until the growth is regulated by AGN feedback, which appears as the knees in the low-z SMFs. Meanwhile, at bright ends of the UV LFs, the number of bright galaxies rapidly decreases possibly due to mass quenching.

The SMFs and UV LFs present similar evolutionary trends in the low-mass (faint) regimes. Meanwhile, the evolutionary trends at the massive (bright) ends are opposite between the SMFs and UV LFs, but both may be governed by the same physical mechanism (mass quenching).

5.5.2 Link between Low-Mass Galaxies and Extended Lyα Emission

Figure 5.12 shows the possible relation of Lyα emission and low-mass galaxies presented in the SMFs. Because the typical $M_\star$ values of LAEs are $\sim 10^9\ M_\odot$ at $z \sim 2$ (Kusakabe et al. 2018, green shade), LAEs are less massive than $M_\star^*$ of the SMFs.

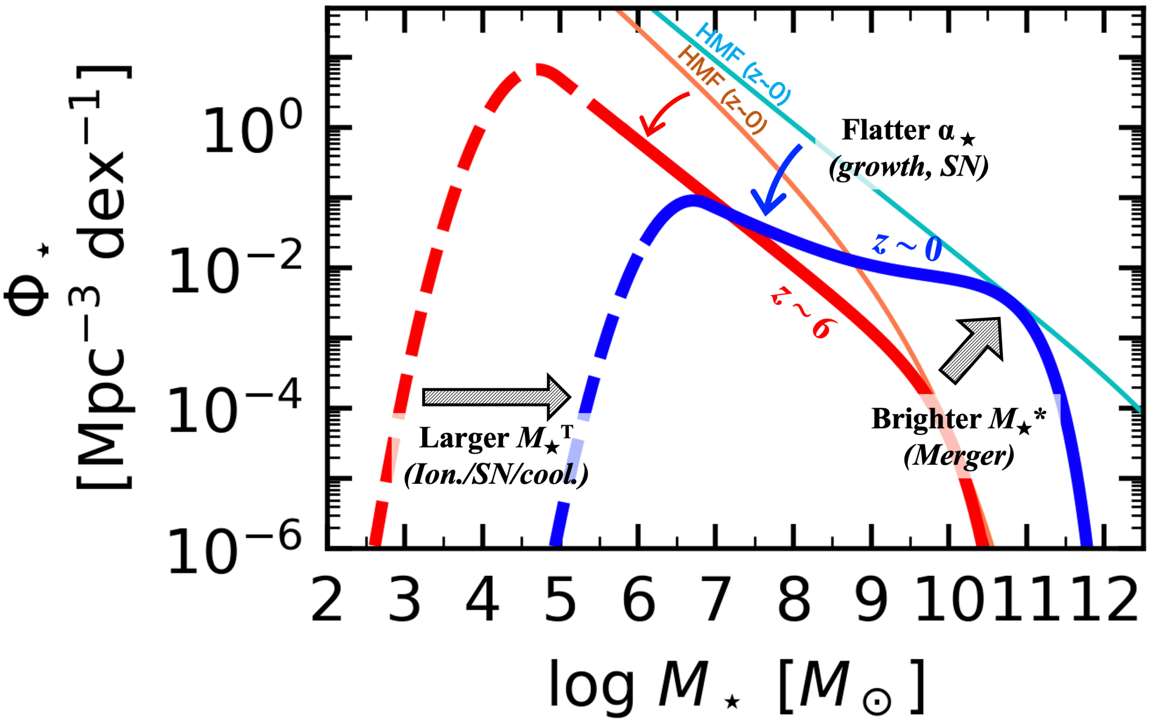

Figure 5.10 Overview of the redshift evolution of the SMFs. The blue thick line shows our best-fit truncated Schechter SMF at $z \sim 0$ (the dashed part is the extrapolation). The red thick solid and dashed lines represent our best-fit Schechter SMF at $z \sim 6$ and the truncated SMF assuming that $M_\star^{\rm T} = 10^{4.7}\, M_\odot$ from the theoretical prediction (Figure 5.4). The orange and cyan thin lines are the Sheth et al. (2001) HMFs at $z \sim 6$ and 0, respectively, that are scaled to the SMFs. The arrows and texts explain the three key features of the redshift evolution of the SMFs. The physical process governing each feature is shown in the parenthesis.

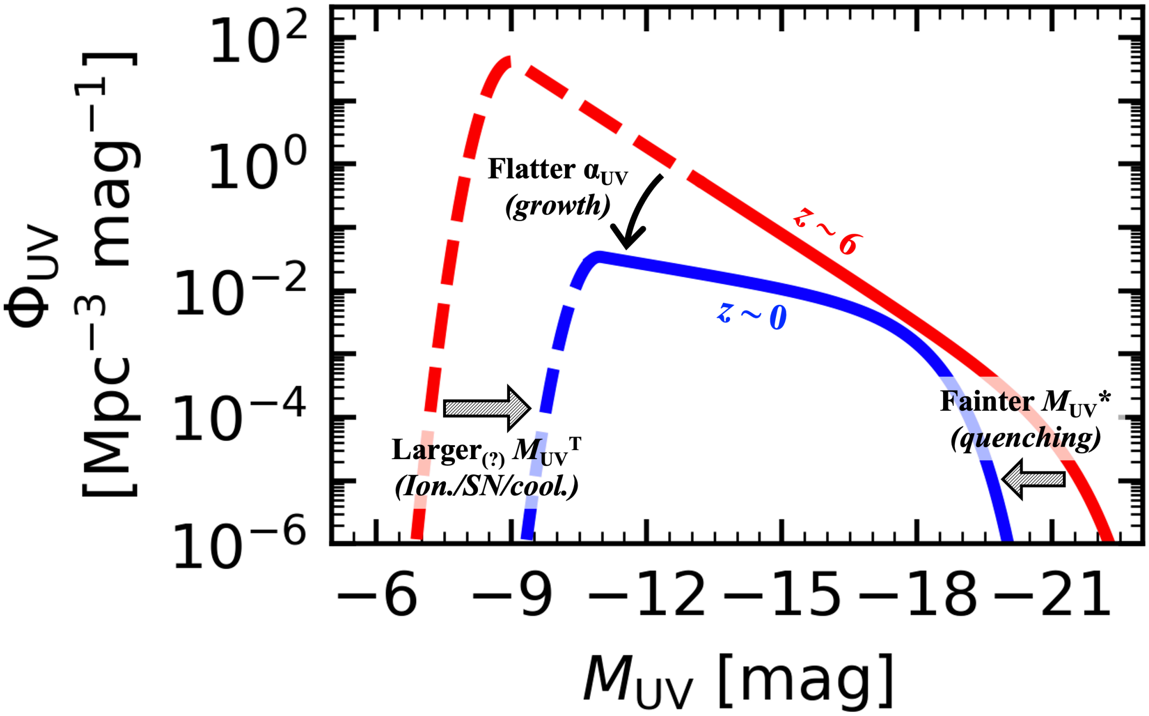

Figure 5.11 Same as Figure 5.10, but for the UV LFs at $z \sim 6-7$ (red) and 0 (blue). The former is taken from Ishigaki et al. (2018) and extrapolated with the assumption that $M_{\rm UV}^{\rm T} = -9$ mag (see Figure 5.6), while the latter is obtained in our work.

The black arrows denote $M_\star$ of the local satellite galaxies that are at the helio-centric distances $d_{\rm helio}$ less than 300 kpc (Drlica-Wagner et al. 2020, see also McConnachie 2012; Newton et al. 2018). In particular, we select those brighter than -8 mag in the Johnson V-band (Johnson & Morgan 1953; Johnson 1955) absolute magnitudes M_V, and exclude the Large and Small Magellanic Clouds (LMC and SMC, respectively). We convert M_V to $M_\star$ assuming that $M_\star/L_V = 2\ M_\odot/L_\odot$ (Jethwa et al. 2018) and $L_V = 10^{-0.4(M_V-4.8)}$ (Willmer 2018). As seen in the Figure, we find that the satellite galaxies are located in the low-mass ends of the SMFs.

In Section 5.4, we found that the extended Lyα emission around a central LAE is caused by the resonant scattering process in the CGM and IGM, and/or is originated from other halos, i.e., satellite galaxies outside $R_{\rm vir}$. Therefore, if the latter scenario is true, it is suggested that low-mass-end galaxies emit Lyα photons and contribute to the extended Lyα emission around the LAE. Bacon et al. (2021) suggest that, if the extended Lyα emission is powered solely by star formation in clustering dwarf galaxies (i.e., other halos in our definition), their SFRs should be as low as 10^{-4} $M_\odot$ yr^{-1}, which corresponds to $M_{\rm UV} \sim -8$ mag. The potential existence of such ultra faint galaxies does not contradict the predicted turnovers in UV LFs ($M_{\rm UV}^{\rm T} \gtrsim -10$ mag) at $z > 3$ (Section 5.2.2).

5.5.3 Link between Low-Mass Galaxies and Milky Way Satellites

Figure 5.13 compares the SMFs of the local satellite galaxies and our $z \sim 0$ SMF. We take the satellite galaxies at $d_{\rm helio} < 300$ kpc from Drlica-Wagner et al. (2020) . We estimate their SMF starting from their V-band number density (dN/dM_V). First, dN/dM_V is converted to the stellar mass number density dN/d$\log M_\star$ by assuming $M_\star/L_V = 2\ M_\odot/L_\odot$. We roughly correct d$N$/d$\log M_\star$ for the survey volume by multiplying $1/V = [(4/3)\pi \times (300\ {\rm kpc})^3]^{-1} \times 10^{-3}$, where the second term represents $\Phi_\star$ of a Milky Way-mass galaxy. The resulting SMF is shown with the black boxes.

The SMF is bimodal; the sources with $M_V < -8$ mag and $M_V > -8$ mag are referred to as satellite galaxies (of the narrow sense; purple line) and ultra-faint dwarfs (UFDs, gray line), respectively (e.g., Newton et al. 2018; Simon 2019). We find that the SMFs of the satellite galaxies and our low-mass galaxies are similar around the

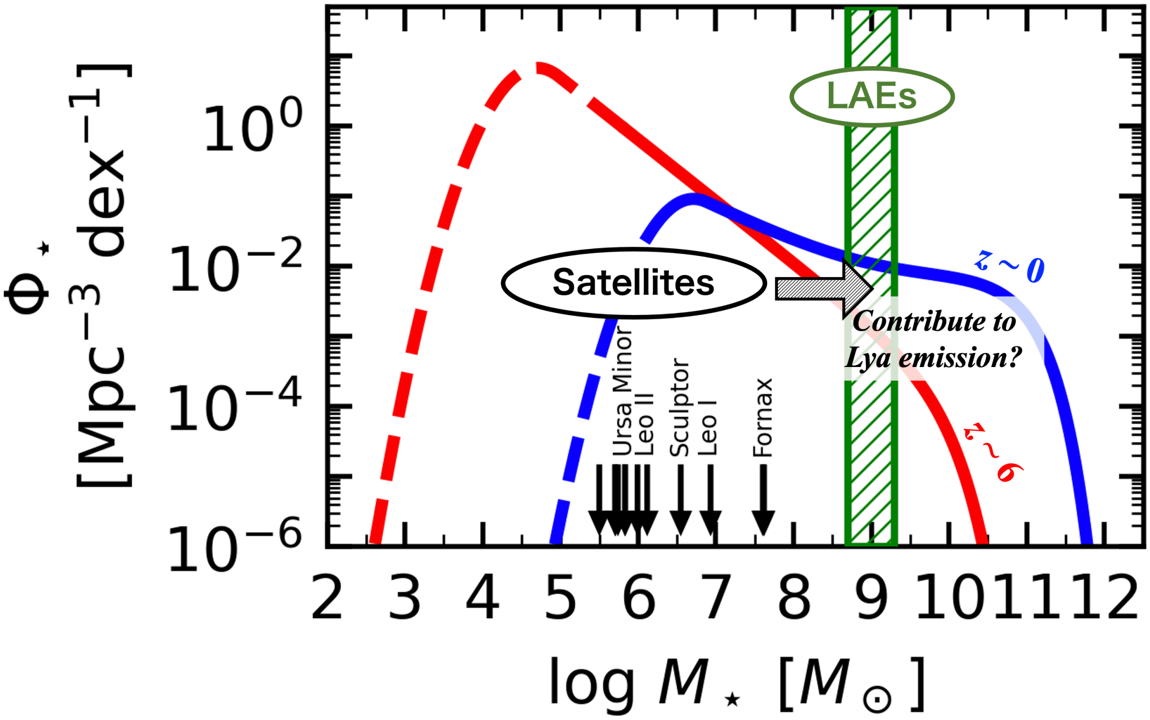

Figure 5.12 Possible relation of LAEs and low-mass galaxies. The green shade show the typical $M_\star$ range of $z \sim 2$ LAEs ($M_\star \sim 10^9$ $M_\odot$; Kusakabe et al. 2018). The red and blue lines show our SMFs at $z \sim 6$ and 0, respectively (same as those shown in Figure 5.10). The black arrows denote $M_\star$ of the local satellites at $d_{\rm helio} < 300$ kpc and brighter than $M_V = -8$ mag (Drlica-Wagner et al. 2020, LMC and SMC are omitted). As discussed in Section 5.4, such dwarf galaxies outside $R_{\rm vir}$ may contribute to extended Lyα emission around LAEs.

low-mass limit of our SMF.

Given that our sample is central galaxies, i.e., those residing in the centers of main halos, the similar SMFs of the satellite and our low-mass galaxies may imply that they form in the same physical mechanism.

The SMF of the UFDs presents a hump below the turnover mass of the SMFs of the satellite galaxies and our low-mass galaxies. This implies that the UFDs form in a different physical process. The first possibility is that they form in the early epoch of the universe, particularly before the UVB becomes strong, and survive until the present (Ricotti & Gnedin 2005; Gnedin & Kravtsov 2006; Salvadori & Ferrara 2009; Ricotti et al. 2016; Bose et al. 2018, e.g.,). For example, the models of Lacey et al. (2016) and Bose et al. (2018) predict that > 70 % of $M_\star = 10^4$ galaxies form at $z > 6$. This is roughly consistent with the smaller $M_\star^{\rm T}$ values at high redshifts (Section 5.2.1). Another scenario is tidal disruption (e.g., Simon & Geha 2007; Muñoz et al. 2010; Ferrarese et al. 2016; Newton et al. 2018; Martin et al. 2021).

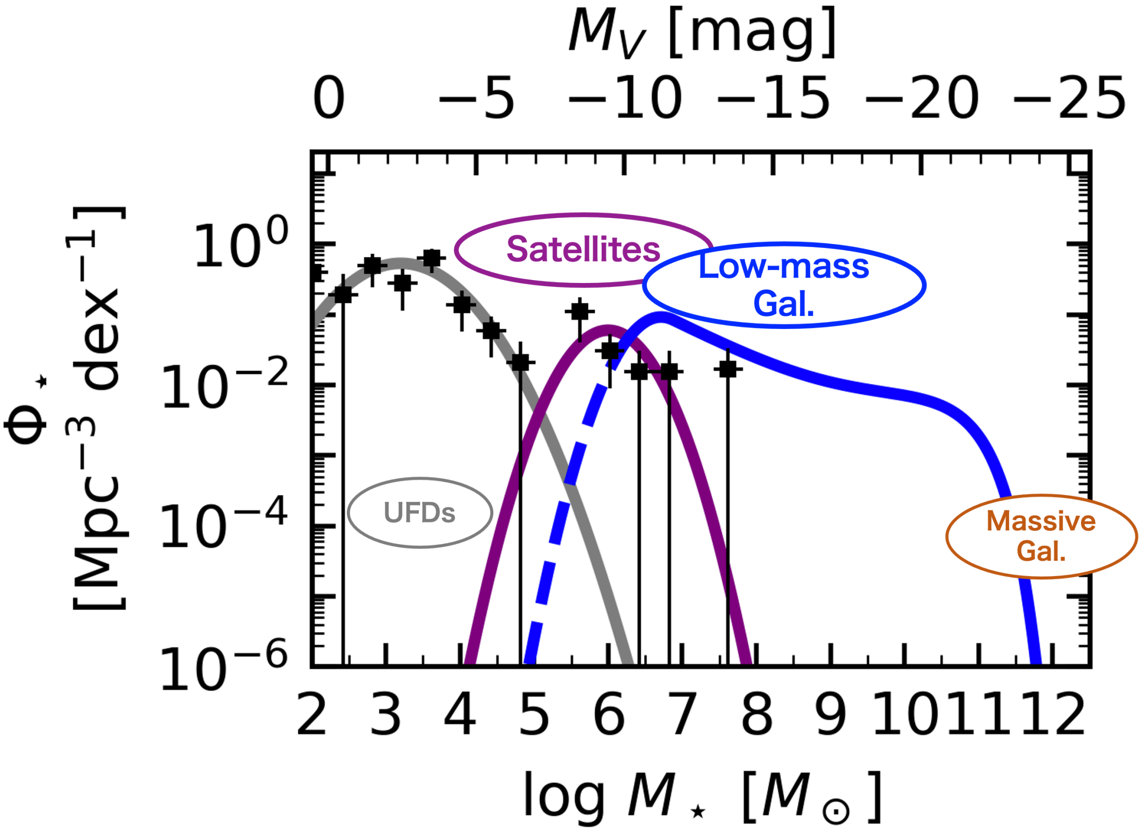

Figure 5.13 Relation of the local satellite galaxies and our low-mass galaxies at $z \sim 0$. The blue line is our UV LF (same as those shown in Figure 5.10). The black boxes denote the SMFs of the satellites at $d_{\rm helio} < 300$ kpc (Drlica-Wagner et al. 2020). The purple and gray lines roughly illustrate the bimodality of the satellite SMFs, corresponding to satellite galaxies and UFDs, respectively (see text). The colored circles represent the typical $M_\star$ ranges of the massive galaxies, our low-mass galaxies, local satellite galaxies, and UFDs. The satellite galaxies share the same $M_\star$ ranges as the low-mass galaxies (our main targets in this thesis) at $M_\star \sim 10^5 - 10^8$ $M_\odot$.

CHAPTER 6
SUMMARY

In this thesis, we investigate the formation of low-mass galaxies over $z \sim 9$ to 0, using large and multiwavelength observational data sets. For a comprehensive understanding, we focus on SMFs, UV LFs, and Lyα emission profiles, which are indicators of completed, ongoing, and future star formation, respectively.

First, we investigate SMFs at $z \sim 0-10$. We derive SMFs at $z \sim 6-9$ using 453 dropouts and the deep HST+*Spitzer* images taken from the full data sets of the HFF, in conjunction with ground-based NIR images of Keck and VLT (Figure 2.7). We investigate the stellar populations of the dropouts, and apply the $M_\star$-$M_{\rm UV}$ relations to the UV LFs to derive the SMFs. We also estimate an SMF at $z \sim 0$ using an SDSS optical spectroscopic catalog that provides stellar population properties of the sources (Figure 2.10). We estimate the SMF by applying the $1/V_{\rm max}$ method to 651202 galaxies at $z = 0.003-0.2$ over ~ 9400 deg^2. Our major findings are summarized below:

1. We find that our SMFs at $z \sim 6-9$ and 0 agree with those obtained in previous studies at intermediate and high-mass regimes ($M_\star \sim 10^7-10^{12}\ M_\odot$), and reach down to $M_\star \sim 10^6\ M_\odot$ (Figure 2.12). We fit Schechter functions to the SMFs at $z \sim 6-9$ and 0, finding that the best-fit low-mass-end slopes $\alpha_\star$ are steep at $z \sim 6-9$ and flat at $z \sim 0$ ($\alpha_\star = -1.81^{+0.21}_{-0.18}$, $-1.76^{+0.21}_{-0.19}$, -1.88 ± 0.07, and $-1.54^{+0.09}_{-0.08}$ at $z \sim 9$, 8, $6-7$, and 0, respectively). While the normalization factors $\phi^*_\star$ rapidly increase especially at $z < 3$ as the low-mass galaxies undergo merging events, the characteristic stellar mass $M^*_\star$ remains constant at $\sim 10^{11}\ M_\odot$ probably due to AGN feedback.

2. We identify a clear ($> 2\sigma$) turnover in our $z \sim 0$ SMF, for the first time, at $M^{\rm T}_\star = 6.71^{+0.60}_{-0.42} \times 10^6\ M_\odot$. Meanwhile, no significant turnovers are found down to $\sim 10^6\ M_\odot$ in any $z \sim 6-9$ SMFs. These results indicate a moderate increasing trend of $M^{\rm T}_\star$ toward low redshifts. Comparing the results with models and simulations, we find that the turnovers can be explained by strong suppression of star formation by photoionization by the UVB radiation, SN feedback, and/or insufficient gas cooling (Figure 5.4).

3. Integrating the GSMFs, we find that the number density fraction of the $M_\star < 10^8\ M_\odot$ galaxies is large (> 80 %) throughout the cosmic history (Figure 5.1). Such low-mass galaxies also contribute to the total SMDs by ~ 30 % at $z > 5$. We estimate the total SMDs between $10^8 \leq M_\star/M_\odot \leq 10^{13}$, confirming that the value at $z \sim 0$ and $6-7$ agree with the finding in the literature. Meanwhile, our total SMDs at $z > 8$ are large, which is consistent with a slow evolution of the cosmic SFRDs, rather than a rapid evolution (Figure 5.2).
4. We estimate the R_e-$M_\star$ relations of our $z \sim 6-9$ dropouts (Figure 5.7). We find that four of our $z \sim 6-7$ dropouts are very compact ($R_\mathrm{e} \leq 40$ physical pc) and low-mass ($M_\star \leq 10^7\ M_\odot$), comparably to the Milky Way GCs.

Next, we discuss UV LFs at $z \sim 0-10$. We derive the UV LF at $z \sim 0$ by applying the $1/V_\mathrm{max}$ method to 67277 galaxies at $z = 0.003-0.2$ taken from the latest (GR6/7) GALEX source catalog and the SDSS spectroscopic catalog. Our findings are listed below:

1. We find that our $z \sim 0$ UV LF agrees with those taken from the literature in the bright and intermediate magnitude ranges ($-20 < M_\mathrm{UV} < -12$; Figure 3.3). We fit a Schechter function to our UV LF, finding a very flat faint-end ($\alpha_\mathrm{UV} = -1.30 \pm 0.01$).
2. We compare our $z \sim 0$ UV LF with those at high redshifts (Figure 3.5). We find increasing trends of α_UV and ϕ^*_UV toward low redshifts, which implies the growth of galaxies. At $z < 3$, the UV LFs move toward the faint ends (M^*_UV becomes fainter while ϕ^*_UV remains constant), possibly due to mass quenching.
3. We identify a tentative turnover at $M^\mathrm{T}_\mathrm{UV} \sim -11$ mag ($M^\mathrm{T}_\mathrm{UV} = -11.7^{+0.83}_{-0.46}$ or $-11.0^{+11.0}_{-2.9}$ according to whether we include the faint-end hump or not, respectively). On the contrary, only weak constraints have been obtained so far at $z > 1$ due to observational limits and lens model uncertainties, which makes it impossible to reveal the redshift evolution of M^T_UV. Comparing the result with models, we find that our M^T_UV estimation is reproduced by either photoionization and/or SN feedback (Figure 5.4).
4. We estimate the fractional number and UV luminosity densities of the low-mass galaxies (Figure 5.3). Faint galaxies with $M_\mathrm{UV} < -16$ mag are prevalent (> 60

%) all through the cosmic history. Similarly, $\sim 30-60$ % of the total luminosity densities is contributed from the galaxies fainter than $M_{\rm UV} \sim -18$ mag.

Lastly, we probe very extended Lyα emission around LAEs at $z = 2.2 - 6.6$. We apply the intensity mapping technique to 1781 LAEs at $z = 2.2$, 3.3, 5.7, and 6.6 and Lyα emission traced by the ultra-deep NB387, NB527, NB816, and NB921 images taken from the HSC-SSP and CHORUS projects. Our main results are as follows:

1. Subtracting the systematics, we identify Lyα emission of $\sim 10^{-20} - 10^{-19}$ erg s^{-1} cm^{-2} arcsec^{-2} with S/N = 4.1 around the $z = 3.3$ LAEs. At this redshift, Lyα emission is extended beyond the radial scale of the $R_{\rm vir}$ of a DMH with 10^{11} $M_\odot$ (~ 100 ckpc), and up to ~ 1 cMpc (Figure 4.5). We also tentatively detect Lyα emission beyond the $R_{\rm vir}$ scales at $z = 5.7$, and 6.6 with S/N ~ 2. Extended Lyα emission is also tentatively detected around the $z = 2.2$ LAEs when faint LAEs are excluded from the sample.

2. We confirm that the SB$_{\rm Ly\alpha}$ radial profiles agree well with those obtained in the previous studies, when the LAEs have similar Lyα luminosities (Figure 4.6).

3. We compare the *observed* SB$_{\rm Ly\alpha}$ across $z = 2.2 - 6.6$, finding no significant difference among the redshifts beyond the uncertainties. Meanwhile, we find a potential decreasing trend toward low redshifts in the profiles of *intrinsic* SB$_{\rm Ly\alpha}$, which is corrected for the cosmological dimming effect (Figure 4.8). The trend roughly follows $(1+z)^{-3}$, which might be explained by the decreasing density of the neutral hydrogen gas due to the cosmic expansion.

4. We investigate the origins and physical mechanisms of the extended Lyα emission by comparing the observational results with theoretical studies (Figure 5.9). We find that the extended Lyα emission beyond $R_{\rm vir}$ may be reproduced by resonant scattering in the CGM and IGM, and/or emission originating from satellite galaxies that are $> R_{\rm vir}$ away from the central LAE.

Through these investigations, we confirm that SMFs, UV LFs, and Lyα emission are closely connected. For example, both SMFs and UV LFs present steep slopes at high redshifts, which reflect abundant low-mass galaxies in the early universe. The slopes become flatter toward low redshifts as the galaxies undergo merging events

(Figures 5.10 and 5.11). Turnovers are identified in the $z \sim 0$ SMF and tentatively in the $z \sim 0$ UV LF, which indicates complete suppression of star formation due to photoionization by the UVB, SN feedback, and/or the gas cooling limit. Such low-mass/faint galaxies might contribute to the extended Lyα emission around comparably massive (but still less massive than $M_\star^*$) galaxies (Figure 5.12). We also find that our SMF at $z \sim 0$ including the turnover is consistent with that of the local satellite galaxies. This may suggest that the local satellite galaxies and central galaxies share the common formation process (Figure 5.13).

Our study is characterized by very wide dynamic ranges of stellar mass ($10^5 < M_\star/M_\odot < 10^{12}$), UV magnitude ($-10 < M_{\rm UV} < -21$), redshift ($0 < z < 10$). Our findings owe the analyses using large data sets including various surveys over deep to wide, UV to MIR observations.

REFERENCES

Acquaviva, V., Raichoor, A., & Gawiser, E. 2015, ApJ, 804, 8

Aihara, H., AlSayyad, Y., Ando, M., et al. 2019, PASJ, 71, 114

Alavi, A., Siana, B., Richard, J., et al. 2016, ApJ, 832, 56

Ann, H. B., Seo, M., & Ha, D. K. 2015, ApJS, 217, 27

Arnouts, S., Schiminovich, D., Ilbert, O., et al. 2005, ApJ, 619, L43

Arrigoni Battaia, F., Hennawi, J. F., Prochaska, J. X., et al. 2019, MNRAS, 482, 3162

Atek, H., Richard, J., Kneib, J.-P., & Schaerer, D. 2018, MNRAS, 479, 5184

Bañados, E., Hung, L.-W., De Propris, R., & West, M. J. 2010, ApJ, 721, L14

Bacon, R., Accardo, M., Adjali, L., et al. 2010, in Society of Photo-Optical Instrumentation Engineers (SPIE) Conference Series, Vol. 7735, Ground-based and Airborne Instrumentation for Astronomy III, ed. I. S. McLean, S. K. Ramsay, & H. Takami, 773508

Bacon, R., Mary, D., Garel, T., et al. 2021, A&A, 647, A107

Baldry, I. K., Glazebrook, K., & Driver, S. P. 2008, MNRAS, 388, 945

Baldry, I. K., Driver, S. P., Loveday, J., et al. 2012, MNRAS, 421, 621

Barkana, R., & Loeb, A. 2001, Phys. Rep., 349, 125

Baumgardt, H., & Hilker, M. 2018, MNRAS, 478, 1520

Behroozi, P., Wechsler, R. H., Hearin, A. P., & Conroy, C. 2019, MNRAS, 488, 3143

Behroozi, P. S., Wechsler, R. H., & Conroy, C. 2013, ApJ, 770, 57

Bertin, E., & Arnouts, S. 1996, A&AS, 117, 393

Bhatawdekar, R., Conselice, C. J., Margalef-Bentabol, B., & Duncan, K. 2019, MNRAS, 486, 3805

Bianchi, L., de la Vega, A., Shiao, B., & Souter, B. J. 2019, ApJS, 241, 14

Bianchi, L., & Shiao, B. 2020, ApJS, 250, 36

Bianchi, L., Shiao, B., & Thilker, D. 2017, ApJS, 230, 24

Bielby, R., Hudelot, P., McCracken, H. J., et al. 2012, A&A, 545, A23

Bielby, R. M., Shanks, T., Crighton, N. H. M., et al. 2017, MNRAS, 471, 2174

Binggeli, B., Tammann, G. A., & Sandage, A. 1987, AJ, 94, 251

Blanton, M. R., Bershady, M. A., Abolfathi, B., et al. 2017, AJ, 154, 28

Borisova, E., Cantalupo, S., Lilly, S. J., et al. 2016, ApJ, 831, 39

Bosch, J., Armstrong, R., Bickerton, S., et al. 2018, PASJ, 70, S5

Bose, S., Deason, A. J., & Frenk, C. S. 2018, ApJ, 863, 123

Bouwens, R. J., Illingworth, G. D., Oesch, P. A., et al. 2017a, ArXiv e-prints, arXiv:1711.02090

Bouwens, R. J., Illingworth, G. D., van Dokkum, P. G., et al. 2021a, arXiv e-prints, arXiv:2112.02948

—. 2021b, AJ, 162, 255

Bouwens, R. J., Oesch, P. A., Illingworth, G. D., Ellis, R. S., & Stefanon, M. 2017b, ApJ, 843, 129

Bouwens, R. J., Illingworth, G. D., Franx, M., et al. 2009, ApJ, 705, 936

Bouwens, R. J., Illingworth, G. D., Oesch, P. A., et al. 2015, ApJ, 803, 34

Bouwens, R. J., Oesch, P. A., Stefanon, M., et al. 2021c, AJ, 162, 47

Bowler, R. A. A., Dunlop, J. S., McLure, R. J., et al. 2014, MNRAS, 440, 2810

Bradley, L. D., Trenti, M., Oesch, P. A., et al. 2012, ApJ, 760, 108

Brammer, G. B., van Dokkum, P. G., & Coppi, P. 2008, ApJ, 686, 1503

Brammer, G. B., Marchesini, D., Labbé, I., et al. 2016, ApJS, 226, 6

Bruzual, G., & Charlot, S. 2003, MNRAS, 344, 1000

Budavári, T., Szalay, A. S., Charlot, S., et al. 2005, ApJ, 619, L31

Bullock, J. S. 2010, arXiv e-prints, arXiv:1009.4505

Byrohl, C., Nelson, D., Behrens, C., et al. 2021, MNRAS, 506, 5129

Cai, Z.-Y., Lapi, A., Bressan, A., et al. 2014, ApJ, 785, 65

Calvi, V., Trenti, M., Stiavelli, M., et al. 2016, ApJ, 817, 120

Calzetti, D., Kinney, A. L., & Storchi-Bergmann, T. 1994, ApJ, 429, 582

Cantalupo, S., Arrigoni-Battaia, F., Prochaska, J. X., Hennawi, J. F., & Madau, P. 2014, Nature, 506, 63

Cantalupo, S., Porciani, C., Lilly, S. J., & Miniati, F. 2005, ApJ, 628, 61

Carilli, C. L. 2011, ApJ, 730, L30

Castellano, M., Yue, B., Ferrara, A., et al. 2016, ApJ, 823, L40

Chabrier, G. 2003, PASP, 115, 763

Chen, Y., Steidel, C. C., Erb, D. K., et al. 2021, MNRAS, 508, 19

Chevallard, J., & Charlot, S. 2016, MNRAS, 462, 1415

Coe, D., Bradley, L., & Zitrin, A. 2015, ApJ, 800, 84

Colless, M., Dalton, G., Maddox, S., et al. 2001, MNRAS, 328, 1039

Comaschi, P., & Ferrara, A. 2016a, MNRAS, 463, 3078

—. 2016b, MNRAS, 455, 725

Comparat, J., Maraston, C., Goddard, D., et al. 2017, arXiv e-prints, arXiv:1711.06575

Conselice, C. J., Rajgor, S., & Myers, R. 2008, MNRAS, 386, 909

Croft, R. A. C., Miralda-Escudé, J., Zheng, Z., Blomqvist, M., & Pieri, M. 2018, MNRAS, 481, 1320

Croft, R. A. C., Miralda-Escudé, J., Zheng, Z., et al. 2016, MNRAS, 457, 3541

Croton, D. J., Springel, V., White, S. D. M., et al. 2006, MNRAS, 365, 11

Cucciati, O., Tresse, L., Ilbert, O., et al. 2012, A&A, 539, A31

Dahlen, T., Mobasher, B., Faber, S. M., et al. 2013, ApJ, 775, 93

Davidzon, I., Ilbert, O., Laigle, C., et al. 2017, A&A, 605, A70

Dawson, K. S., Schlegel, D. J., Ahn, C. P., et al. 2013, AJ, 145, 10

Dayal, P., Ferrara, A., Dunlop, J. S., & Pacucci, F. 2014, MNRAS, 445, 2545

De Vis, P., Gomez, H. L., Schofield, S. P., et al. 2017, MNRAS, 471, 1743

Dekel, A., & Silk, J. 1986, ApJ, 303, 39

Diemer, B. 2018, ApJS, 239, 35

Dijkstra, M., & Kramer, R. 2012, MNRAS, 424, 1672

Driver, S. P., Robotham, A. S. G., Kelvin, L., et al. 2012, MNRAS, 427, 3244

Drlica-Wagner, A., Bechtol, K., Mau, S., et al. 2020, ApJ, 893, 47

Duncan, K., Conselice, C. J., Mortlock, A., et al. 2014, MNRAS, 444, 2960

Efstathiou, G. 1992, MNRAS, 256, 43P

Eisenstein, D. J., Weinberg, D. H., Agol, E., et al. 2011, AJ, 142, 72

Ellis, R. S., McLure, R. J., Dunlop, J. S., et al. 2013, ApJ, 763, L7

Elsner, F., Feulner, G., & Hopp, U. 2008, A&A, 477, 503

Fardal, M. A., Katz, N., Gardner, J. P., et al. 2001, ApJ, 562, 605

Faucher-Giguère, C.-A., Kereš, D., Dijkstra, M., Hernquist, L., & Zaldarriaga, M. 2010, ApJ, 725, 633

Faucher-Giguère, C.-A., Kereš, D., & Ma, C.-P. 2011, MNRAS, 417, 2982

Felten, J. E. 1976, ApJ, 207, 700

Ferland, G. J., Porter, R. L., van Hoof, P. A. M., et al. 2013, RMxAA, 49, 137

Feroz, F., & Hobson, M. P. 2008, MNRAS, 384, 449

Feroz, F., Hobson, M. P., & Bridges, M. 2009, MNRAS, 398, 1601

Ferrarese, L., Côté, P., Sánchez-Janssen, R., et al. 2016, ApJ, 824, 10

Finkelstein, S. L., Ryan, Jr., R. E., Papovich, C., et al. 2015, ApJ, 810, 71

Finlator, K., Oh, S. P., Özel, F., & Davé, R. 2012, MNRAS, 427, 2464

Finlator, K., Prescott, M. K. M., Oppenheimer, B. D., et al. 2017, MNRAS, 464, 1633

Fisher, Ronald Aylmer, S. 1970, Statistical methods for research workers, 14th edn. (Edinburgh : Oliver and Boyd)

Fonseca, J., Silva, M. B., Santos, M. G., & Cooray, A. 2017, MNRAS, 464, 1948

Fontana, A., Salimbeni, S., Grazian, A., et al. 2006, A&A, 459, 745

Foreman-Mackey, D. 2016, The Journal of Open Source Software, 1, 24

Fujimoto, S., Ouchi, M., Ferrara, A., et al. 2019, ApJ, 887, 107

Fukugita, M., & Kawasaki, M. 2021, arXiv e-prints, arXiv:2111.01389

Furlanetto, S. R., Schaye, J., Springel, V., & Hernquist, L. 2005, ApJ, 622, 7

Gallego, S. G., Cantalupo, S., Lilly, S., et al. 2018, MNRAS, 475, 3854

Garel, T., Blaizot, J., Rosdahl, J., et al. 2021, MNRAS, 504, 1902

Giavalisco, M., Ferguson, H. C., Koekemoer, A. M., et al. 2004, ApJ, 600, L93

Gnedin, N. Y. 2000, ApJ, 542, 535

—. 2016, ApJ, 825, L17

Gnedin, N. Y., & Kravtsov, A. V. 2006, ApJ, 645, 1054

Goerdt, T., Dekel, A., Sternberg, A., et al. 2010, MNRAS, 407, 613

Gong, Y., Cooray, A., Silva, M. B., Santos, M. G., & Lubin, P. 2011, ApJ, 728, L46

González, V., Labbé, I., Bouwens, R. J., et al. 2011, ApJ, 735, L34

Goto, H., Shimasaku, K., Yamanaka, S., et al. 2021, ApJ, 923, 229

Goto, T., Utsumi, Y., Furusawa, H., Miyazaki, S., & Komiyama, Y. 2009, MNRAS, 400, 843

Grazian, A., Fontana, A., Santini, P., et al. 2015, A&A, 575, A96

Grogin, N. A., Kocevski, D. D., Faber, S. M., et al. 2011, ApJS, 197, 35

Gutkin, J., Charlot, S., & Bruzual, G. 2016, MNRAS, 462, 1757

Haardt, F., & Madau, P. 2012, ApJ, 746, 125

Haiman, Z., Spaans, M., & Quataert, E. 2000, ApJ, 537, L5

Harikane, Y., Ouchi, M., Ono, Y., et al. 2016, ApJ, 821, 123

—. 2018a, PASJ, 70, S11

Harikane, Y., Ouchi, M., Shibuya, T., et al. 2018b, ApJ, 859, 84

Harikane, Y., Ouchi, M., Ono, Y., et al. 2019, ApJ, 883, 142

Harikane, Y., Ono, Y., Ouchi, M., et al. 2021, arXiv e-prints, arXiv:2108.01090

Hayashi, M., Shimakawa, R., Tanaka, M., et al. 2020, PASJ, 72, 86

Hayashino, T., Matsuda, Y., Tamura, H., et al. 2004, AJ, 128, 2073

Hayes, M., Schaerer, D., Östlin, G., et al. 2011, ApJ, 730, 8

Hayes, M., Östlin, G., Schaerer, D., et al. 2013, ApJ, 765, L27

Hayes, M., Östlin, G., Duval, F., et al. 2014, ApJ, 782, 6

Higuchi, R., Ouchi, M., Ono, Y., et al. 2019, ApJ, 879, 28

Hogg, D. W. 1999, arXiv e-prints, arXiv:astro-ph/9905116

Hopkins, P. F., Hernquist, L., Cox, T. J., & Kereš, D. 2008, ApJS, 175, 356

Hutter, A., Dayal, P., Yepes, G., et al. 2021, MNRAS, 503, 3698

Ilbert, O., McCracken, H. J., Le Fèvre, O., et al. 2013, A&A, 556, A55

Inoue, A. K., Shimizu, I., Iwata, I., & Tanaka, M. 2014, MNRAS, 442, 1805

Inoue, A. K., Hasegawa, K., Ishiyama, T., et al. 2018, PASJ, 70, 55

Inoue, A. K., Yamanaka, S., Ouchi, M., et al. 2020, PASJ, 72, 101

Ishigaki, M., Kawamata, R., Ouchi, M., et al. 2015, ApJ, 799, 12

—. 2018, ApJ, 854, 73

Ishigaki, M., Ouchi, M., & Harikane, Y. 2016, ApJ, 822, 5

Itoh, R., Ouchi, M., Zhang, H., et al. 2018, ApJ, 867, 46

Jaacks, J., Thompson, R., & Nagamine, K. 2013, ApJ, 766, 94

Jeeson-Daniel, A., Ciardi, B., Maio, U., et al. 2012, MNRAS, 424, 2193

Jeffreys, H. 1961, Theory of Probability (Cambridge)

Jethwa, P., Erkal, D., & Belokurov, V. 2018, MNRAS, 473, 2060

Johnson, H. L. 1955, Annales d'Astrophysique, 18, 292

Johnson, H. L., & Morgan, W. W. 1953, ApJ, 117, 313

Kakiichi, K., & Dijkstra, M. 2018, MNRAS, 480, 5140

Kakuma, R., Ouchi, M., Harikane, Y., et al. 2021, ApJ, 916, 22

Karademir, G. S., Taylor, E. N., Blake, C., et al. 2022, MNRAS, 509, 5467

Katz, H., Ramsoy, M., Rosdahl, J., et al. 2020, MNRAS, 494, 2200

Kawamata, R., Ishigaki, M., Shimasaku, K., et al. 2018, ApJ, 855, 4

Kawamata, R., Oguri, M., Ishigaki, M., Shimasaku, K., & Ouchi, M. 2016, ApJ, 819, 114

Kelvin, L. S., Driver, S. P., Robotham, A. S. G., et al. 2014, MNRAS, 444, 1647

Kikuta, S., Matsuda, Y., Cen, R., et al. 2019, PASJ, 71, L2

Kitayama, T., Susa, H., Umemura, M., & Ikeuchi, S. 2001, MNRAS, 326, 1353

Klypin, A., Kravtsov, A. V., Valenzuela, O., & Prada, F. 1999, ApJ, 522, 82

Koekemoer, A. M., Faber, S. M., Ferguson, H. C., et al. 2011, ApJS, 197, 36

Kollmeier, J. A., Zheng, Z., Davé, R., et al. 2010, ApJ, 708, 1048

Konno, A., Ouchi, M., Nakajima, K., et al. 2016, ApJ, 823, 20

Konno, A., Ouchi, M., Shibuya, T., et al. 2018, PASJ, 70, S16

Kovetz, E. D., Viero, M. P., Lidz, A., et al. 2017, arXiv e-prints, arXiv:1709.09066

Kravtsov, A. 2010, Advances in Astronomy, 2010, 281913

Kusakabe, H., Shimasaku, K., Ouchi, M., et al. 2018, PASJ, 70, 4

Kusakabe, H., Shimasaku, K., Momose, R., et al. 2019, PASJ, 71, 55

Lacey, C., & Cole, S. 1993, MNRAS, 262, 627

Lacey, C. G., Baugh, C. M., Frenk, C. S., et al. 2016, MNRAS, 462, 3854

Lake, E., Zheng, Z., Cen, R., et al. 2015, ApJ, 806, 46

Laursen, P., & Sommer-Larsen, J. 2007, ApJ, 657, L69

Laursen, P., Sommer-Larsen, J., & Razoumov, A. O. 2011, ApJ, 728, 52

Leclercq, F., Bacon, R., Wisotzki, L., et al. 2017, A&A, 608, A8

Leclercq, F., Bacon, R., Verhamme, A., et al. 2020, A&A, 635, A82

Lee, Y., Rey, S.-C., Hilker, M., Sheen, Y.-K., & Yi, S. K. 2016, ApJ, 822, 92

Li, T. Y., Wechsler, R. H., Devaraj, K., & Church, S. E. 2016, ApJ, 817, 169

Licquia, T. C., & Newman, J. A. 2015, ApJ, 806, 96

Liu, C., Mutch, S. J., Angel, P. W., et al. 2016, MNRAS, 462, 235

Livermore, R. C., Finkelstein, S. L., & Lotz, J. M. 2017, ApJ, 835, 113

Loeb, A., & Furlanetto, S. R. 2013, The First Galaxies in the Universe

Lotz, J. M., Koekemoer, A., Coe, D., et al. 2017, ApJ, 837, 97

Madau, P. 2018, MNRAS, 480, L43

Madau, P., & Dickinson, M. 2014, ARA&A, 52, 415

Martin, D. C., Chang, D., Matuszewski, M., et al. 2014, ApJ, 786, 107

Martin, D. C., Fanson, J., Schiminovich, D., et al. 2005, ApJ, 619, L1

Martin, G., Jackson, R. A., Kaviraj, S., et al. 2021, MNRAS, 500, 4937

Mas-Ribas, L., & Dijkstra, M. 2016, ApJ, 822, 84

Mas-Ribas, L., Dijkstra, M., Hennawi, J. F., et al. 2017a, ApJ, 841, 19

Mas-Ribas, L., Hennawi, J. F., Dijkstra, M., et al. 2017b, ApJ, 846, 11

Matsuda, Y., Yamada, T., Hayashino, T., et al. 2012, MNRAS, 425, 878

Matthee, J., Sobral, D., Best, P., et al. 2017, MNRAS, 465, 3637

McConnachie, A. W. 2012, AJ, 144, 4

McKee, C. F., & Ostriker, E. C. 2007, ARA&A, 45, 565

McLeod, D. J., McLure, R. J., & Dunlop, J. S. 2016, MNRAS, 459, 3812

Meneghetti, M., Natarajan, P., Coe, D., et al. 2017, MNRAS, 472, 3177

Mo, H., van den Bosch, F. C., & White, S. 2010, Galaxy Formation and Evolution

Momose, R., Shimasaku, K., Nagamine, K., et al. 2021a, ApJ, 912, L24

Momose, R., Shimizu, I., Nagamine, K., et al. 2021b, ApJ, 911, 98

Momose, R., Ouchi, M., Nakajima, K., et al. 2014, MNRAS, 442, 110

—. 2016, MNRAS, 457, 2318

Montes, M., & Trujillo, I. 2014, ApJ, 794, 137

Moore, B., Ghigna, S., Governato, F., et al. 1999, ApJ, 524, L19

Morrissey, P., Schiminovich, D., Barlow, T. A., et al. 2005, ApJ, 619, L7

Morrissey, P., Conrow, T., Barlow, T. A., et al. 2007, ApJS, 173, 682

Mortlock, A., Conselice, C. J., Bluck, A. F. L., et al. 2011, MNRAS, 413, 2845

Moustakas, J., Coil, A. L., Aird, J., et al. 2013, ApJ, 767, 50

Moutard, T., Sawicki, M., Arnouts, S., et al. 2020, MNRAS, 494, 1894

Muñoz, J. B., Qin, Y., Mesinger, A., et al. 2021, arXiv e-prints, arXiv:2110.13919

Muñoz, R. R., Geha, M., & Willman, B. 2010, AJ, 140, 138

Muzzin, A., Marchesini, D., Stefanon, M., et al. 2013, ApJ, 777, 18

Naab, T., & Ostriker, J. P. 2017, ARA&A, 55, 59

Nakajima, K., Ellis, R. S., Robertson, B. E., Tang, M., & Stark, D. P. 2020, ApJ, 889, 161

Navarro, J. F., Frenk, C. S., & White, S. D. M. 1997, ApJ, 490, 493

Newton, O., Cautun, M., Jenkins, A., Frenk, C. S., & Helly, J. C. 2018, MNRAS, 479, 2853

Nishi, R. 2002, Progress of Theoretical Physics Supplement, 147, 1

Norris, M. A., Kannappan, S. J., Forbes, D. A., et al. 2014, MNRAS, 443, 1151

Ocvirk, P., Aubert, D., Sorce, J. G., et al. 2020, MNRAS, 496, 4087

Oesch, P. A., Bouwens, R. J., Illingworth, G. D., Labbé, I., & Stefanon, M. 2018, ApJ, 855, 105

Oesch, P. A., Bouwens, R. J., Illingworth, G. D., et al. 2013, ApJ, 773, 75

—. 2014, ApJ, 786, 108

Oguri, M. 2010, PASJ, 62, 1017

Okamoto, T., Frenk, C. S., Jenkins, A., & Theuns, T. 2010, MNRAS, 406, 208

Okamoto, T., Gao, L., & Theuns, T. 2008, MNRAS, 390, 920

Oke, J. B., & Gunn, J. E. 1983, ApJ, 266, 713

Ono, Y., Ouchi, M., Shimasaku, K., et al. 2010, ApJ, 724, 1524

Ono, Y., Itoh, R., Shibuya, T., et al. 2021, ApJ, 911, 78

O'Shea, B. W., Wise, J. H., Xu, H., & Norman, M. L. 2015, ApJ, 807, L12

Östlin, G., Hayes, M., Kunth, D., et al. 2009, AJ, 138, 923

Ouchi, M., Ono, Y., & Shibuya, T. 2020, ARA&A, 58, 617

Ouchi, M., Mobasher, B., Shimasaku, K., et al. 2009, ApJ, 706, 1136

Ouchi, M., Shimasaku, K., Furusawa, H., et al. 2010, ApJ, 723, 869

Ouchi, M., Harikane, Y., Shibuya, T., et al. 2018, PASJ, 70, S13

Panter, B., Heavens, A. F., & Jimenez, R. 2004, MNRAS, 355, 764

Papovich, C., Kawinwanichakij, L., Quadri, R. F., et al. 2018, ApJ, 854, 30

Park, J., Mesinger, A., Greig, B., & Gillet, N. 2019, MNRAS, 484, 933

Parsa, S., Dunlop, J. S., McLure, R. J., & Mortlock, A. 2016, MNRAS, 456, 3194

Peng, Y.-j., Lilly, S. J., Kovač, K., et al. 2010, ApJ, 721, 193

Péroux, C., & Howk, J. C. 2020, ARA&A, 58, 363

Popesso, P., Biviano, A., Böhringer, H., & Romaniello, M. 2006, A&A, 445, 29

Pozzetti, L., Bolzonella, M., Zucca, E., et al. 2010, A&A, 523, A13

Press, W. H., & Schechter, P. 1974, ApJ, 187, 425

Priewe, J., Williams, L. L. R., Liesenborgs, J., Coe, D., & Rodney, S. A. 2017, MNRAS, 465, 1030

Pullen, A. R., Doré, O., & Bock, J. 2014, ApJ, 786, 111

Qin, Y., Mesinger, A., Greig, B., & Park, J. 2021, MNRAS, 501, 4748

Quinn, T., Katz, N., & Efstathiou, G. 1996, MNRAS, 278, L49

Rauch, M., Haehnelt, M., Bunker, A., et al. 2008, ApJ, 681, 856

Read, J. I., & Trentham, N. 2005, Philosophical Transactions of the Royal Society of London Series A, 363, 2693

Reddy, N. A., Erb, D. K., Pettini, M., Steidel, C. C., & Shapley, A. E. 2010, ApJ, 712, 1070

Ricotti, M., & Gnedin, N. Y. 2005, ApJ, 629, 259

Ricotti, M., Parry, O. H., & Gnedin, N. Y. 2016, ApJ, 831, 204

Robertson, B. E., Ellis, R. S., Dunlop, J. S., et al. 2014, ApJ, 796, L27

Rodríguez-Puebla, A., Calette, A. R., Avila-Reese, V., Rodriguez-Gomez, V., & Huertas-Company, M. 2020, PASA, 37, e024

Rosdahl, J., & Blaizot, J. 2012, MNRAS, 423, 344

Ross, A. J., Bautista, J., Tojeiro, R., et al. 2020, MNRAS, 498, 2354

Sakamoto, T., Chiba, M., & Beers, T. C. 2003, A&A, 397, 899

Salmon, B., Papovich, C., Finkelstein, S. L., et al. 2015, ApJ, 799, 183

Salpeter, E. E. 1955, ApJ, 121, 161

Salvadori, S., & Ferrara, A. 2009, MNRAS, 395, L6

Santini, P., Fontana, A., Castellano, M., et al. 2017, ApJ, 847, 76

Schechter, P. 1976, ApJ, 203, 297

Schmidt, M. 1968, ApJ, 151, 393

Scoville, N., Aussel, H., Brusa, M., et al. 2007, ApJS, 172, 1

Sekiguchi, K., Akiyama, M., Furusawa, H., et al. 2005, in Multiwavelength Mapping of Galaxy Formation and Evolution, ed. A. Renzini & R. Bender, 82

Sheth, R. K., Mo, H. J., & Tormen, G. 2001, MNRAS, 323, 1

Shibuya, T., Ouchi, M., & Harikane, Y. 2015, ApJS, 219, 15

Shibuya, T., Ouchi, M., Harikane, Y., & Nakajima, K. 2019, ApJ, 871, 164

Shibuya, T., Ouchi, M., Konno, A., et al. 2018a, PASJ, 70, S14

Shibuya, T., Ouchi, M., Harikane, Y., et al. 2018b, PASJ, 70, S15

Shipley, H. V., Lange-Vagle, D., Marchesini, D., et al. 2018, ApJS, 235, 14

Silva, M. B., Santos, M. G., Gong, Y., Cooray, A., & Bock, J. 2013, ApJ, 763, 132

Simon, J. D. 2019, ARA&A, 57, 375

Simon, J. D., & Geha, M. 2007, ApJ, 670, 313

Smith, A., Ma, X., Bromm, V., et al. 2019, MNRAS, 484, 39

Smith, A., Tsang, B. T. H., Bromm, V., & Milosavljević, M. 2018, MNRAS, 479, 2065

Somerville, R. S., & Davé, R. 2015, ARA&A, 53, 51

Song, M., Finkelstein, S. L., Ashby, M. L. N., et al. 2016, ApJ, 825, 5

Speagle, J. S., Steinhardt, C. L., Capak, P. L., & Silverman, J. D. 2014, ApJS, 214, 15

Stark, D. P., Schenker, M. A., Ellis, R., et al. 2013, ApJ, 763, 129

Stefanon, M., Bouwens, R. J., Labbé, I., et al. 2021, ApJ, 922, 29

—. 2017, ApJ, 843, 36

Steidel, C. C., Adelberger, K. L., Giavalisco, M., Dickinson, M., & Pettini, M. 1999, ApJ, 519, 1

Steidel, C. C., Bogosavljević, M., Shapley, A. E., et al. 2011, ApJ, 736, 160

Steidel, C. C., Erb, D. K., Shapley, A. E., et al. 2010, ApJ, 717, 289

Susa, H., & Umemura, M. 2004, ApJ, 600, 1

Swinbank, A. M., Bower, R. G., Smith, G. P., et al. 2007, MNRAS, 376, 479

Tanaka, M., Chiba, M., Hayashi, K., et al. 2018, ApJ, 865, 125

Tody, D. 1986, in Proc. SPIE, Vol. 627, Instrumentation in astronomy VI, ed. D. L. Crawford, 733

Tody, D. 1993, in Astronomical Society of the Pacific Conference Series, Vol. 52, Astronomical Data Analysis Software and Systems II, ed. R. J. Hanisch, R. J. V. Brissenden, & J. Barnes, 173

Tollerud, E. J., Bullock, J. S., Strigari, L. E., & Willman, B. 2008, ApJ, 688, 277

Tomczak, A. R., Quadri, R. F., Tran, K.-V. H., et al. 2014, ApJ, 783, 85

Trentham, N., Sampson, L., & Banerji, M. 2005, MNRAS, 357, 783

Tumlinson, J., Peeples, M. S., & Werk, J. K. 2017, ARA&A, 55, 389

Umehata, H., Fumagalli, M., Smail, I., et al. 2019, Science, 366, 97

Vanzella, E., Calura, F., Meneghetti, M., et al. 2017, MNRAS, 467, 4304

Verhamme, A., Dubois, Y., Blaizot, J., et al. 2012, A&A, 546, A111

Wilkinson, D. M., Maraston, C., Goddard, D., Thomas, D., & Parikh, T. 2017, MNRAS, 472, 4297

Willmer, C. N. A. 2018, ApJS, 236, 47

Wisotzki, L., Bacon, R., Blaizot, J., et al. 2016, A&A, 587, A98

Wisotzki, L., Bacon, R., Brinchmann, J., et al. 2018, Nature, 562, 229

Wright, A. H., Robotham, A. S. G., Driver, S. P., et al. 2017, MNRAS, 470, 283

Wu, J., Jiang, L., & Ning, Y. 2020, ApJ, 891, 105

Wyder, T. K., Treyer, M. A., Milliard, B., et al. 2005, ApJ, 619, L15

Wyithe, J. S. B., & Loeb, A. 2013, MNRAS, 428, 2741

Xue, R., Lee, K.-S., Dey, A., et al. 2017, ApJ, 837, 172

Xue, X. X., Rix, H. W., Zhao, G., et al. 2008, ApJ, 684, 1143

Yamanoi, H., Komiyama, Y., Yagi, M., et al. 2012, AJ, 144, 40

Yue, B., Castellano, M., Ferrara, A., et al. 2018, ApJ, 868, 115

Yung, L. Y. A., Somerville, R. S., Finkelstein, S. L., Popping, G., & Davé, R. 2019a, MNRAS, 483, 2983

Yung, L. Y. A., Somerville, R. S., Finkelstein, S. L., et al. 2020, MNRAS, 496, 4574

Yung, L. Y. A., Somerville, R. S., Popping, G., et al. 2019b, MNRAS, 490, 2855

Zhang, H., Ouchi, M., Itoh, R., et al. 2020, ApJ, 891, 177

Zheng, Z., Cen, R., Weinberg, D., Trac, H., & Miralda-Escudé, J. 2011, ApJ, 739, 62